An X-ray and Neutron Scattering Study of Critical and Lattice Dynamics

Thesis submitted by
Mark Hewitt

For the Degree of
Doctor of Philosophy

Department of Physics
University of Edinburgh
March 1992

Declaration

I declare that, unless otherwise stated explicitly, the work presented in this thesis is my own, and that the composition of the thesis has been my own work. Where the collaboration of others has played an important part in the performance of the experimental measurements reported, this has been acknowledged.

Signed

M. Hewitt

Fundamental Constants and Units of Energy

A number of fundamental constants occur repeatedly in this thesis and therefore the symbols used for these constants and their values are listed below.

Symbol	Constant	Value	SI Units
$\hbar$	Planck's constant/2π	$1.054x10^{-34}$	Js
μ_β	Bohr magneton	$9.274x10^{-24}$	J/T
μ_N	Nuclear magneton	$5.051x10^{-27}$	J/T
m_n	Mass of neutron	$1.675x10^{-27}$	Kg
m_e	Mass of electron	$9.11x10^{-31}$	Kg
γ_N	Gyromagnetic ratio of the neutron	-1.914	
k_B	Boltzmann's constant	$1.381x10^{-23}$	J/K
e	electromagnetic charge	$1.602x10^{-19}$	C
c	speed of light in vacuo	$2.998\,x10^{8}$	m/s

The units of energy used depend on the individual chapter and their suitability. The conversion factors between several different units are given below.

$$1\text{meV} = 1.60219x10^{-22}J$$

$$1\text{THz} = 4.13541meV$$

Acknowledgements

I wish to thank Professor R.A. Cowley for suggesting the projects which comprise this thesis and my second supervisor Dr R.J. Nelmes. I would also like to thank Dr A.D. Taylor of the Rutherford Appleton Laboratory for his experimental assistance in collecting the inelastic neutron scattering data presented in chapter 2. I am grateful to have benefitted from Dr T.W. Ryan's introduction to the technique of x-ray scattering.

I should also like to thank Dr P. Mitchell, Dr H. Mook and Dr R. Pynn with whom I collaborated during the studies described in chapter 3 and Dr W.G. Stirling for his invaluable help in running the experiment at the Institute Laue Langevin. Much of the analysis of the experimental data in chapter 3 was performed on the Distributed Array Processor at Edinburgh University, and I am grateful to Dr P. Mitchell for the use of his fitting program, Shamgars Oxgoad. I appreciate the technical support provided by the staff of the Institute Laue Langevin, Rutherford Appleton Laboratory and Edinburgh University physics department.

I acknowledge the award of a D.E.N.I. postgraduate studentship and support from the S.E.R.C. Finally I should like to express my appreciation to Mrs E. McKirdy whose expert typing of manuscripts ,often at short notice, was invaluable.

Abstract

The first project was an attempt to test experimentally the conditions under which the impulse approximation (IA) is valid for the dynamic structure factor of a real crystal, where anharmonic effects are significant, and determine the high energy motions in solids. Neutron scattering measurements for a polycrystalline lithium sample were made for wavevector transfers in the range 14 $\AA^{-1}$ to 49 $\AA^{-1}$ at the Rutherford Appleton Laboratory. The wavevector scaling properties of the position of the maximum and width of the scattered neutron distribution suggest that the IA is a good approximation for $Q>25$ $\AA^{-1}$ at a sample temperature of 100K. However, the width was found to be 14% larger than that calculated using the harmonic model density of phonon states determined by experiment. Numerical calculations for the incoherent dynamic structure factor predicted widths that were in good agreement with those calculated assumming the IA to be valid. It is concluded that either the model density of phonon states is incorrect or a systematic experimental error is present due to the approximation made for the instrumental resolution function.

Several theoretical predictions for the power law divergence of the wavevector, magnetic field and energy dependence of the longitudinal magnetic susceptibility for an isotropic ferromagnet below the Curie temperature remain untested. Inelastic neutron scattering measurements were performed at the Institute Laue Langevin for a single crystal of EuO, which is an almost ideal isotropic Heisenberg ferromagnet, in order to test the theoretical predictions. The wavevector dependence of the longitudinal susceptibility was found to be well described by the mean field result, and the divergent term concluded to be absent or negligibly small. The energy dependence was found to be quasielastic, and was represented empirically by a Lorentzian. The statistical accuracy of the data precluded a detailed test of the longitudinal susceptibility field dependence.

Lead magniobate is a system with competing interactions and may exhibit a spin glass phase in the absence of an applied electric field. The objective of this project was to distinguish between a true spin glass phase, random frozen in electric dipoles, and a

random field like phase that is comprised of many small ferroelectric domains by the technique of x-ray diffraction. Measurements of the x-ray distribution scattered by the crystal into the (001) crystallographic plane showed intense streaks of diffuse scattering that extended from the Bragg reflections along the [110] crystallographic directions to the Brillouin zone centre. The wavevector and intensity dependence of the scattered x-ray distribution at a temperature of 20K is in qualitative agreement with the calculated structure factor for 90° domain walls in a tetragonal perovskite structure. The scattered x-ray distribution was measured in the temperature range 20K to 620K. It was concluded from this that lead magniobate consists of many small ferroelectric domains that persist above the permittivity maximum at room temperature. Streaks of diffuse scattering along the [211] crystallographic direction and weak Bragg reflections at the Brillouin zone centre were measured in the (011) plane. The origin of this scattering is not understood at present.

Contents

Chapter 1

Introduction

1.1 Introductory review

This thesis presents three independent projects each having a particular emphasis on the interpretation of the results from scattering experiments. Each project has been assigned a separate chapter with a specific introduction explaining the particular motivation for the work and a subsequent presentation of the experimental detail and results. To eliminate unnecessary repetition, Sections (1.2) and (1.3) of this chapter serve to review the background common to the work presented in chapters 2, 3 and 4, and to define the notation and terminology used throughout this thesis. The following is a brief outline of the work contained in those chapters.

Many neutron scattering experiments have been performed to determine the condensate fraction of superfluid He^4 following the suggestion that, at sufficiently high wavevectors transfers where the Impulse Approximation (IA) is valid, the atomic momentum distribution maybe determined directly from the scattered neutron distribution. However the failure to isolate the bose condensate as a separate peak in the He^4 momentum distribution has resulted in much discus-

sion in the literature about the validity of the IA for quantum liquids and solids. Many of the pathological features found in the models applicable to these systems are not present in those for solids bound by harmonic forces and it is anticipated that the IA may be valid for experimentally accessible wavevector transfers. In chapter 2 we present neutron scattering measurements for a polycrystalline lithium sample in order to test the validity of the IA at momentum transfers accessible to experiment. With the assistance of Dr A. D. Taylor data were collected using the high resolution spectrometer HET at the ISIS spallation source for wavevector transfers in the range $14\mathring{A}^{-1} < Q < 49\mathring{A}^{-1}$. Numerical calculations for the dynamic structure factor assuming a harmonic model for lithium are compared to the experimental results and the validity of the impulse approximation is discussed.

Various theoretical techniques have been used to calculate the static critical properties of the isotropic Heisenberg ferromagnet. These concur that the longitudinal magnetic susceptibility has a power law divergence as a function of wavevector or applied magnetic field below the critical point. However conflicting results have been obtained for the energy dependence of the dynamic longitudinal susceptibility. Using a crystal of europium oxide ,which is almost an ideal realisation of the isotropic Heisenberg model, we have attempted to observe these divergences, and determine the inelastic form of the dynamic susceptibility below the critical point using the technique of neutron scattering with polarisation analysis. For these purposes the high resolution spectrometer IN12 at the high Flux reactor in Grenoble was ideal. This work is reported in chapter 3 and was performed in collaboration with Dr's P. W. Mitchell, H. Mook, R. Pynn and Professor R. A. Cowley.

The high temperature paraelectric phase of lead magniobate, $Pb_3MgNb_2O_9$, has a cubic perovskite structure , formula ABO_3, with quenched disorder between the Mg and Nb on the crystallographic B site. The different atomic radii of magnesium and niobium ions and the microscopic inhomogeniety of their dis-

tribution gives rise to random electric dipole fields, and regions with competing tendencies to order ferro or antiferroelectrically. Such a system may possess either a ferroelectric or a 'glass' like phase. In the absence of agreed theoretical criteria for the existence of a glass phase and the experimental difficulty in differentiating between the possibilities mentioned, the nature of the low temperature phase is still uncertain. Diffuse and high resolution diffraction x-ray measurements have been made using the triple crystal x-ray spectrometer in Edinburgh to investigate the microstructure of this compound as a function of temperature and electric field. The theory for the scattering of x-rays by static 90^0 domain walls in the tetragonal phase of the perovskite structure has been developed and is compared to the data. The results are incompletely understood at present.

1.2 Critical phenomena

Many excellent monographs and articles are available about the extensive subject of critical phenomena(Stanley (1971), Ma (1976), Pfeuty and Toulouse (1977)). We shall therefore only introduce the necessary terminology to discuss critical phenomena and some of the general ideas and results that are of interest to test experimentally.

A phase undergoes a transition when it becomes unstable under a given set of thermodynamic conditions (Adkins 1975). This leads to the following thermodynamic classification of a transition by Ehrenfest (1933): a transition is said to be of the same order as the derivative of the Gibbs free energy which shows a discontinuous change at the transition. However this classification is unsatisfactory in several respects and Landau (1937) has introduced the concept of an order parameter which is zero in the disordered phase and finite in the ordered phase to distinguish between the two phases. This implicitly recognises two of the most important characteristics of phase transitions; the lowering of the sym-

metry of some property, electron or spin density . . .etc, at the critical point and the subsquent development of long range order. Transitions are classified as first or second order depending on whether the order parameter changes continuously or discontinuously at the transition point. It is usual to choose a macroscopic observable such as the magnetisation density as the order parameter.

In recent years the second order transition has attracted most attention because in the critical region it was found that the behaviour for all second order transitions was qualitatively similar. Subsequently it has been the goal of theorists to develop an understanding of the basic simplicity and apparent close similarity of critical behaviour in widely different contexts, such as that found at ferromagnetic and liquid critical points. The systems considered in this thesis belong to this class of transition, and all further discussion will be restricted to this group.

1.2.1 Landau theory

The simplest view of phenomena near a critical point, attributable in its general form to Landau (1958), is of universal character and attributes certain common characteristics to all phase transitions. Because of the insight gained into critical phenomena and the construction of a Landau theory as a necessary first step in the application of more sophisticated techniques we shall discuss it in some detail.

Landau assumes that the free energy may be expressed as a power series in the order parameter, denoted M, with temperature dependent coefficients a(T),b(T) and c(T). The number of terms in the expansion, equation (1.1), is restricted by stability requirements to:

$$F = \int dr F_o - hM(r) + a(T)M^2(r) + b(T)M^4(r) + c(T)[\nabla M(r).\nabla M(r)] \quad (1.1)$$

where h is the field conjugate to the order parameter and F_0 is a constant. The

$$\chi\Big|_{h=0} = \begin{cases} \Gamma\,(t)^{-\gamma} & \gamma = 1 \\ \Gamma'(-t)^{-\gamma'} & \gamma' = 1 \end{cases} \qquad M = \begin{cases} 0 & T > T_c \\ B(-t)^{\beta} & \beta = \frac{1}{2} \quad T < T_c \end{cases}$$

$$t = \frac{T - T_c}{T_c} \qquad \xi = (T - T_c)^{-\nu} \qquad \nu = \frac{1}{2}$$

Table 1.1 relates the citical exponents to the physical quantities defined in the text The parameters Γ, Γ' and B are amplitude factors, and T_c the critical temperature.

last term represents the energy cost of an order parameter which is spatially dependent. The most probable value of $M(r)$ is given by the Ginzburg-Landau condition :

$$[2a(T) + b(T)M^2(r) - 2c(T)\nabla^2]M(r) = h(r) \qquad (1.2)$$

It is then assumed that a(T)=d(T-T_c), where T_c is the critical temperature and d a co-efficient, and that M(r) may be replaced by an average spatial value. The results for the critical exponents of the order parameter and isothermal susceptibility, χ, are then obtained, and are presented in Table (1.1).

The isothermal susceptibility is defined as the response function conjugate to the field , $\chi = \lim_{h\to 0} \frac{M}{h}$. When considering dynamic phenomena the dynamic susceptibilty is the analogous response to an alternating field with a frequency ω and wavevector q. Other thermodynamic functions which diverge at the critical point include the specific heat which has a critical exponent α.

The concept that exponents and amplitude ratios are identical for all systems with a qualitatively similar free energy expansion is known as universality. In general the free energy expansion of equation(1.1) contains combinations of the order parameter components which are invariant under the point symmetry group of the crystal (Toledano (1988)) and results in a number of universality classes.

The static correlation function . $G(R_i R_j)$. describes the degree of correlation between the order parameter M at site i and j. The function depends only on $R_i - R_j$ because of crystal translational symmetry and is given by:

$$G^{\alpha\beta}(R_i - R_j) = < M_{i\alpha'} M_{j\beta'} > - < M_{i\alpha'} >< M_{j\beta'} > \quad (1.3)$$

$$= \frac{k_B T}{8\pi c} \frac{e^{-\frac{|R_i - R_j|}{\xi}}}{R_i - R_j} \quad (1.4)$$

where $\alpha'\beta'$ are referred to a set of orthogonal axes , c is a constant and the temperature dependence of ξ is given in Table (1.1). The behaviour of ξ indicates that the fluctuations become of a very great spatial extent close to the critical point. The significance of $G(R_i - R_j)$ will become apparent in Section (1.3).

Landau theory predicts the existence of universality classes characterised by macroscopic properties such as symmetry and number of order parameter components (Griffiths (1970)). The divergence of the various thermodynamic response functions as a simple power law is qualitatively in agreement with experiment, but in the limit of arbitrary close approach to the critical point is quantitatively incorrect for systems in three dimensions. This failure may be related to the internal inconsistency in the theory which, derived under the assumption that the fluctuations could be neglected, predicted their divergence at the critical point. Clearly more sophisticated theories should take these into account correctly.

A modified formulation of the Ginzburg[1](1960) criteria for the conditions under which Landau theory is exact was proposed by Als-Nielsen and Birgeneau (1977). They show that the mean field exponents are valid above a critical lattice dimensionality ,d_c, given by $d_c = \frac{(\gamma+2\beta)}{\nu} - m$, where m is the anisotropy of the critical fluctuations. Isotropic systems have $d_c = 4$ and therefore fluctuation effects should dominate the observed critical behaviour in three dimensions. Finally a second critical dimensionality,the so called lower critical dimension, LCD, exists below which fluctuations are of sufficient magnitude to prevent the oc-

[1] The Ginzburg criteria states that below T_c mean field theory is valid provided that the fluctuations in the order parameter, denoted ∂M, satisfy the condition $(\partial M)^2 << M^2$ when averaged over the correlation length of the fluctuations.

curence of long range order. These fluctuations may be induced thermally or by the presence of various types of defects (Halperin and Varma (1977)).

1.2.2 Modern theories of critical phenomena

An alternative microscopic approach is provided by statistical mechanics from which the usual thermodynamic quantities can be calculated from equation (1.5):

$$Z = Tr\left(e^{-\frac{H}{k_B T}}\right) \tag{1.5}$$

and equation (1.6):

$$F = -k_B T ln Z \tag{1.6}$$

where H is the Hamiltonian, Z the partition function and Tr denotes the trace. Unfortunately we can proceed directly to obtain an analytic solution for only a few simple model Hamiltonians (Ising (1925), Onsager (1944), Domb and Green (1974)). Exact solutions exist for the Ising model in 1,2 and 4 dimensions, Heisenberg model in 1 and 2 dimensions, and provide a valuable test for various approximations and numerical techniques. The simplest approximation for decoupling the many-body problem is the mean field approximation (Brout (1965)) where the effect of all neighbours on a particle is replaced by an average molecular field. From the effective single particle Hamiltonian various thermodynamic functions maybe calculated. This approximation gives the same critical exponents as obtained from Landau theory, because it also fails to incorporate the fluctuations properly.

An attempt to find a phenomenological description was made by Widom (1965) and Kadanoff et al (1967) who proposed a scaling theory. The original static scaling hypothesis assumes that the static correlation function, equation (1.4), in the domain of large distances r compared to microscopic lengths, depends only on the ratio $\frac{r}{\xi}$, with different behaviour in the limiting regimes $r \ll \xi$ and

$r \gg \xi$. For a d dimensional system and r < ξ ,G(r) becomes:

$$G(r) = r^{(-d+2)} e^{-\frac{r}{\xi}} \rightarrow r^{(-d+2+\eta)} D'(\frac{r}{\xi}) \qquad r = R_i - R_j \qquad (1.7)$$

where D' is an unknown scaling function and $\eta = 0$ for classical theories. Fourier transforming equation (1.7) and using the relation $\gamma = (2 - \eta)\nu$, the resultfor the susceptibility is obtained:

$$\chi(q) = t^{-\gamma} D' \left(\frac{q^2}{t^{2\nu}} \right) \qquad (1.8)$$

which for $q = 0$ reduces to the uniform susceptibility that diverges at the critical point. On the assumption that the correlation function varies smoothly for all values of q and ξ, except for the singularity at the critical point, the forms valid in each regime must coincide when extrapolated to the line $q\xi = 1$. The great utility of hydrodynamic theory[1] when coupled with scaling theory is the predictions (Enz (1974)) it leads to for the hydrodynamic parameters near the critical point where the theory may not be valid. Although the scaling theory successfully predicts the equalities observed experimentally between critical exponents it is not rigorous, but based on physically plausible arguements. The great value of the scaling hypothesis was the insight it provided for the development of the renormalisation group theory.

The method is mathematically complex and consequently only the results necessary to the work presented in this thesis are presented. A more complete account of the technique can be found in the reviews by Wilson (1974) and Fisher (1974).

A major result of the renormalisation group is the existence of a fixed point under the renormalisation group transformations for static phenomena which provides support for the static scaling hypothesis of Kadanoff et al (1967). The study of various model systems also supports the concept of universality classes which are dependent only on such features as the lattice dimension, number of order parameter components and range of interactions.

Terms in the Hamiltonian, that are originally small, may become important

1 Hydrodynamic theory is based on conservation laws for the physical quantities of interest with empirical co-efficients defined to describe their transport. Within this formalism the dynamic susceptibility is calculated in the limit that q is very much less than the typical fluctuation correlation length, ξ, at that temperature. Clearly, this assumption may not be valid for any q when the temperature is made arbitrarily close to T_c, because the correlation length ξ diverges.

at the fixed point. This may destablise the fixed point and result (Reidel and Wegner (1970 a, b) in a continuous change of the critical exponents between the universality classes. Aharony (1973 a, b) has recently investigated the effect on the critical behaviour of an isotropic short range interaction Hamiltonian due to the addition of dipolar interactions or cubic anisotropy. To first order in $\epsilon = 4 - d$ the critical exponents γ and α are changed to:

$$\frac{1}{\gamma} = 1 - \frac{\epsilon}{4}, \alpha = \frac{-\epsilon^2}{8}$$

$$\frac{1}{\gamma} = 1 - \frac{9\epsilon}{34}, \alpha = \frac{-\epsilon}{34}$$

when dipolar interactions are present. If the dipolar interactions are of sufficient strength they will dominate the critical behaviour at all temperatures.

Experimental measurements have not been sufficiently precise to detect a dipolar contribution to the static critical exponents α and ϵ. Specific heat measurements (Ahlers (1971)) give $\alpha = -0.04 \pm 0.06$ and measurements for ν using neutron scattering (Dietrich et al (1976)) and bulk methods (Hog (1973)) gave $1.29 \pm 0.01$and 1.39 ± 0.5 respectively for the isotropic ferromagnet europium oxide.

The breaking of a continuous symmetry in a system leads to a set of collective excitations that necessarily have zero frequency in the limit $q = 0$ (Goldstone (1961) Bludman and Klein (1963)). The existence of such collective excitations , spin waves, in isotropic Heisenberg systems is the result of breaking the continuous rotational symmetry of the Hamiltonian and is responsible for the divergence in the longitudinal magnetic susceptibility as a function of wavevector and magnetic field. Consequently it is of interest to observe these divergences as a test of the validity of the Heisenberg model for real systems which necessarily possess dipolar interactions and resulting anisotropies.

For dynamic critical phenomenon there is no exactly soluble model which exhibits a phase transition or even a well defined mean field theory that leads

to unambiguous general predictions. Halperin and Hohenberg (1969) have extended the static scaling hypothesis to include a characteristic frequency Γ,

$$\Gamma = \xi^{-z} f(q\xi) \tag{1.9}$$

where the scaling function f and exponent z are universal. This allows predictions similar to the static case to be made about dynamic phenomema. This has received substantial experimental support from investigations on magnetic systems. Unfortunately it does not enable us to predict the analytic form of the dynamic response near the critical region. Another approach is based on the time dependent formulation of the Ginzburg -Landau equations. The critical properties are then investigated by the renormalisation group method, Halperin and Hohenberg(1974), where an equation of motion replaces the Hamiltonian in the static case. It was found that the static universality classes are a subset of the dynamic case, being differentiated by the conservation laws applicable to the equation of motion. The concept of the upper critical dimensionality is still found to apply although this is now defined by the form of the equation of motion and conservation laws as well as by the Hamiltonian, and need not be the same as the upper critical dimensionality in the static case. The upper critical dimensionality for the isotropic Heisenberg model is $d_c = 6$.

Recently the effect of compositional disorder at phase transitions has received much theoretical and experimental attention. Compositional disorder can be divided into two broad categories, annealed disorder where the impurities diffuse freely to reach equilibrium with the system and quenched disorder where the impurities are frozen in fixed positions at the temperature under study. Phase transitions in annealed sytems are quite well understood, and it is the critical behaviour of quenched sytems that is of current interest. Originally it was conjectured that the statistical fluctuations in the spatial distribution of impurities would give rise to a range of local transition temperatures and result in a broadening of the transition. Harris (1974) has shown that provided there is no macroscopic fluctuations in the concentration of impurities the transition occurs

for a unique temperature if the specific heat exponent satisfies the inequality $\alpha < 0$. Lubensky (1975) has obtained the same result using the renormalisation group technique to study a magnetic system with small fluctuations in the exchange interactions.

Edwards and Anderson (1975) have given a mean field treatment of the Heisenberg model with random nearest neighbour exchange interactions. On cooling, the system may exhibit, subject to the form of the interaction probability distribution and next nearest neighbour interaction strength, a transition to a state where the magnetic spins are "frozen" in along random directions. The absence of long range order in the system is a direct consequence of the competing exchange interactions and the inability of any given spin configuration to simultaneously minimise each energy term in the Hamiltonian. Associated with the short range order are numerous ground states that are almost degenerate in energy and which have very long relaxation times.

The random field model proposed by Fishman and Aharony (1979) incorporates competing interactions through the addition of a random field term to the Ising Hamiltonian that couples linearly to the local spin. Within the mean field approximation this model has characteristics similar to the Edwards model, but is simpler in that the low temperature phase consists of small regions within which the order parameter is constant; these are known as domains. Unlike the Edwards model the paramagnetic phase has spin glass like disorder induced by the random fields but it is not the result of a collective transition. Because of the direct physical relevance of the LCD to the applicability of the mean field solutions to the models considered above, most attention and controversy has focussed on this quantity. At present the spin glass and random field models are believed to have LCD of 4 or 3 and 3 or 2 respectively (Binder and Young (1986). It is therefore important to establish experimentally the extent to which the low temperature phases of real systems and these models are similar.

1.3 Scattering theory

The discovery of the diffraction of x-rays by crystals and the relationship between the intensity of the scattered radiation and the atomic structure revolutionised condensed matter physics. Since then the scattering of x-rays, electrons, neutrons and light has become a well established technique (Turchin (1965), Egelstaff (1967), Gurevich and Tasarov (1968), Lovesey (1984), Bacon (1975)) for studying the static and dynamical properties of systems at the atomic level.

The aim of this section is to summarise the formalism within which the results of scattering experiments may be interpreted. We choose to limit the discussion to neutron scattering because it is the technique most widely used in this thesis, specific details of other radiation-matter interactions are left to the relevant chapters. In Section (1.3.1) the partial differential cross section is calculated. The importance of this quantity derives from its direct connection with the correlation function describing the system, and the fact it is the quantity which may be obtained from experiment. The division of this quantity into a coherent and incoherent component is discussed in Section (1.3.2) along with its physical origin. Finally the relationship between the peculiarities of the experimental technique and the properties of the probe used to measure $S(Q,\omega)$ are discussed along with the interrelation of the results obtained.

1.3.1 Partial differential scattering cross section

We consider a scattering process in which a neutron of wavevector k_0 is scattered to a wavevector k_f by a sample that is a single crystal. The change in the neutron wavevector Q is defined by:

$$Q = k_0 - k_f \tag{1.10}$$

and the change in energy $\hbar\omega$ by:

$$\mathcal{E} = \hbar\omega = \frac{\hbar^2}{2m_n}(k_0^2 - k_f^2) \tag{1.11}$$

where m_n is the mass of the neutron. The initial and final spin state of the neutron is denoted by $|\sigma>$ and $|\sigma'>$ respectively. The initial and final states of the target are described by the wavefunctions $|\lambda>$ and $|\lambda'>$ respectively with energy E_λ and $E_{\lambda'}$. The double differential cross section within the first Born approximation is then given by:

$$\frac{d^2\sigma}{d\Omega d\epsilon} = \frac{k_f}{k_0}\left(\frac{m_n}{2\pi\hbar}\right)^2 \sum_{\lambda\sigma} P_\lambda P_\sigma \sum_{\lambda'\sigma'} |<\sigma'\lambda' k_f \mid \hat{V} \mid \sigma\lambda k_0>|^2 \, \delta(\epsilon + E_\lambda - E_{\lambda'}) \tag{1.12}$$

The term $\delta()$ denotes the conservation of energy, and P_λ and P_σ the probability for various sample and neutron states. Physically $\frac{d^2\sigma}{d\Omega d\epsilon}$ is the probability per nucleus that an incident neutron of energy E_0 is scattered by an angle θ into a solid angle element $d\Omega$, and into an energy interval between E_i and $E_i + d\epsilon$. To proceed it is assumed both that the neutron-nuclear interaction is given by (Fermi (1933) $V(r) = \frac{2\pi\hbar}{m_n}\sum_j b_j \delta(r - R_j)$, where R_j is the atomic position, and that the neutron wavefunction may be represented by a plane wave. Using the familar identities (Clarke (1984)) for orthonormal eigenstates and the Hermitian properties of the operator the result for $\frac{d^2\sigma}{d\Omega d\epsilon}$ is obtained:

$$\frac{d^2\sigma}{d\Omega d\epsilon} = \frac{k_f}{2\pi\hbar k_0}\int \sum_{ij} b_i b_j < e^{-iQ\cdot\hat{R}_i(0)} e^{iQ\cdot\hat{R}_j(t)} > e^{i\omega t} dt \tag{1.13}$$

where $<>$ denotes the thermal average, $\sum_\lambda P_\lambda . <\lambda|\hat{A}\hat{B}|\lambda>$, and $\hat{R}$ is the position operator in the Heisenberg representation. The scattering length b_j of an element depend on the isotope and relative neutron nuclear spin orientation. Assuming the isotope, element and spin distributions are random the configurational average (Bacon (1975)) is obtained independently of the average over the initial states of the system by using equation (1.14):

$$b_j = \bar{b} + (b_j - \bar{b}) \tag{1.14}$$

where $\bar{b}$ is the average scattering length. On substituting this into equation (1.13) it is found that the double differential scattering cross section may be written as:

$$\frac{d^2\sigma}{d\Omega d\epsilon} = \frac{k_f}{k_0}\left[b_{coh}^2 S^{coh}(Q,\omega) + b_{inc}^2 S^{inc}(Q,\omega)\right] \tag{1.15}$$

where the coherent dynamic structure factor is defined by:

$$S^{coh}(Q,\omega) = \frac{1}{2\pi\hbar}\int_{-\infty}^{\infty} dt e^{i\omega t}\sum_{ij} < e^{-iQ.\hat{R}_i(0)} e^{iQ.\hat{R}_j(t)} > \qquad (1.16)$$

and the incoherent dynamic structure factor is defined by:

$$S^{inc}(Q,\omega) = \frac{1}{2\pi\hbar}\int_{-\infty}^{\infty} dt e^{i\omega t}\sum_{j} < e^{-iQ.\hat{R}_j(0)} e^{iQ.\hat{R}_j(t)} > \qquad (1.17)$$

Remarkably $\frac{d^2\sigma}{d\Omega d\epsilon}$ can be written as the product of a constant characterising the interaction between the incident probe and the sample, and a function which is dependent purely on the sample. Thus $S(Q,\omega)$ may be determined experimentally by several techniques, light, x-rays and Mossbauer provided the radiation couples to the relevant physical parameter of the system.

1.3.2 Van Hove formalism

The dynamic structure factor can be calculated in the previous formulation if the eigenfunctions of the undisturbed sample are known. However this is possible in only a limited number of cases. As a consequence an alternative representation was presented by Van Hove(1954 a,b,c). The space and time dependent correlation function $G(R,t)$ is introduced in equation (1.18), and is shown to have ,within a classical approximation, a simple interpretation as a probability density distribution which facilitates the interpretation of experimental data and model calculations.

$$S(Q,\omega) = \frac{1}{2\pi}\int_{-\infty}^{\infty} e^{i(Q.R-\omega t)} G(R,t) dR dt \qquad (1.18)$$

Then it follows from equations (1.13),(1.16) and (1.17) that $G(R,t)$ is given by:

$$G(R,t) = \frac{1}{(2\pi)^3 N}\int_{-\infty}^{\infty} e^{iQ.R}\sum_{ij} < e^{-iQ.\hat{R}_i(0)} e^{iQ.\hat{R}_j(t)} > dQ \qquad (1.19)$$

Using the convolution theorem to evaluate equation (1.19) we obtain after some algebra:

$$G(R,t) = \frac{1}{(2\pi)^3 N}\sum_{ij}\int_{-\infty}^{\infty} < \delta[R + R_i(0) - R']\delta[R' - R_j(t)] > dR' \qquad (1.20)$$

The integral in equation (1.20) cannot be evaluated except for $t = 0$ because Heisenberg operators do not commute. If we make the transition to classical mechanics and assume that the operators $\hat{R}_j(t)$ are simply vectors, valid provided $\frac{\hbar^2 Q^2}{2m_n} << \frac{k_B T}{2}$, then :

$$G^{class}(R,t) = \frac{1}{N} \sum_{ij} < \delta(R + R_i(0) - R_j(t)) > \qquad (1.21)$$

where $G^{class}(R,t)$ is the probability of finding any atom at time t in the volume element dR at a point R if a particular atom is at the origin at time $t = 0$. The physical meaning of equations (1.16) and (1.17) is now apparent.

In general $G(R,t)$ is a complex function without classical meaning, the imaginary part of which is discussed by Van Hove (1958). Schofield (1960) has shown that $G^{class}(R,t)$ is real and therefore violates the condition of detailed balance. This may be corrected approximately by substituting the new variable $t + \frac{ih}{2k_B T}$ for t in the correct classical correlation function. A check on the validity of the model $G(R,t)$ is provided by the sum rules (De Gennes and Villain (1960)). The sum rules are exact results for the frequency moments of the dynamic structure factor that are independent of the particular model choosen to evaluate $G(R,t)$.

In addition to the scattering from density fluctuations in the sample due to thermal excitations of phonons it is also clear that static or quasi static deviations from perfect lattice periodicity will give rise to diffuse scattering. Such static density fluctuations may arise from substitutional impurities occupying off lattice sites due to a change in the local force constants or extended defects such as dislocation planes and ferroelectric domain walls separating regions of alternating polarisation orientation. The theory of x-ray scattering by ferroelectric domain walls was developed by Bruce (1981) who finds that the scattering by domain walls takes the form of lines in reciprocal space perpendicular to the wall orientation in real space. It will be shown in chapter 4 that measurements of the wavevector dependence of the intensity distribution of diffuse scattering in reciprocal space can provide detailed information on the atomic displacements

and domain wall structure of the system.

1.3.3 Experimental method and technique.

In Section (1.3.1) and (1.3.2) the underlying unity of various spectroscopies was emphasized. However, the unique properties of the particular radiation used constrain the range of wavevector and energy transfers that may be employed. Consequently stringent tests of model predictions are provided only by comparison of the information obtained from several techniques. Although this thesis is primarily concerned with the interpretation of data obtained from x-ray and neutron scattering experiments a brief review of several other spectrosopies is included.

The different characteristics of the probes used in spectroscopy results in a classification of experimental technique according to the precision and range in which the momentum and frequency response can be measured,Figure (1.1). The great utility of neutron scattering arises from the similarity of the neutron energy and wavelength to those of typical excitations observed in solids, eg phonons and magnons. Hence it is possible to measure $S(Q,\omega)$ over the whole Brillouin zone of the crystal.

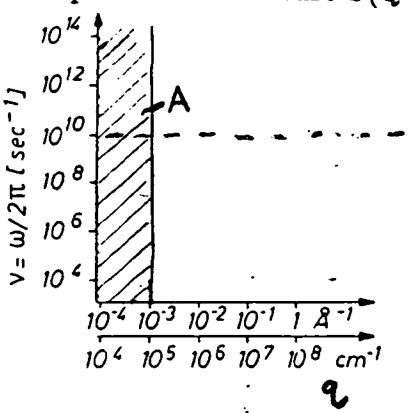

Figure(1.1) shows the q-ω regions accessible to various spectroscopies. Optical spectroscopy is restricted kinematically to region A, $q < 10^{-3}$. Ultrasonic and permittivity measurements apply to a frequency range below $10^{10}s$.
X-rays cover a similar q range to that of neutrons however no energy analysis is possible and we observe an integrated intensity S(Q).

It is clear from equation (1.18) and the general properties of Fourier integrals that the frequency and wavevector of the Fourier components of G(R,t) must be chosen carefully to observe the relevant limiting behaviour in space and time. For example, in chapter 3 it is the spatial and temporal spin correlations over large distances and times that are of interest near the critical point of the ferromagnet. However, in chapter 2 it is the atomic temporal correlations at small times that are of interest. In chapter 4 it is the streaks of x-ray scattering by domain walls that are to be investigated. The streak intensity is relatively weak and the width is approximately only several hundredths of a [1] Angstrom. Therefore an intense source and good wavevector resolution are required. Where both neutron and other techniques are applicable the latter are usually employed because of the expense of using neutrons. These considerations in addition to the strength of the coupling between the radiation and physical parameter of interest determine the choice of radiation for a particular experiment.

Experimentally the determination of the x-ray and neutron wavevector and energy transfer, the radiations used in the experiments which comprise this thesis, may be accomplished by selection of the incident and scattered neutron or x-ray beam by Bragg reflection from a single crystal. Alternatively for neutrons the incident beam wavevector may be determined by a rotating disk (chopper) with a fixed phase relation to a source and the final wavevector inferred by performing a time of flight analysis of the scattered beam over a known path length. The relative merits for either technique depend in general upon the application, but at high incident neutron energies Bragg reflection becomes increasingly inefficient because of the wavevector dependence of the Debye-Waller factor. All instruments situated at spallation sources, which produce neutrons with incident energies in the range 0.1 to 2eV, use the time of flight technique.

The reason for the choice of radiation and technique employed in the projects

1 reciprocal

presented in chapters 2,3 and 4 should now be clear.

Chapter 2

A Study of the Impulse Approximation and Anharmonic effects in Lithium

2.1 Introduction

The determination of atomic momentum distributions in crystals continues to be an area of interest because of the unique information contained about the high energy atomic motions. The momentum distribution is determined by the technique of neutron scattering because the scattered neutron distribution is simply related to the atomic momentum distribution when the impulse approximation (IA) is valid. Within the IA it is assumed that the atom recoils after collision with the incident neutron as if it were a free particle: the effect of the constraining interatomic potential is insignificant.

Nelkin and Parks (1960) have shown that the IA is exact in the limit of high wavevector transfers for the incoherent dynamic structure factor of a crystal with a simple cubic structure that is bound by a harmonic interatomic potential. Gunn et al (1986) have independently obtained this result, and using a Debye model density of states shown that the IA is closely approximated at wavevector transfers less than the maximum accessible with spallation sources, approximately 80 $\AA^{-1}$. However, at the wavevector transfers, and concomitant energy transfers, where the IA may be valid the atom recoils with high energy towards a neighbouring atom and the short range

anharmonic forces may then become important. This may also result in marked deviations from the 'free' particle like behaviour observed when the atom is constrained by a purely harmonic potential well. Consequently, the wavevector transfer required before the IA is valid is uncertain for a real crystal where anharmonic effects are always present. The dynamic structure factor, at high wavevector transfers also contains valuable information about the interatomic anharmonicity, and the high energy atomic motions in solids.

The objective of this study was to ascertain when the IA is valid for a real crystal. The momentum distribution of a crystal bound by harmonic forces is Gaussian with a width determined by the phonon density of states. The region where the IA is valid may be identified by using this result or the scaling property of the scattered neutron distribution proposed by Sears (1984). Sears has suggested that in the IA limit the incoherent dynamic structure factor will not be an independent function of the wavevector and energy transfers but will exhibit a scaling law. The second objective was to observe any deviations in the scattered neutron distribution lineshape from the IA result for a harmonic crystal due to anharmonic effects. Lithium was chosen because it has a simple cubic structure(Montgomery and Covington (1957)), and a model density of phonon states (Smith (1969)) that has been determined by experiment.

This chapter is divided into a number of sections beginning with a discussion of crystal dynamics, Section (2.2), and then the incoherent dynamic structure factor for a harmonic lattice is given in Section (2.2.1). Section (2.3) of this chapter contains a brief description of the time of flight technique, spectrometer and resolution components. The experimental method is discussed in Section(2.4), and neutron inelastic scattering measurements of $S(Q,\omega)$ for polycrystalline lithium, over a range of high energy and wavevector transfers are reported in Section (2.5.1). The results of the numerical calculation for $S^{inc}(Q,\omega)$ within the harmonic approximation at room temperature and 100K are presented in Section (2.5.2) for wavevectors in the range $10\mathring{A}^{-1} < Q < 50\ \mathring{A}^{-1}$. These numerical results are compared to the IA predictions to illustrate the limits of validity for the incoherent approximation. Section(2.5.3) contains a discussion of the results and suggestions for further work are made in Section (2.5.4).

2.2 Crystal dynamics

The theory of lattice dynamics has been extensively reviewed (Lovesey 1984) and several excellent monographs exist. Therefore we shall give only a brief review of one of the phenomenological models - Born Von Karman - (BVK) for a crystal with one atom per unit cell. This model is based on the harmonic approximation viz, the amplitude of the vibration are sufficiently small so that the interatomic forces are linear in the individual atomic displacements. The equation of motion for the l^{th} atom displaced a distance u can be written as :

$$M\frac{d^2u_\alpha(l)}{dt^2} = \sum_\beta \sum_{l'} \Phi_{\alpha\beta}(R_{ll'})(u_\beta(l') - u_\beta(l)) \qquad (2.1)$$

where α and β denote any of the three cartesian coordinates x,y or z , M is the atomic mass and the Φ are called the atomic force constants. Hence for a solution of this equation we write:

$$u_\alpha(l') = B(qj)M^{\frac{-1}{2}}e^{i(q.R_{ll'}-\omega(qj)t)}\xi_\alpha(qj) \qquad (2.2)$$

where B(qj) is the amplitude of the lattice wave and ξ(qj) the polarisation vector. Substituting this solution into equation (2.1) the displacement frequencies are given by:

$$\omega^2(qj)\xi_\alpha(qj) = \sum_\beta D_{\alpha\beta}(q)\xi_\beta(qj) \qquad (2.3)$$

where:

$$D_{\alpha\beta}(q) = \frac{1}{M}\sum_{l'} \Phi_{\alpha\beta}(R_{ll'})e^{iq.R_{ll'}} - 1 \qquad (2.4)$$

is an element of the dynamical matrix that describes the atomic motions.

The condition that solutions exist for the components ξ_x, ξ_y, ξ_z of the polarisation vector ,equation (2.3), is that the determinant of the coefficients vanish. This is an equation of the third degree in ω^2 and yields three solutions for each q: ω(qj), j=1,2,3. The components obey the orthonormality relation

$$\xi_\alpha(qj)\xi_\alpha(q'j') = \delta_{jj'}\delta_{qq'}$$

The BVK formalism has been used extensively for the analysis of the experimentally determined dispersion curves of solids. In practice the force constants are considered as adjustable parameters to be determined by fitting to the experimental data. This procedure gives an adequate description of a large number of metals.

To quantise the vibrations we introduce the Bose operators associated with a given lattice site, namely $\hat{a}(l)$ and $\hat{a}^+(l)$. Then by definition (Lovesey (1984)):

$$\hat{a}^+_\alpha(l) = \frac{1}{\sqrt{N}} \sum_{qj} \xi^*_\alpha(qj) e^{-iq.l} \hat{a}^+(qj)$$

$$\hat{a}_\alpha(l) = \frac{1}{\sqrt{N}} \sum_{qj} \xi_\alpha(qj) e^{iq.l} \hat{a}(qj)$$

where $\hat{a}^+(qj)$ and $\hat{a}(qj)$ obey the anticommutation rule for bose operators :

$$\begin{aligned} [\hat{a}(qj), \hat{a}^+(q'j')] &= \delta_{jj'}\delta_{qq'} \\ < \hat{a}^+(qj)\hat{a}(q'j') > &= \delta_{jj'}\delta_{qq'} n(qj) \end{aligned} \tag{2.5}$$

and $n(qj) = [e^{\frac{\hbar\omega}{k_B T}} - 1]^{-1}$, and $<>$ denotes a thermal average. The total displacement u of atom l is given by :

$$\hat{u}_\alpha(l) = \sum_{qj} \left(\frac{\hbar}{2NM\omega(qj)} \right)^{\frac{1}{2}} \xi_\alpha(qj) e^{iq.l} [\hat{a}(qj) + \hat{a}^+(-qj)] \tag{2.6}$$

The time dependence of the displacement operator is conveniently written in the Heisenberg representation as:

$$\hat{u}(l,t) = \frac{1}{\sqrt{NM}} \sum_{qj} \xi(qj) e^{iq.l} \hat{Q}(qj,t) \tag{2.7}$$

where $\hat{Q}(qj,t)$ is defined as:

$$\hat{Q}(qj,t) = \hat{Q}^+(-qj,t) = \left(\frac{}{2\omega(qj)} \right)^{\frac{1}{2}} [\hat{a}(qj) e^{-i\omega(qj)t} + \hat{a}^+(-qj) e^{i\omega(qj)t}]$$

2.2.1 Scattering Theory

Consider the dynamic structure factor ,equation (1.17), chapter 1 ,

$$S(Q,\omega) = \frac{1}{2\pi\hbar} \int_{-\infty}^{\infty} e^{\ i\omega t} F(Q,t) dt$$

where:

$$F(Q,t) = \frac{1}{N}\sum_{ij} < e^{-iQ.\hat{R}_i(0)} e^{iQ.\hat{R}_j(t)} > \qquad (2.8)$$

and all symbols are defined in Section (1.3). At large Q, F(Q,0) is equal to unity and indicates that only the incoherent terms, i=j are important. In order to increase the clarity of the exposition the atomic position denoted i and j in Section (1.3), will now be included within the parentheses of the position operator $\hat{R}$. Equation (2.8) was evaluated by replacing the operator $\hat{R}(i,t)$ by the relation $i = l + \hat{u}(l,t)$, where $\hat{u}(l,t)$ is the time displacement operator for atom l given by equation (2.1). With the exception of prefactors equation (2.8) is given by:

$$F^{inc}(Q,t) = < e^{-iQ.u_i(l,0)} e^{iQ.u_i(l,t)} >$$

Then assuming $\hat{A} = -iQ.\hat{u}(l,0)$ and $\hat{B} = iQ.\hat{u}(l,t)$ and using the following identities (Lovesey 1984) that are valid if the commutator of $\hat{A}$ and $\hat{B}$ is a c number[1], $< e^{A}e^{B} >= e^{\frac{1}{2}[A,B]} < e^{A+B} >$ and $< e^{A+B} >= e^{<(A+B)^2>}$, it follows that:

$$F^{inc}(Q,t) = e^{\frac{1}{2}<-(Q.\hat{u}(l))^2>} e^{<Q.\hat{u}(l)Q.\hat{u}(l,t)>} \qquad (2.9)$$

From the expansion of $\hat{u}(l)$ in terms of the phonon operators, equation (2.6), $\hat{a}(qj)$ and $\hat{a}^{+}(qj)$ it follows that the first exponent in equation (2.9) becomes:

$$< (Q.u(l))^2 >= \frac{\hbar}{2NM}\sum_{qj} \frac{| Q.\xi(qj) |^2}{\omega(qj)}[2n(qj)+1] \qquad (2.10)$$

To proceed $\sum_{qj}$ was replaced by an integral over the normalised density of phonon states g(ω) defined by:

$$g(\omega) = \frac{1}{3N}\sum_{qj} \delta(\omega - \omega(qj))$$

and then, using the result that the average of $| Q.\xi(qj) |^2$ for a Bravais crystal lattice with cubic symmetry is $\frac{Q^2}{3}$, the relation for W(Q) is obtained:

$$W(Q) = < (Q.u(l))^2 >= \frac{\hbar Q^2}{2M}\int_0^{\infty} d\omega \frac{g(\omega)}{\omega}[2n(\omega)+1] \qquad (2.11)$$

[1] A c number is a complex number.

W(Q) is the well known Debye-Waller factor. To evaluate the second term of equation (2.9) we proceed as before to obtain after some tedious algebra the result:

$$F^{inc}(Q,t) = e^{\frac{\hbar^2 Q^2}{2M}[\gamma(0)-\gamma(t)]} \tag{2.12}$$

where

$$\gamma(t) = \int_{-\infty}^{\infty} d\omega \frac{g(\omega)}{\omega} n(\omega) e^{-i\omega t}$$

We now consider this function in the limit of large Q. To obtain a suitable expansion we rewrite equation (2.12) in powers of t about t=0.

$$F^{inc}(Q,t) = e^{Q^2 \sum_{n=1}^{\infty} \frac{(it)^n}{n!} u_n} \tag{2.13}$$

Essentially it is assumed that at high energy and wavevector transfers the behaviour of $S^{inc}(Q,\omega)$ is determined by the behaviour of the correlation function at t=0. Equating equation(2.12) and (2.13) the result for u_n where n = 1,2 and 3 is obtained:

$$u_1 = \frac{\hbar}{2M}$$

$$u_2 = \frac{\hbar}{2M} \int_0^{\infty} g(\omega)\omega coth(\frac{\hbar\omega}{2k_B T}) d\omega$$

$$u_3 = \frac{\hbar}{2M} \int_0^{\infty} \omega^4 g(\omega) d\omega$$

The exponent in equation (2.12) is expanded to second order and the higher order terms represented by a Taylor expansion; $F^{inc}(Q,t)$ is then given by:

$$F^{inc}(Q,t) = e^{\frac{Q^2}{2M}(i\hbar t - u_2 t^2)}(1 + \sum_{n=3}^{\infty} \frac{u_n}{n!}(it)^n) \tag{2.14}$$

Then using the identity:

$$\int_{-\infty}^{\infty} e^{-z^2}(iz)^n e^{-izx} dz = \sqrt{(2\pi)} H_n(x) e^{-x^2}$$

where $H_n(x)$ are the Hermite polynomials defined by (Fischbeck and Fischbeck(1982)), it can be shown that $S^{inc}(Q,\omega)$ is given by:

$$S^{inc}(Q,\omega) = S^{IA}(Q,\omega)(1 + h(Q,\omega)) \tag{2.15}$$

where:

$$S^{IA}(Q,\omega) = \left(\frac{1}{2\pi\Delta^2}\right)^{-\frac{1}{2}} e^{-\frac{(\omega-\omega_r)^2}{2\Delta^2}} \tag{2.16}$$

and:

$$\Delta^2 = 2\frac{\hbar^2 Q^2}{2M} k_B T_{eff} \tag{2.17}$$

h(Q,ω) represent the final state interactions which can be shown to be a series expansion in powers of p=$\left(\frac{k_B T_{eff}}{\omega_r}\right)^{\frac{1}{2}}$. The coefficients of p are combinations of Hermite polynomials, which are of even or odd symmetry depending on the power of n multiplied by a thermally weighted energy moment of the phonon density of states. The final state effects are alternatively of odd or even symmetry and in the limit of high Q vanish like $\frac{1}{Q^n}$ so that $S^{inc}(Q,\omega)$ asymptotically approaches $S^{IA}(Q,\omega)$. Experimentally the presence of final state interactions can then be observed as an asymmetry in the measured S(Q,ω) with a shift in the peak position from the recoil position, ω_r. The peak in $S^{IA}(Q,\omega)$ is characterised by equation (2.16) and the effective temperature, a measure of the mean kinetic energy of the atom, given by:

$$T_{eff} = \frac{1}{2k_B}\int_0^\infty g(\omega)\omega coth(\frac{\hbar\omega}{2k_B T})d\omega \tag{2.18}$$

$g(\omega)$ is the effective phonon frequency distribution for vibrations with displacements parallel to the momentum transfer. For a polycrystalline solid, where we have a spherical average over the crystal, $g(\omega)$ is replaced by the total density of states.

2.3 Experimental technique

S(Q,ω) was determined by time of flight neutron spectroscopy. This technique is the most favourable for use with the high energy incident neutrons that are produced at a spallation source because selection of a particular energy by Bragg reflection becomes very inefficient for neutrons with incident energies > 200 meV. A schematic diagram of a direct geometry time of flight spectrometer

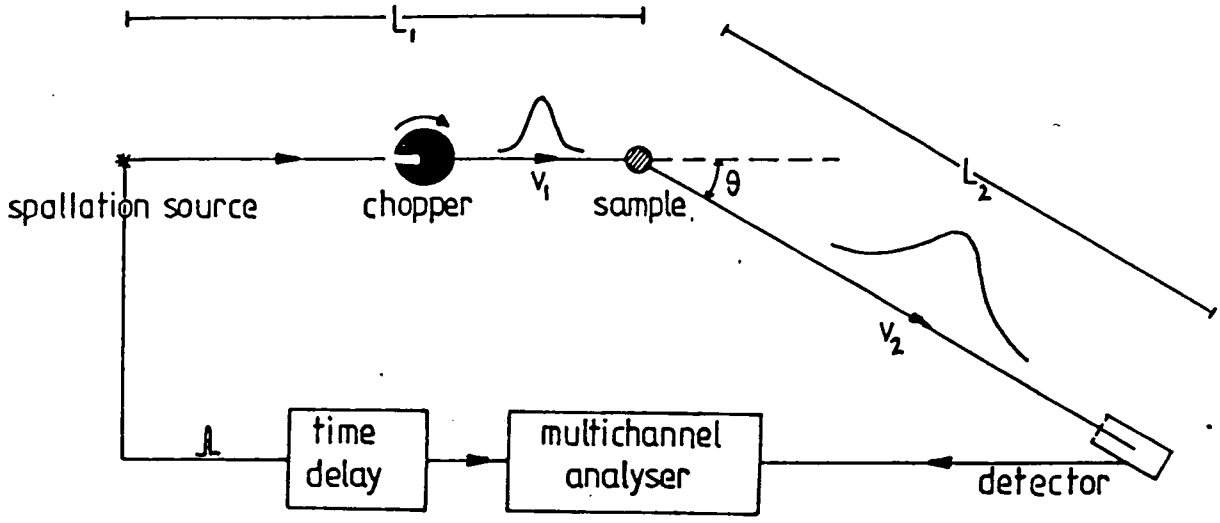

Figure 2.1: Schematic outline of a direct geometry time of flight spectrometer

at a spallation source is shown in Figure (2.1). A spallation source produces a very short polychromatic pulse of neutrons which spreads afterwards due to their different velocities. By maintaining the chopper, which rotates at a fixed frequency, in a definite phase relation to the incident pulse only neutrons with a predetermined velocity , v_1,are allowed to travel to a fixed angle, θ, detector over a measured path length $L_1 + L_2$. The arrival time of the neutron is related to its final velocity, v_2, after the scattering event. An auxillary device, usually electronic circuits, measures the time interval, t, between the firing of the pulse and the response of the detector. A multichannel time analyser records the pulses from the detector in a discrete time interval and stores them as a time spectrum, the range of the time spectrum being proportional to the pulse repetition frequency. Consequently the pulse repetition frequency is a compromise between intensity and the time required to complete the scan before the arrival of the next pulse. The time of flight of the scattered neutrons determines their energy, while the momentum transfer is specified by the detector's angular position. In practice however due to the uncertainities in measured flight paths, angles, finite beam area, detector solid angle and width of time channels the spectrometer does not only record the nominal wavevector Q_0 and energy transfer $\hbar\omega_0$ selected but integrates over a small range of these values. A full deconvolution of the resolution function for a time of flight of spectrometer has

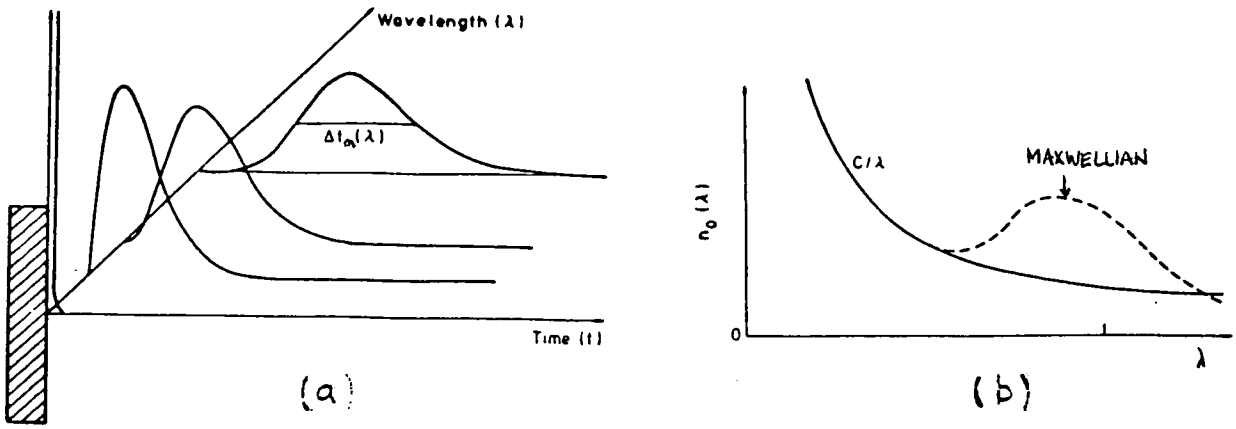

Figure 2.2: (a) Time spread of the pulse as a function of λ after moderation, Δt_m. (b) Flux $n_0(\lambda)$ at the moderator surface of a pulsed source as a function of λ. (Windsor (1981))

not been undertaken in the present work. Therefore only a brief qualitative description of the main resolution degrading components will be given.

2.3.1 Resolution components

The resolution of the spectrometer is given by $\frac{\Delta t}{T}$ where Δt and T are the uncertainty in the time of flight and the total time of flight respectively. The uncertainity in the time of flight is determined by the following components.

Moderator and incident spectrum

The sharp burst of very high energy neutrons from the target station are slowed down by repeated inelastic collisions in the moderator with an associated time scale. Neutrons emitted from the moderator with a longer wavelength require more collisions and subsequently have a significantly larger time spread than the initial pulse, see Figure(2.2 a). It is this time spread that determines the fundamental limit in the resolution and the uncertainty to which the other resolution components are matched. Figure (2.2 b) shows the output from the moderator as a function of wavelength. The undermoderated component of the incident

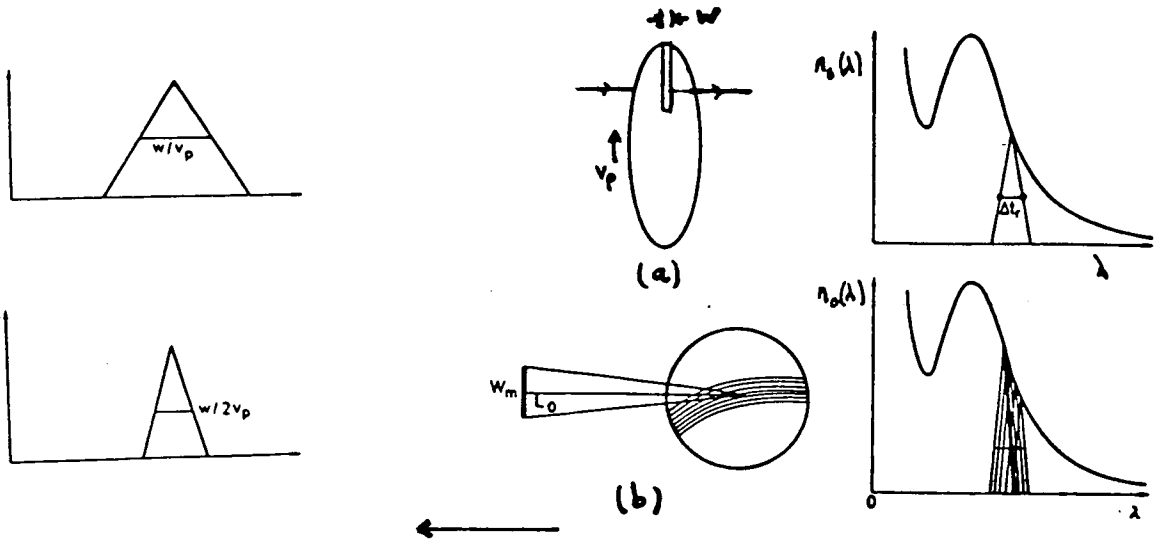

Figure 2.3: Schematic diagram of the disk(a) and Fermi chopper(b) and the flux transmitted as a function of time.(Windsor (1981))

spectrum shown in Figure (2.2 b) is called the epithermal region. In this range the resolution of the spectrometer is independent of the incident wavelength because the pulse width is proportional to the neutron wavelength and the total time of flight inversely proportional to it. The long wavelength component has an approximately Maxwellian distribution in equilibrium at a temperature about 25-30% higher than the physical temperature of the moderator. However in this section we shall not be further concerned with this component.

Neutron chopper

The pulse width and total intensity are dependent on chopper performance. An ideal chopper should be opaque to all neutrons when closed, open quickly and let in a wide solid angle of neutrons for a specified time interval Δt. The simplest mechanical construction is a disk with a slit of width w shown in Figure (2.3 a). For neutrons with infinite speed the transmitted pulse is triangular with a full width half maxima $\Delta t = \frac{w}{v_p}$ where v_p is the peripheral speed. With the practical limitations on v_p ,w must be small to obtain suitable pulse widths. Unfortunately this often gives an unacceptable decrease in the transmitted intensity. However,

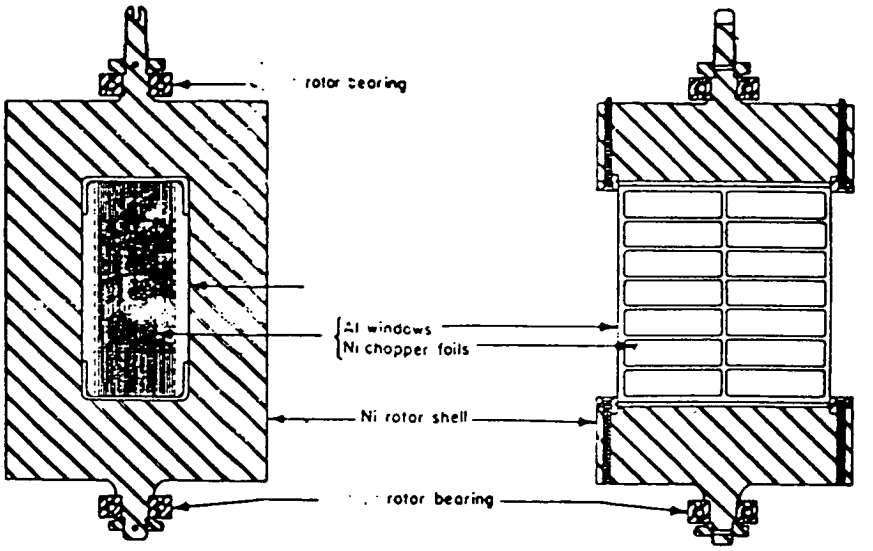

Figure 2.4: Fermi chopper consists of alternating sheets of a neutron transmitting and absorbing material respectively.(Egelstaff (1967)).

in the case where the constraints on the pulse width are less severe the disk chopper, see Figure (2.3 a), gives large transmitted beam areas and because of the large mass inserted into the beam at the chopping point a low background. This is important for fast neutrons because the cross section of all materials is very low at these energies. It is possible to appreciably improve the transmission of the disk chopper without degrading the pulse width by stacking many such slits together of width w separated by absorbing slots of thickness t as shown in Figure(2.4). This is known as a Fermi chopper, and has an overall maximum transmission of $\frac{w}{t+w}$. The chopper is rotated about an axis parallel to the plane of the windows while the neutron beam strikes the chopper perpendicular to the axis. For finite neutron velocities the slot will turn appreciably during the passage of the neutron through it. Consequently the slot is curved so that a neutron of selected velocity v which enters the slot centrally, travels down the curved slot of radius R given by, $R = \frac{v_p}{4\pi f}$. Clearly the chopper is also optimised for incident energies that are a submultiple of the chopper frequency, f. Because the moderator pulse width increases with wavelength it is prudent to run the chopper at submultiples of the fundamental frequency to select neutrons with incident energies that are close to submultiples of the optimal energy. This enhances the flux for a fixed resolution, and is clearly preferable to running the chopper at a fixed frequency and selecting the incident neutron energy solely

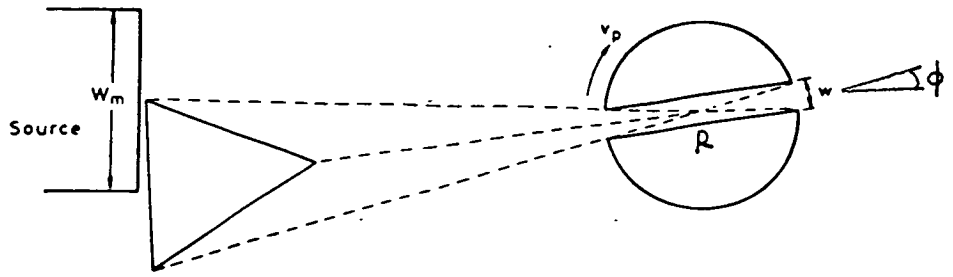

Figure 2.5: The effects in the time pulse as the triangular transmission function sweeps across the uniform brightness of the moderator (Windsor (1981))

through the chopper-source phasing.

Lighthouse effect

When the triangular transmission function of the chopper, Figure(2.5) sweeps across the moderator of finite size, w_m, there will be an increase in the neutron pulse width. The total time uncertainity of the transmitted beam is given by the chopper transmission function convoluted with the moderator neutron intensity time distribution. An ideal pulsed source gives a unique correspondence between the angle of chopper slit rotation and the wavelength of the neutrons incident at the chopper. However the time spread of a real source pulse results in a velocity distribution for the incident neutrons at each angle of chopper rotation, ϕ. This is one of the major difficulties in developing an analytical expression for the spectrometer resolution function.

Multichannel analyser

Electrical pulses from the detectors are summed in discrete time channels to create a time of flight spectrum. Each channel has a width corresponding to a range of neutron flight times. Ideally the time channel width should be small compared to the resolution width of the narrowest structure in the spectra. The choice of channel width is a compromise between resolution and statistical

precision.

2.3.2 Kinematics

The energy and momentum conservation laws apply stringent limitations to the values of Q and ϵ we may observe in an experiment. From equations (1.10) and (1.11) the relation for $\hbar Q$ is obtained:

$$\hbar Q = 2E_0 - \epsilon - 2cos\theta[E_0(E_0 - \epsilon)]^{\frac{1}{2}} \tag{2.19}$$

where E_0 is the incident energy of the neutron and θ the angle through which the neutron is scattered. For each detector in a time of flight experiment the Q and ϵ are coupled together so that a detector at a particular angle scans a parabolic locus in Q,ϵ space, see Figure (2.6). From equation (2.19) it is clear that high incident energies and scattering angles are required to reach large Q and ϵ transfers.

If the IA is valid and the lineshape at constant Q is Gaussian with a FWHM $\Delta\epsilon_Q$, then to a first approximation, the lineshape at constant angle will (Jackson (1974)) also have a Gaussian form, but with the FWHM $\Delta\epsilon_\phi$ given by:

$$\frac{\Delta\epsilon_\phi}{\Delta\epsilon_Q} = [1 - \frac{m_n}{M}\left(\frac{E_0}{E_f}\right)^{\frac{1}{2}} cos\theta - 1]^{-1} \tag{2.20}$$

where m_n and M are the masses of the neutron and atom, E_0 and E_f are the neutron's initial and final energies. The error in this approximation has been assessed numerically and the transformation found to be accurate to $\pm.1\%$ and the displacement of the peak position to be less than $\pm.2\%$ for the incident energies used.

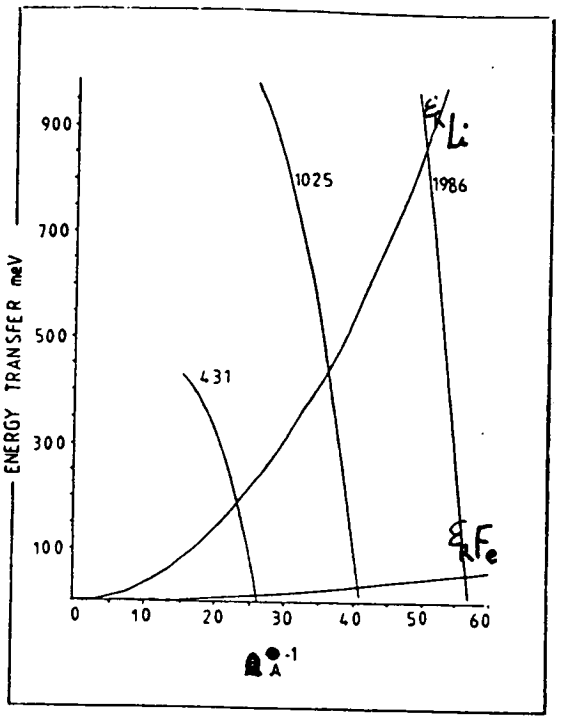

Figure 2.6: Loci of Q and ϵ transfers for three of the incident energies used in the experiment for a detector at an angle of $\theta = 135^0$. Superimposed on this figure are the recoil energies ϵ_r for lithium and iron.

2.4 Experimental method

Details of the direct geometry spectrometer at ISIS have been given elsewhere and its operation will be described only briefly along with the experimental procedure. Pulses of high energy protons were incident on a uranium target with a repitition rate of 50 Hz. The emitted high energy neutrons were moderated by water at room temperature. A Fermi chopper 10m downstream of the moderator rotated at an integral multiple of 50 Hz. The chopper to source phasing and rotation frequency were chosen to select neutrons with an incident energy in the range 227 to 1986 meV. A disk chopper located 2 m upstream from the Fermi chopper decreased the fast neutron background at short times after the pulse of protons strike the target.

The intensity of neutrons scattered by the sample, located 1.8 m from the chopper, were recorded as a function of their time of flight by He^4 proportional counters. The counters were configured into two parallel arrays, with respect to the scattering plane and incident neutron direction, and were nominally at an angle of 124° or 135°. Because the detector efficiency is proportional to $1/k_0$ the second bank allowed a significant increase in the data accumulation rate when higher incident neutron energies were used. A multichannel analyser with bin widths varying from 1 μs to 10 μs recorded the number of neutrons in each time channel. Two low efficiency detectors placed in the direct beam monitored the incident neutron flux intensity and mean energy. The entire spectrometer was kept under vacuum to decrease the contamination of the recorded signal by neutrons scattered by gas. The time averaged flux on the sample was 10^4 neutrons/cm-s.

A stainless steel sample cell, 7 cm diameter, with a 0.05 mm thick window, contained the natural lithium which was 99.999% chemically pure. Natural lithium contains isotopes of Li^7 and Li^6 in the ratio 92% and 8% respectively. The cell was attached to the cold stage of a closed cycle refrigerator, where the temperature stability of the sample was ±1K. Lithium undergoes a Martensitic phase transition at 77K (Martin (1959)). The lowest temperature measurements were made at 100K. Spectra were also collected at room temperature for the empty cell using incident neutron energies of 828 and 1017 meV.

The intialisation, collection and storage of spectrometer data was automated using a VAX11/730. After recording the spectra the data, which consisted of the number of neutrons detected in each time channel of a particular detector, were stored on the magnetic disk of a mainframe computer. A program called GENIE containing the spectrometer configuration characteristics allowed the various data reduction procedures and manipulations that are necessary and computationally intensive to be performed interactively and displayed graphically. In addition

to the catalogue maintained of each data manipulation GENIE also enables individual spectra , or an arbitrary grouping, to be fitted to a model for S(Q,ω) by invoking a user written program. All subsequent analysis of the data were performed using this system.

2.5 Analysis

Data were collected as a function of time of flight so that the intensity, I(t) measured for a time of flight channel t, by a detector at a scattering angle θ, is given by :

$$I(t) = \int_{-\infty}^{\infty} \frac{d^2\sigma}{d\Omega dt} R(Q - Q', t - t')dQ'dt'$$

To obtain $\frac{d^2\sigma}{d\Omega dt}$ from the observed lineshape, I(t), it is necessary to deconvolute the instrument resolution function R(Q, t). The deconvolution procedure is tractable only if the transmission probabilities for the various spectrometer components are assumed to have a simple analytical form, usually Gaussian. This assumption is not generally correct, Section (2.3.1), however under the experimental conditions employed R(Q,t) may be considered initially as a delta function. In addition to the neutrons scattered by the sample cell, the measured spectra also include a background signal due to fast neutrons and electronic noise. The latter contributions were removed by subtracting the measured neutron count in the time of flight channels at very long times. The measured neutron distribution is then proportional to the product of the double differential cross section and the detector efficiency. The incident neutron energy in each case was determined from the monitor peak positions and their known path seperation. The spectrum was then converted to a function of energy transfer using the relation $\frac{d^2\sigma}{d\Omega d\epsilon} = \frac{d^2\sigma}{d\Omega dt} t^4$. The relationship between the double differential cross section and the dynamic structure factor is given in Section (1.3).

Corrections for the kinematical factor $\frac{k_0}{k_f}$ and detector efficiency were applied and

the data summed over the front and back detector arrays. The high absorption cross section, ρ, for lithium negated the correction for multiple scattering, and the effect on the lineshape was computed ,Sears (1975), for a flat plate sample in backscattering geometry, and found to be negligible.

All spectra then are presented as energy distributions, I(ϵ), proportional to S(Q,ϵ). The energy dependence of I(ϵ) was fitted to equation (2.21) over the energy range of interest:

$$I(\epsilon) = A_1 + A_2\epsilon + A_3 e^{\frac{-(\epsilon - A_4)^2}{A_5}} + A_6 e^{\frac{-(\epsilon - A_7)^2}{A_8}} \qquad (2.21)$$

and $A_1 A_2 \ldots . A_3$ were parameters found by the least squares method using a program written by the author, Hewitt2. The fourth term in equation (2.21) describes the recoil scattering from lithium and is only the leading term of the result for $S(Q,\epsilon)$, equation(2.15). Terms one and two of equation (2.21) were identified with the fast neutron background and term three with the background scattering by the steel sample holder. The program Hewitt2 was written in Fortran 77 and ran on the Rutherford Vax computer.

A measure of the quality of the fits was obtained by calculating χ^2 (Bevington 1969)), defined as $\chi^2 = \sum_i w_i \frac{(I_i(meas) - I_i(calc))^2}{N-n}$, which for a satisfactory fit should have a value close to 1.0. The weight factor w_i in the expression was given by the inverse of the square of of the standard deviation of the measured counts, N and n ,represent, respectively the number of experimental points and the number of fitting parameters. The instrumental resolution contribution to the value obtained for A_8 by the fitting procedure was then deconvoluted by assuming that the observed neutron distribution was the convolution of S(Q,ϵ) with a Gaussian resolution function. Variation of the full width half maxima of R(Q t) across the spectra is neglected, and the value chosen for the FWHM was that at the recoil position. Although neither function is strictly a Gaussian we believe this procedure gives widths and positions which are accurate to within the estimated errors. Spectra from individual detectors in the array were analysed

ϵ_0	ϵ_r	A_7	$\Delta\epsilon_Q$	$\Delta\epsilon_{BVK}$	$\frac{\chi^2}{N}$
431[3]	167.7	151 ± 2.9	177 ± 4.3	164	1.26
514	200.0	180 ± 3.0	207 ± 11.8	178	1.15
618	240.1	217 ± 2.5	229 ± 4.8	199	0.83
828[+]	297.3	296 ± 9.0	242 ± 7.0	217	0.63
833	323.7	311 ± 3.0	259 ± 2.2	225	0.89
1026	399.0	392 ± 4.0	286 ± 1.8	253	0.89
1646	639.7	634 ± 8.7	369 ± 12.0	309	0.67
1985[+]	712.7	712 ± 12.0	389 ± 11.0	335	0.66

Table (2.1) shows the values of the fitted parameters defined by equation(2.21) .

[3] not within the single particle regime

[+] data taken at a scattering angle of 123^0

$\Delta\epsilon_Q = A_8\sqrt{8ln2}$ corrected from constant angle to constant Q by equation(2.20) .

$\Delta\epsilon_{BVK}$ FWHM calculated using the $g(\epsilon)$ calculated from Smiths BVK model.

ϵ_0	Temp	A_7	$\Delta\epsilon_Q$	$\Delta\epsilon_{BVK}$	$\frac{\chi^2}{N}$
1985[+]	RT	712 ± 14	480 ± 20.3	448	0.56
1985[+]	100	712 ± 12	389 ± 11	335	0.68
828[+]	RT	291 ± 6	301 ± 10	289	0.55
828[+]	100	296 ± 9	242 ± 7	217	0.63

Table (2.2) shows the values for the fitted parameters defined by equation(2.21) .

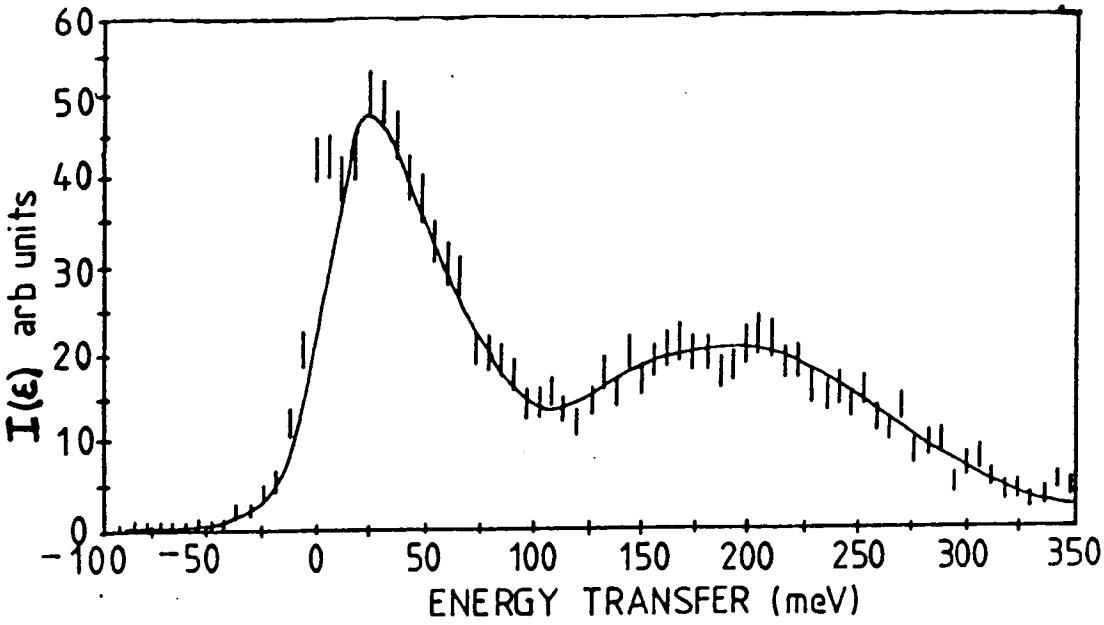

Figure(2.7) shows the measured spectra for an incident energy of 514 meV with the scattering angle at 135^0. The statistical errors are shown, together with a least squares fit to equation(2.21) . The resolution width at the recoil position is 8meV and the data collection time was 0.46 mA hr (neutron beam current x time).

independently and in various combinations and gave fitted parameters to within the estimated errors of the values given in Table (2.1).

2.5.1 Results

Figure (2.7) shows the observed spectra consists of two well separated peaks for an incident energy of 514 meV at a temperature of 100K. Spectra for the empty sample cell showed the peak at lower energies was scattering from the sample cell and occurred approximately at the position expected for recoil scattering from iron. A typical fit to the data (solid line), Figure (2.7), shows equation(2.21) to be a good representation of the data. The best values of the fitted parameters are listed in Table (2.1) and the errors shown reflect the statistical analysis only, and assume there are no systematic errors.

In Figure (2.8) the values for A_7 determined by the fitting procedure discussed in Section (2.5) are plotted as a function of Q^2. The solid line is a plot of the

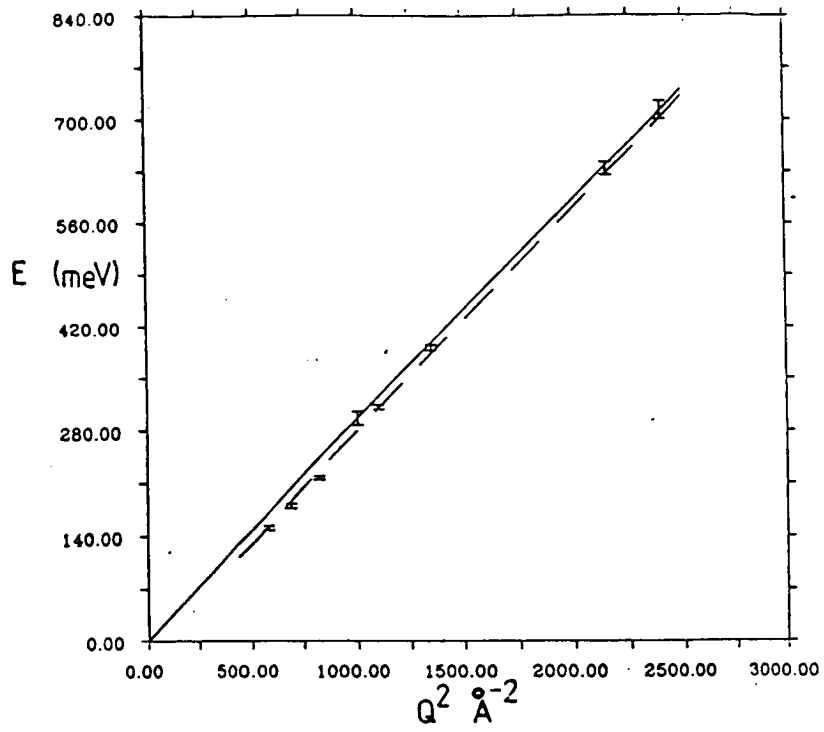

Figure(2.8) shows the recoil position for lithium, solid line, plotted as a function of Q. The peak positions determined from the fitting procedure are shown as points with errorbars along with the peak maxima determined from the full calculation for $S^{inc}(Q,\epsilon)$ at equivalent Q, dashed line .

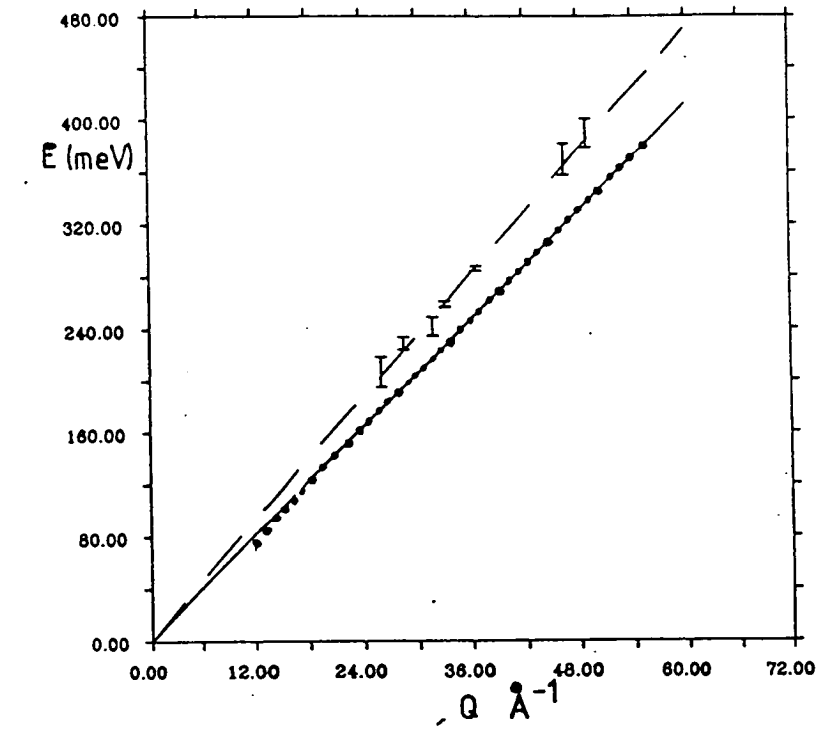

Figure(2.9). The points with error bars are the FWHM determined by the fitting procedure to the data. The FWHM determined from the full calculation for $S^{inc}(Q,\epsilon)$, dotted line, and using the IA result, solid line , are also shown.

lithium recoil energy $\frac{\hbar^2 Q^2}{2M}$, where M is the isotopically weighted average of the Li^7 and Li^6 atomic masses. The measurements suggest the IA regime is approached for Q transfers $>2.5\AA^{-1}$ and a recoil energy of 640 meV. This is much larger than the maximum phonon energy of ≈38 meV but significantly less than the atomic binding energy of lithium which is ≈ 1.6 eV. Gunn et al (1986) have shown for a single Einstein oscillator that although the IA considers the final state of the scattered particle to be a plane wave this need not be a free state. It is sufficient for the final state to be a good approximation to a plane wave over the spatial extent of the initial state. Consequently the observed approach to the regime where the IA is valid for recoil energies of 640meV is not counter intuitive. Plotted in Figure (2.9) are the widths $\Delta\epsilon_Q$ obtained from the values of A_8 obtained by the fitting procedure discussed in Section (2.5) and corrected using equation (2.20) together with a linear fit (dashed line) constrained to pass through the origin. This fit gave an effective sample temperature of 216±1.7K compared to the value of 166K which was obtained by evaluating equation (2.18) numerically with the g(ϵ) ,determined from the neutron scattering data , published by Smith (1968). The IA result is shown as a solid line in the figure. Within the harmonic approximation the FWHM of $S^{IA}(Q,\epsilon)$ is proportional to $\sqrt{T_{eff}}$, equation (2.17). The time of flight spectra were measured for lithium at room temperature and 100K using incident neutron energies of .828 and 2 eV. T_{eff} was calculated using the g(ϵ) determined by neutron scattering at 293K (Beg and Nielsen (1976)) and 100K (Smith (1968)). For each incident energy the ratio of the measured FWHM at 100K and 293 K is systematically lower than the square root of the ratio of their effective temperature at each physical temperature, Table (2.2).

The results show, Table (2.1), that the lineshape is adequately represented by a Gaussian for Q>20 $\AA^{-1}$ as judged by the values for χ^2. This is probably due to the statistical precision of the data as there is some evidence, particularily around the peak position, for structure in the profile of I(ϵ). The systematic increase of χ^2 with decreasing incident neutron energy, apart from the spectra collected

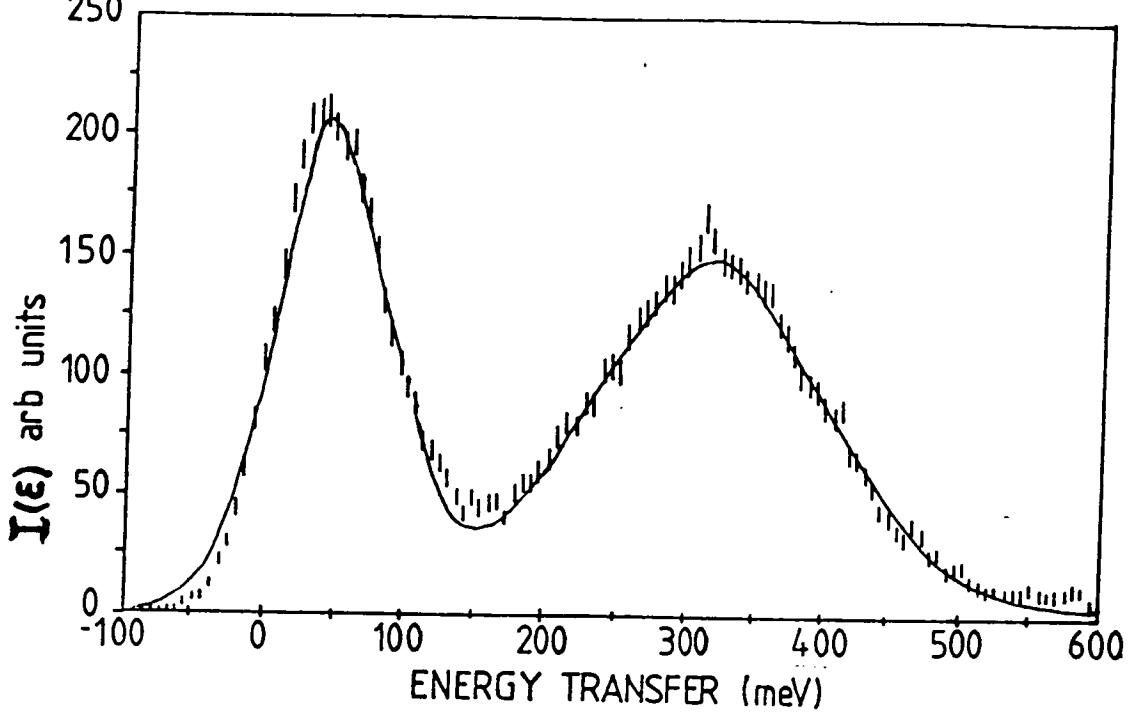

Figure (2.10) shows the measured spectra for an incident energy of 833 meV with the scattering angle at135°. The statistical errors are shown , together with a least squares fit to equation(2.21). The resolution width at the recoil position is 10 meV and the data collection period was 2.2 mA hr (beam current x time).

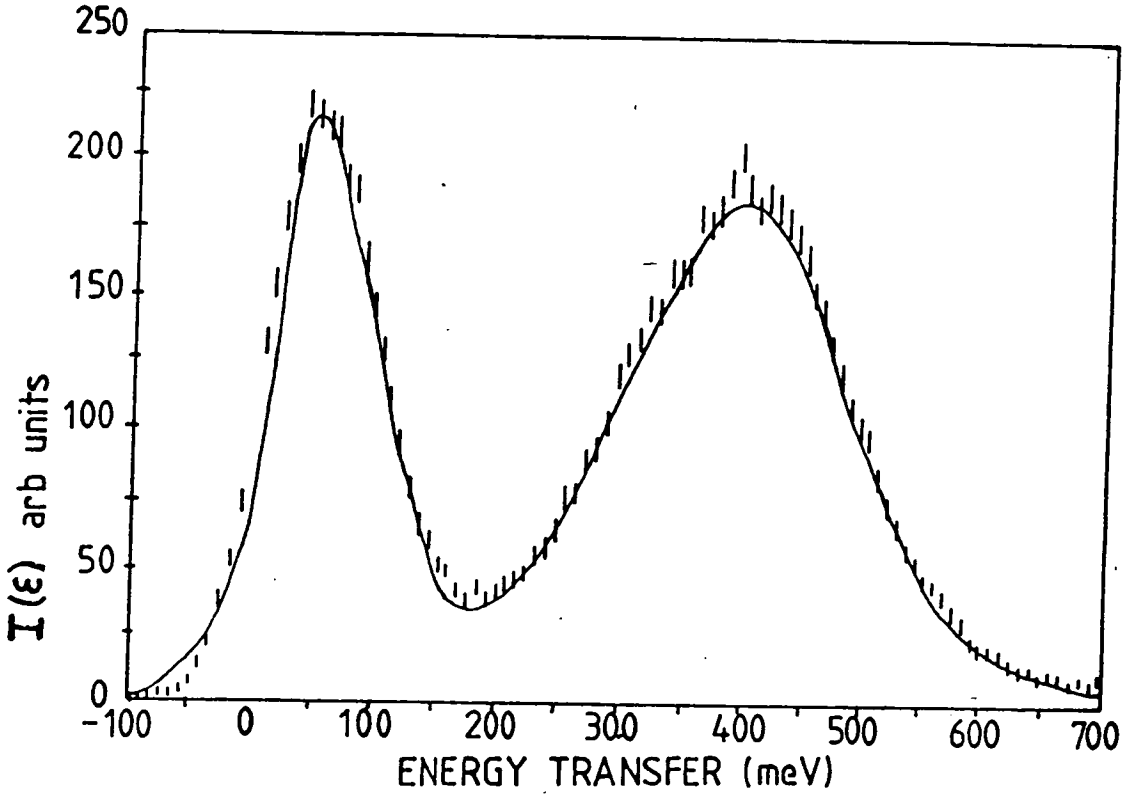

Figure (2.11) shows the measured spectra for an incident energy of 1026 meV with the scattering angle at 135°. The statistical errors are shown, together with a least squares fit to equation (2.21). The resolution width at the recoil position is 12meV and the running time 2.6 mA hr (neutron beam current x time).

with higher statistical accuracy, is due to the increased structure present in the profile of the scattering by the sample cell. The data for an incident neutron energy of 227 meV show several peaks in the lineshape that were attributed to the peak in $g(\omega)$ at 40 meV. At energy transfers comparable to phonon energies $S^{inc}(Q,\omega)$ is proportional to $g(\omega)$ (Egelstaff (1967)) for a polycrystalline solid. Further measurements were made to investigate the lineshape of the scattered neutron distribution in more detail.

Figures (2.10) and (2.11) show lineshape measurements with much higher statistical precision for incident energies of 833 meV and 1026 meV. There is evidence for a feature in the lineshape near the recoil position in each figure with evidence of further structure for energy transfers at approximately 100 and 150 meV above the recoil position. If this structure arises from the phonon density of states, as might be expected if there were a singularity present, then the features produced in $S(Q,\epsilon)$ occur at regular energy intervals and should be more pronounced on the low energy side of the recoil position. Although this appears to be in disagreement with the data presented, the absence of features on the low energy side of the recoil position may be due to scattering from the iron sample cell and poorer experimental resolution.

Sears(1984) has suggested that at large Q, $QS(Q,\epsilon)$ will not be an independent function of Q and ϵ but will exhibit a scaling law. Consequently any features that are a property of the momentum distribution should also scale as $y=\frac{M}{\hbar Q}(\epsilon-\frac{\hbar^2Q^2}{2M})$. Figure (2.12) shows the data in Figures (2.10) and (2.11) plotted as a function of the variable y and normalised against the height of the peak fitted to the lineshape by the least squares procedure described earlier. The scattering from the sample cell has been subtracted on the assumption that it may be represented by a Gaussian form, the parameters of which were also determined earlier. The lineshape is within the approximation made and counting statistics a universal

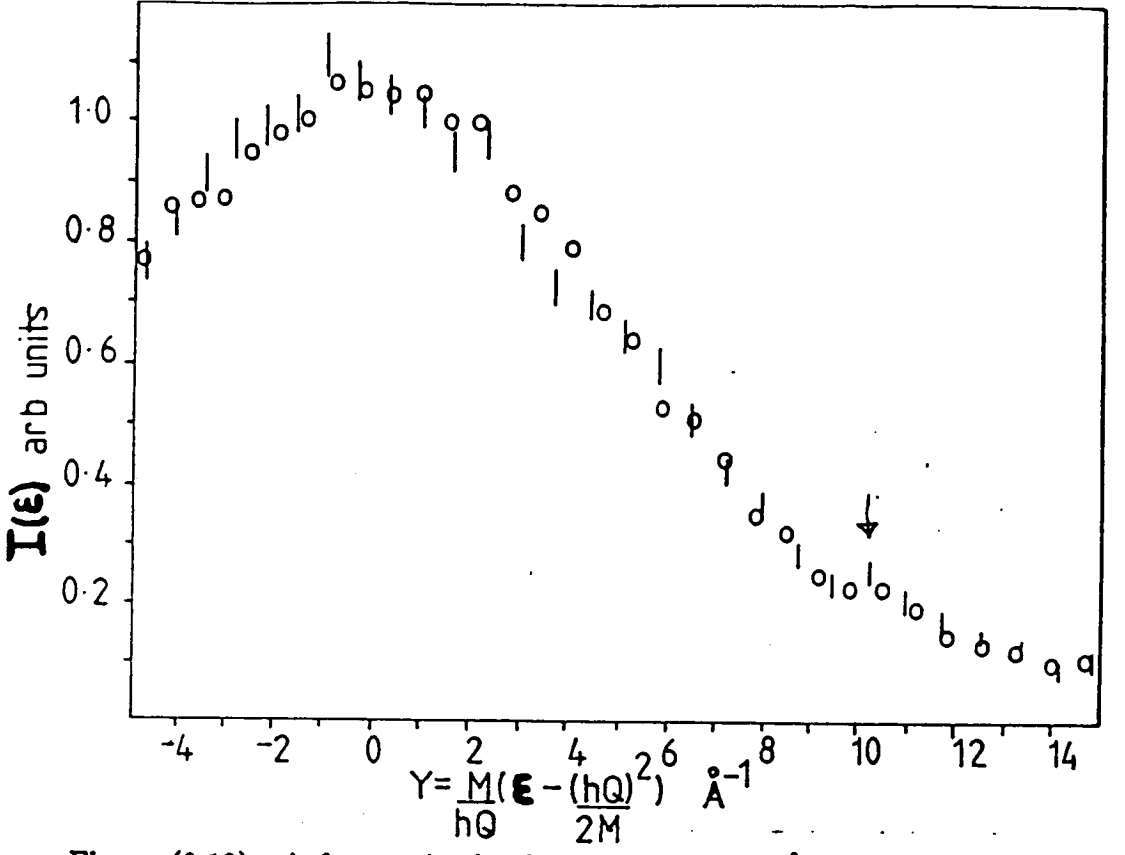

Figure (2.12). A feature is clearly seen at Y = 10Å^{-1} in both spectra. It is unlikely to be due to recoil scattering from an impurity atom because only H and He have smaller masses than Li^7 and the former cannot scatter for angles greater the 90^0. Li^6 would produce features at 399 meV and 323 meV for incident energies of 1026 and 833 meV instead of at the observed positions of 560 and 470 meV.

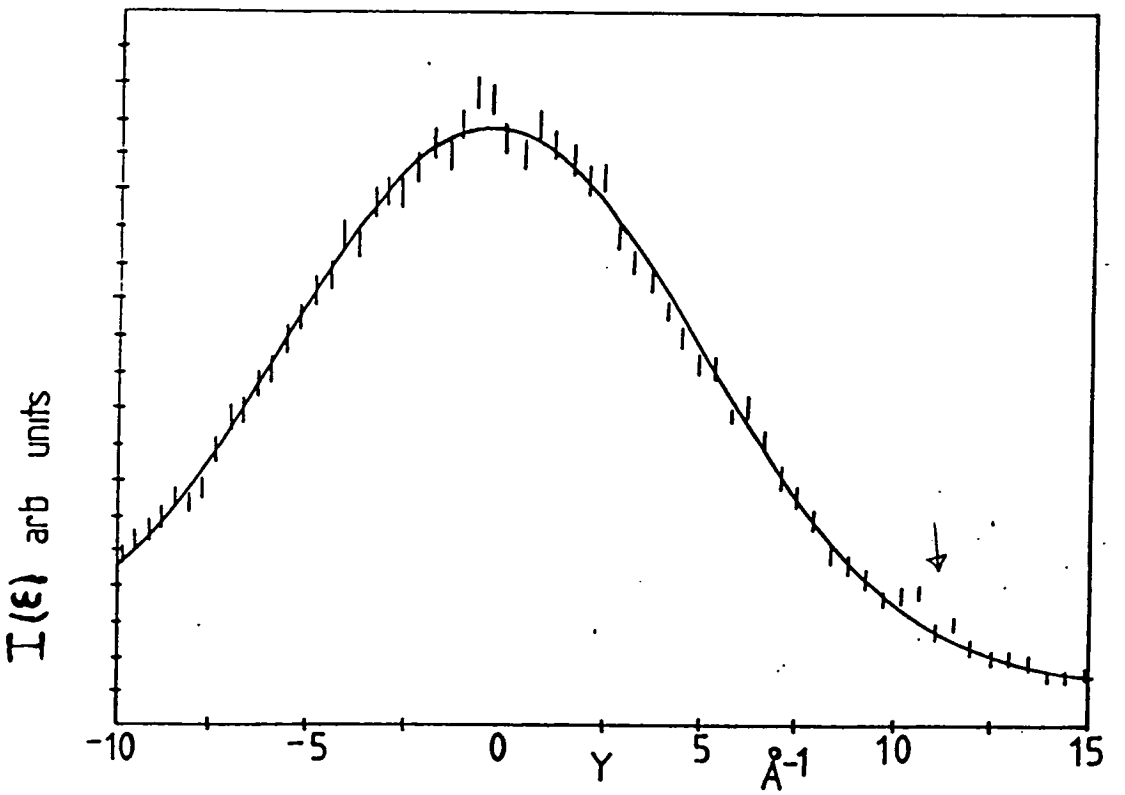

Figure (2.13). The Gaussian fit to the data (solid line) is a guide to the eye and shows clearly a feature at $Y = 10Å^{-1}$.

function of y. On the assumption that the final state interactions are small and may be neglected, the data in Figure (2.12) were combined and are shown in Figure (2.13). The gross features are similar to those observed in Figure (2.12) and a feature at y = 10 $\mathring{A}^{-1}$ is clearly shown.

2.5.2 The incoherent dynamic structure factor

The incoherent dynamic structure factor for a cubic Bravais lattice is given by equation (2.12) in Section(2.2.1). Results for the energy dependence of $S^{inc}(Q,\epsilon)$ at constant wavevector transfers were obtained in the range $10\mathring{A}^{-1} < Q < 50\mathring{A}^{-1}$ by direct numerical integration using the g(ϵ) inferred from neutron scattering data at 100K, room temperature, and for a Debye solid. A damping factor, $e^{-s\epsilon^2}$, was included in equation (2.12) so that the integrand converged to zero at infinity. The effect of this term in the calculation is to give a Gaussian shaped broadening to the energy spectrum. The program to calculate $S^{inc}(Q,\epsilon)$ was written in Fortran 77 and called SCATFUNC. This program was compiled and run on the ICL 2900 computer belonging to the University of Edinburgh. The value of s was chosen sufficiently small that the distortion introduced into the lineshape was negligible. The first energy moment of the calculated $S^{inc}(Q,\epsilon)$ was compared with the analytical result, $\frac{\hbar^2 Q^2}{2M}$, and found to be in good agreement.

The FWHM of $S^{inc}(Q,\epsilon)$ are plotted as a function of Q in Figure (2.9) (dotted line), and shows the scaling regime appears to be reached for $Q > 18\mathring{A}^{-1}$. The peak positions in Figure (2.8), dashed line , show small deviations from the recoil position for all Q and are in good agreement with those measured experimentally. This is a consequence of the final state interaction's greater effect on the peak position than on the FWHM (Sears (1972)). Nevertheless experiments with a finite experimental resolution are effectively in the scaling regime for wavevector transfers $> 25\mathring{A}^{-1}$.

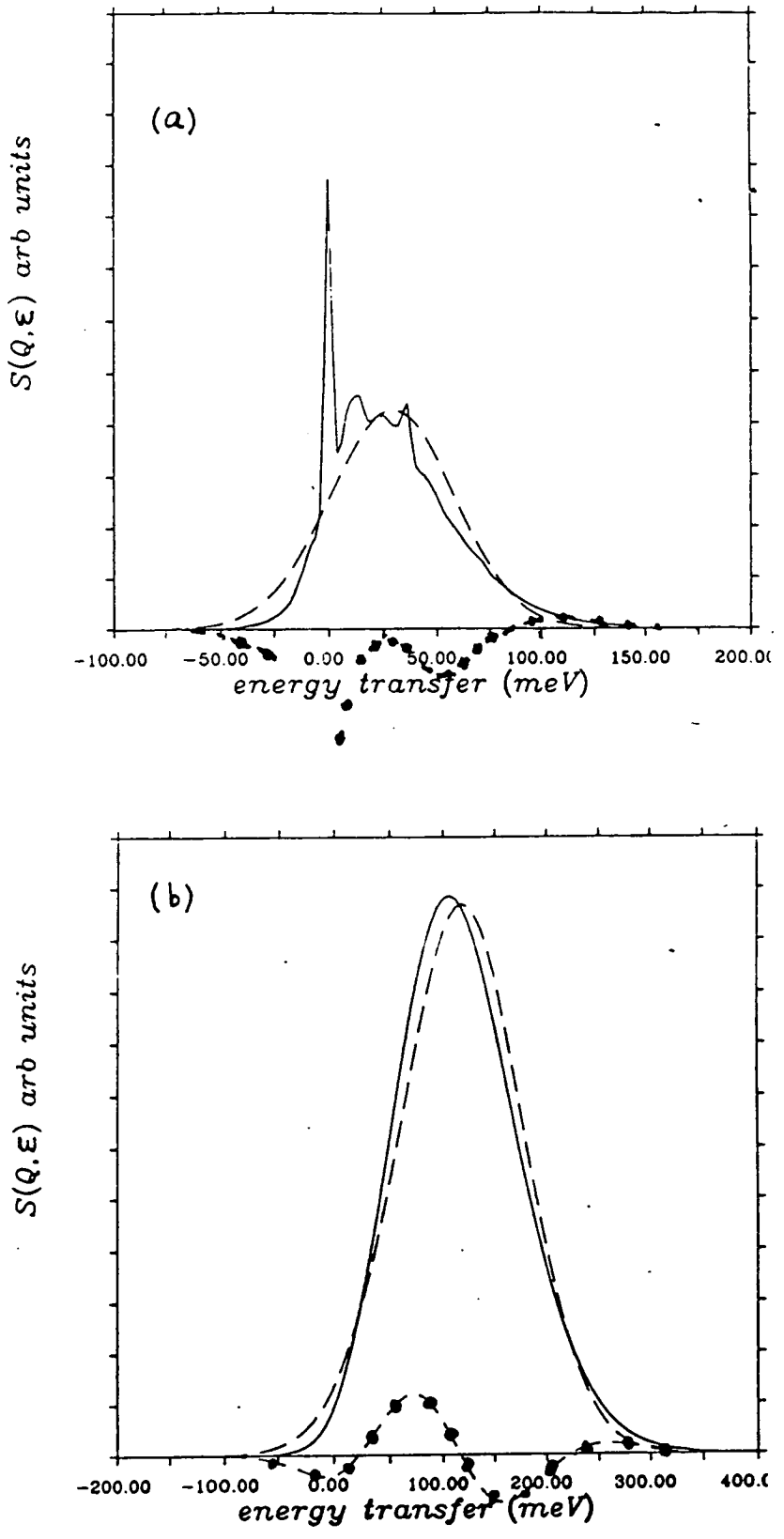

Figure (2.14)(a) shows $S^{inc}(Q,\varepsilon)$ calculated from equation (2.12), solid line, and the IA result, $S^{IA}(Q,\varepsilon)$, dashed line for a sample temperature of 100K and Q = 10 $\mathring{A}^{-1}$. Deviations from the IA result $((S^{IA}(Q,\varepsilon)-S^{inc}(Q,\varepsilon))xQ)$ are shown by the dot-dash line. Structure from the phonon density of states is clearly visible in the figure. (b) The magnitudes of the deviations from the IA result at Q = 20 $\mathring{A}^{-1}$ are shown to be less, dash-dot line, and the lineshape has no discontinuities.

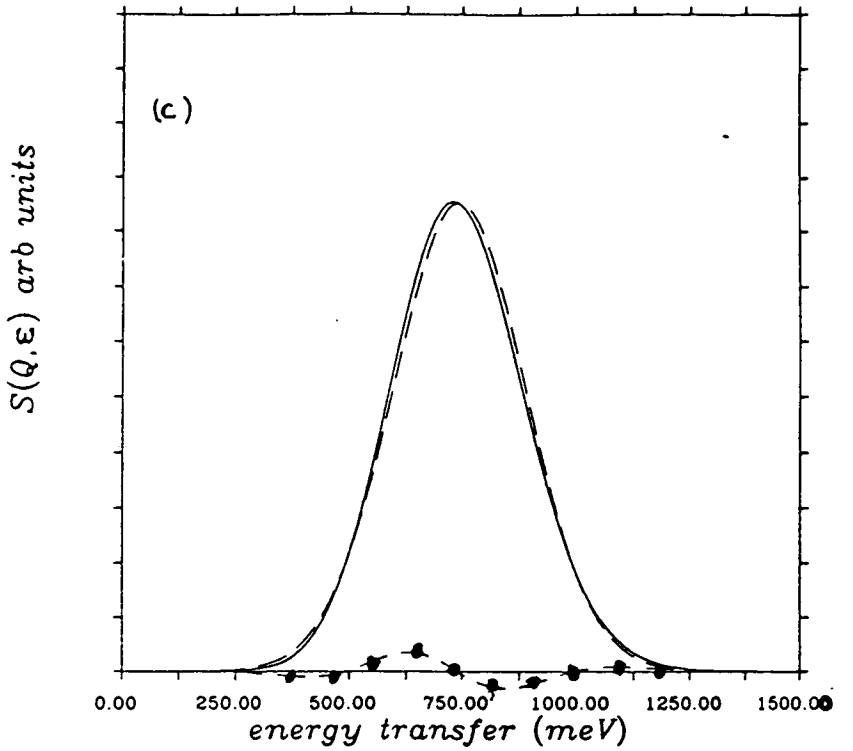

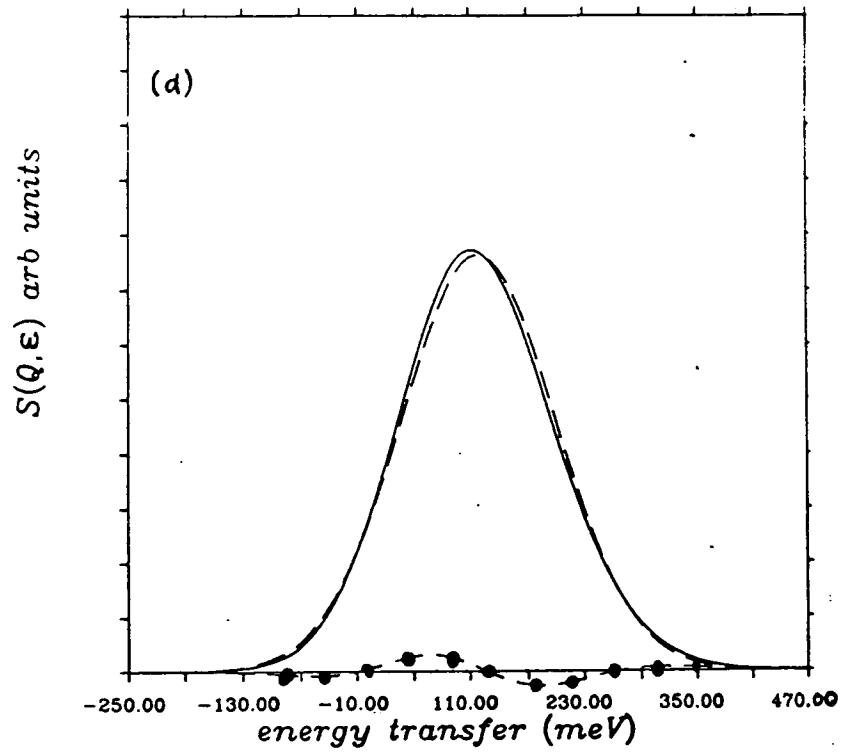

Figure (2.14) (c) shows $S^{inc}(Q,\omega)$ calculated from equation (2.12), solid line, and the IA result, $S^{IA}(Q,\omega)$, dashed line for a sample temperature of 100 K and Q = 50 $\mathring{A}^{-1}$. The IA is shown to be a very good approximation as judged by both the continuity of the lineshape and magnitudes of the deviations, $((S^{IA}(Q,\omega)- S^{inc}(Q,\omega))xQ)$, shown by the dash-dot line. (d) At a sample temperature of 300K and Q = 20 $\mathring{A}^{-1}$, the deviations from the IA result are less than at 100K and Q = 20 $\mathring{A}^{-1}$.

Figure (2.14a) shows the calculated $S^{inc}(Q,\epsilon)$ for Q=10 $\AA^{-1}$ (solid line) possesses structure, which originates from the peak in g(ϵ) due to the zone boundary phonons, that is not reproduced in the IA (dashed line). At Q=20 $\AA^{-1}$, Figure (2.14b), the structure in the lineshape has disappeared. The peak position is however displaced from the recoil position and the intensity in the "wings" of $S^{inc}(Q,\epsilon)$ is enhanced on the high energy side of the recoil position and depressed on the low energy side. As Q increases the IA becomes a progressively better approximation as shown in Figure (2.14c) for Q=50$\AA^{-1}$. Figure (2.14d) shows the final state interactions present at room temperature are much smaller than at 100K and is in qualitative agreement with equation (2.15).

The FWHM of S(Q,ϵ) for a Debye model g(ϵ) was calculated using the Debye temperature determined by specific heat measurements (Martin (1959)) The calculated FWHM for $g_{Deb}(\epsilon)$ and $g_{BVK}(\epsilon)$ were the same within error , and it is concluded that the FWHM is not sensitive to the precise form of g(ϵ).

2.5.3 Discussion and conclusions

Neutron scattering measurements were performed for energy and wavevector transfers in the range 227 meV to 1985 meV and 16 $\AA^{-1}$ to 50 $\AA^{-1}$ respectively with a sample temperature of 100 K. The dynamic structure, factor is characteristic of the region where the IA is valid as determined by the wavevector scaling properties of the peak position and width, that were parameters of the Gaussian fitted to the spectra, for wavevector transfers greater than 25 $\AA^{-1}$. Plots of several spectra made with higher statistical precision as a function of y are a universal function of y, and it is concluded that the IA is closely approximated for wavevector transfers greater than 25 $\AA^{-1}$.

The FWHM of the scattered neutron distribution was 14% larger than the value calculated assuming the IA is valid and using a harmonic model density of states(Smith (1968)). A calculation of the incoherent dynamic structure factor using

the same model density of states showed that the width discrepancy was not a failure of the IA for a harmonic crystal. Therefore the discrepancy between the FWHM determined from the model fitted to the data and the IA result may be due to either an incorrect model density of states, or a systematic error in the model fitted to the data. Each of these is discussed below in more detail.

It is difficult to estimate the absolute size of the systematic error that resulted from approximating the resolution function and dynamic structure factor at constant angle by a Gaussian, and the accurate subtraction of the background, but previous experiments using HET suggest that this error is less than 5%.

The accuracy of the model density of states derived for a harmonic crystal depends on the validity of the force constant model employed, and the precision of the experimental technique used to determine the phonon frequencies throughout the Brilloiun zone. The finite experimental resolution with which neutron scattering measurements are performed can lead to systematic errors in the phonon frequencies and the derived density of phonon states(Cooper and Nathans (1968), Cowley and Pant (1970)). Smith (1968) has not applied a resolution correction to his data, and the Debye temperatures determined from the model density of phonon states and specific heat measurements (Martin (1959)) differ by 10%. Beg and Nielson (1976) have remeasured the phonon dispersion relation along the [1,1,1] cubic crystallographic direction at 110 K, with much higher resolution. They found that the discrepancy between the measured and model calculations of Smith(1968) to be approximately 18%. Although the interpretation of the phonon dispersion relations in terms of the BVK model for metals is questionable, the objective was to reproduce the phonon frequencies throughout the Brilloiun zone accurately. More recent models,(Krebs (1965), Ramamurthy and Satishkumar (1985), Jani and Cohel (1982)) which are physically more plausible,were rejected in favour of the BVK model because the calculated phonon frequencies were in better agreement with the measured frequencies. However, the FWHM is relatively insensitive to the precise distribution of the density of phonon states, and it may be estimated, by assuming a Debye model density of states with the correct Debye temperature, that the discrepancy in Debye temperatures can account for only 3 % of the width anomaly.

Bednarz and Field (1982) have made an x-ray diffraction study for a single crystal of lithium. Measurements of the integrated intensity of the Bragg peaks as a function of Q and temperature have been analysed for anharmonic effects in the lattice vibrations by using a temperature factor based on an effective single body potential ,V,of the form (Willis (1975))

$$V(u) = \frac{\alpha^2 u}{2} + \alpha^2 u^4 + \delta(u_x^4 + u_y^4 + u_z^4 - \frac{3u^4}{4})$$

where u is the displacement of the atom from the equilibrium position. The harmonic force constant is given by α and the higher order terms are constrained by the symmetry of the crystal. They find a small but significant anisotropic component, δ, in the one particle potential. However it is known (Keating et al(1971)) that the electron cloud distorts in a manner to compensate for the anharmonic motion. Consequently this effect may be significantly larger than that measured by the x-ray technique. Neutrons are sensitive only to the nuclear motion and therefore give a more accurate measure of the anharmonic motion. McCarthy et al(1980) have performed a neutron diffraction experiment on high purity polycrystalline lithium at temperatures between 4.2 and 300K. Their data clearly show a dramatic increase in the intensity of the high angle reflections as the temperature is lowered from 293K to 78K. The anharmonic terms in the Debye Waller factor were extracted from the angular dependence of the incoherent elastic scattering. Because the sample was polycrystalline the Debye-Waller was assumed to have the following functional form, ((Willis 1975) and equation (2.11))

$$W(Q) = aQ^2 + bQ^4$$

where b is a phenomenological term that represents the anharmonic effect for a centrosymmetric crystal. A large anharmonic contribution to the Debye Waller factor is reported from 4.2 to 293K. In contrast the Debye temperature, θ_D, determined from specific heat measurements (Martin (1959)) suggest the anharmonic contribution at 100 K to the crystal energy is negligible. However, θ_D is quite insensitive to the high frequency tails introduced into g(ϵ) by anharmonicity, because it is proportional to, $\int_0^\infty \frac{g(\epsilon)}{\epsilon} coth(\frac{\epsilon}{k_B T}) d\epsilon$.

It is concluded that the interatomic potential in lithium is significantly anharmonic. Moleko and Glyde (1985) have shown that the main effect of anharmonic terms in the interatomic potential is to increase the mean atomic kinetic energy over the value obtained for a purely harmonic potential. Physically, the increase in atomic restoring force is significant only for large amplitude, high energy vibrations because the anharmonic forces are appreciable only at short ranges. This results in a relative increase in the model density of states at the largest frequencies and, from Section 2.2.1, an increase in the mean atomic kinetic energy. It is expected that the momentum distribution remains almost Gaussian, and that the main effect of anharmonicity is to increase the mean kinetic energy, or equivalently T_{eff}. It is therefore concluded that deviations from the IA for a harmonic crystal have been observed for lithium, and are due to significant anharmonic effects in the interatomic potential.

2.5.4 Further work

Further investigations require a single crystal of lithium to understand the origin of the structure in the data, preferably a crystal isotopically enriched in Li^7 to obtain adequate counting statistics. The sample holder should be constructed with tin or tantalum endplates to reduce the magnitude of the sample holder scattering. It would also be useful to perform a neutron diffraction experiment at 100K for a lithium single crystal. From measurements of the integrated Bragg peak intensities the size and Q dependence of the Debye-Waller factor could be determined. This would allow the density of states to be checked and a test for the presence of anharmonicity at 100K to be made.

Chapter 3

Isotropic Ferromagnets

3.1 Introduction

To describe the complete dynamical behaviour of a many body system it is necessary to know the explicit form of the Hamiltonian. In general this is too complex for solution and consequently it is normal to consider a model Hamiltonian which includes only those features considered the most important. It has been fruitful to study the properties of ferromagnetic materials in terms of the Heisenberg model. The model consists of a regular array of localised spins that are coupled together by phenomenological constants, called exchange interactions, that are determined by the theory with a set of experimental results. From this model other experimental results may be explained and related phenomena correlated. In particular the properties of the longitudinal susceptibility of isotropic ferromagnets have attracted a great deal of theoretical activity much of which has still not been vindicated by experiment.

It has been shown (Holstein and Primakoff (1940), Herring and Kittel (1951)) that the longitudinal susceptibility diverges for $T < T_c$ as the applied field $H^{-\frac{1}{3}}$ because of the transverse spin fluctuations. Renormalisation group techniques

(Brezin and Wallace (1973)) have shown that this result is valid up to T_c.

Kawasaki and Mori (1961,1962,1967) using the the Greens function formalism have obtained the result that the wavevector dependence of the static susceptibility diverges as $\frac{1}{q}$[1] in zero applied field. This result was also calculated by the renormalisation group technique by Mazenko (1976).

No consensus has been reached for the frequency dependence of the longitudinal susceptibility. Villain (1971) has calculated that the response function has a peak at each of the two spin wave frequencies and Vaks et al(1968) obtained a similar result with an additional peak centered at zero frequency due to spin diffusion. Mazenko (1976) has predicted a single peak in the response function centred at zero frequency that diverges at zero wavevector as $\frac{1}{\sqrt{\omega}}$.

The divergences in the longitudinal susceptibility as a function of wavevector, frequency and applied field may be shown to be a direct consequence of the absence of an energy gap in the spin wave excitation spectrum at $q = 0$. The absence of a gap follows from the application of Goldstone's theorem (Goldstone (1961)) which asserts "when a symmetry group that is broken is continuous (translational or rotational) a new excitation may appear whose frequency goes to zero at small wavevectors." In the low temperature ordered phase the spins have a preferred direction of orientation whereas the Heisenberg Hamiltonian is rotationally invariant, consequently we have a broken symmetry.

Although it has been known for many years that the longitudinal and transverse components of the magnetic susceptibility can be separated by the use of polarised neutrons (Moon et al 1966) most experimental investigations have been performed with unpolarised beams. This was because of the limitations imposed by the neutron flux from available reactor sources and various spectrometer components. Collins et al (1969) examined iron and Minkiewicz et al (1969) examined nickel close to T_c and observed only spin wave peaks with-

[1] The reduced wavevector transfer q is defined in Section (3.2)

out any evidence of a central peak. Als-Nielsen et al (1976) and Dietrich et al (1976) performed a very thorough study of EuO and EuS and identified a small contribution for $T = T_c$ and just below T_c as longitudinal fluctuations with a Lorenztian form in wavevector. Their inelastic scattering measurements below T_c showed only spin wave peaks and they concluded that the longitudinal susceptibility had an inelastic form similar to the spin wave spectrum.

The development of high flux beam reactors, in particular the Institute Laue Langevin (ILL) at Grenoble in 1971, and high efficiency polarising devices have made inelastic neutron scattering experiments with polarisation analysis feasible. Recently Mitchell et al (1984) have reported neutron inelastic scattering measurements with polarisation analysis for the macroscopically isotropic ferromagnet Pd(10%)Fe. Their measurements show clearly the frequency dependence of the longitudinal susceptibility is quasielastic. However they were unable to observe the predicted divergences in the longitudinal susceptibility as a function of q, ω and H. This may have been a consequence of the rather large field required to saturate the sample around ,0.5T, and the smearing of the transition due to concentration gradients in the sample. At present it is therefore important to know whether the predicted divergences have gone unobserved because of experimental limitations or because the isotropic Heisenberg model is unrealistic.

3.2 Scattering theory

In this section the double differential cross section for the scattering of a polarised neutron beam by a system of localised magnetic moments, S_i ,at lattice site l is given. A more detailed account of the results presented and the Heisenberg model may be found in the monograph by Lovesey (1984).

The unpaired electron neutron interaction, $V_m(Q)$, for an ion with no orbital contribution to the magnetic moment is given by:

$$\left(\frac{2\pi\hbar^2}{m_n}\right)\left(\frac{\gamma e^2}{m_e c^2}\right)\hat{\sigma}\sum_i e^{iQ.r_i}\tilde{q}\otimes(\tilde{s}_i\otimes\tilde{q}) \qquad (3.1)$$

where $\hat{\sigma}$ is the Pauli spin matrix, $\otimes$ the vector cross product and r_i the electron co-ordinate. Physically this implies that only the components of the magnetisation density perpendicular to the scattering plane give rise to scattering. Substituting $V_m(Q)$ into equation (1.12) we obtain the result:

$$\frac{d^2\sigma}{d\Omega d\varepsilon} = \left(\frac{\gamma e^2}{m_e c^2}\right)^2 \frac{k_f}{k_0}\left|\frac{1}{2}gF(Q)\right|^2 \sum_{ll'} e^{iQ.(l'-l)}\frac{1}{2\pi\hbar}\int_{-\infty}^{\infty} dt e^{-i\omega t}\frac{1}{4}[(1+(\hat{Q}.\hat{H})^2+2(\hat{P}.\hat{Q})(\hat{Q}.\hat{H})$$

$$< S_{l'}^-(0)S_{l'}^+(t) > + (1+(\hat{Q}.\hat{H})^2 - 2(\hat{P}.\hat{Q})(\hat{Q}.\hat{H}))< S_l^+(0)\,S_{l'}^-(t) >] \qquad (3.2)$$

where F(Q) is the magnetic moment form factor, the spin angular momentum operators $S^{\pm}$ are raising and lowering operators that change the total z component of the spin by one unit and g is the Lande factor. $\hat{P},\hat{Q}$ denote unit vectors where P is the neutron beam polarisation and Q the wavevector.

For the experimental configuration discussed in Section (3.3), with the applied field H perpendicular to Q and parallel to P, the cross section is:

$$\frac{d^2\sigma}{d\Omega d\epsilon} = \left(\frac{\gamma e^2}{m_e c^2}\right)\frac{k_f}{k_0}\left|\frac{1}{2}gF(Q)\right|^2\sum_{ll'}e^{iQ(l-l')}\frac{1}{2\pi\hbar}\int_{-\infty}^{\infty}dt e^{-i\omega t}$$

$$\frac{1}{4}[< S_l^-(0)S_{l'}^+(t) > + < S_l^+(0)S_l^-(t) >] + < S_l^z(0)S_l^z(t) > \qquad (3.3)$$

Using the fluctuation dissipation theorem (Lovesey(1984)) the first two correlation functions maybe shown to be related to the transverse susceptibility and the third correlation function to the longitudinal susceptibility. The longitudinal scattering involves no change in the incident neutron spin state (Moon et al(1966)) and the transverse scattering gives a π change in spin orientation. For completeness it is noted that coherent neutron scattering occurs without a change in the neutron spin state and that incoherent scattering may occur without a change in the neutron spin state.

The magnetic susceptibility $\chi(q,\omega)$ is related to $S(q,\omega)$ by: $\mathrm{Im}\,\chi(q,\omega) = \frac{2\pi\mu_B}{\hbar}S(q,\omega)\left(e^{-\frac{\hbar\omega}{K_BT}}-1\right)$

It is convenient to write the wavevector transfer $Q = \tau + q$, where τ is a reciprocal lattice vector of the crystal structure, and q is the reduced wavevector transfer.

3.3 Experimental background

The neutron inelastic scattering measurememnts were performed using the IN12 triple axis spectrometer at the ILL. In this section we shall discuss both the generic features of this instrument, Section(3.3.1) and those which are specific ,Section (3.3.2). Both sections are quite brief because many detailed reviews covering the points discussed already exist (Dorner(1982)).

3.3.1 Triple crystal spectrometer

A schematic plan of a triple axes spectrometer is shown in Figure (3.1). The wavevector of the incident radiation is determined by Bragg reflection, through an angle $2\theta_M$, and the wavevector of the scattered radiation obtained by Bragg reflection, through an angle $2\theta_A$, from an analyser crystal. Maximization of the reflected intensity and a favourable value for the Bragg angle are important criteria in determining the choice of crystal for the monochromator and analyser. Larger values for θ_M or θ_A result in a smaller spread in the selected wavevector for a given mosaic spread. Clearly intensity and resolution are optimised when the angular divergence of the beam transmitted by the collimators is matched to the mosaic spread of the preceeding crystal. Further collimation may improve the resolution but result in a significantly lower transmitted intensity.

The setting of the spectrometer at a given point (Q,ω) determines the required incident and final neutron wavevectors according to the energy and momentum conservation conditions given by equations(1.10) and (1.11). These values for the neutron wavevector then give the values for the monochromator, analyser and sample angles. By specifying the angle,ψ, between the sample reciprocal axes and the wavevector transfer Q the spectrometer configuration is completely determined. However because only the three variables ω, and two components of Q

in the scattering plane are required it is usual to fix one of the variable instrumental parameters k_0 or k_f. . It is normal to chose a sequence of points (Q, ω) where one variable is fixed. This is known as a constant Q or ω scan and each possesses important advantages (Dorner(1982)) over a scan where Q and ω vary simultaneously.

There is a problem which is generic to all triple axis spectrometers. If a monochromator (analyser) is set to reflect neutrons of wavevector k_0 it follows from Braggs law that it will also reflect neutrons with a wavevector k_0/n, where n is an integer. The solution adopted depends on the the spectral output characteristics of the source and the detector used to detect the scattered radiation. This point is discussed in more detail in Section (3.3.5) and (4.4).

3.3.2 Experimental Background

The neutron inelastic scattering measurements were performed using the IN12 triple axis spectrometer at the ILL. Epithermal neutrons, which are produced in the core of the nuclear reactor, come into equilibrium with an adjacent moderator while passing through it and undergoing collision processes. The outgoing neutrons have an approximately Maxwell-Boltzmann distribution of energies, the peak of which is determined by the moderator temperature. The neutron flux incident on the IN12 spectrometer is in equilibrium with a liquid deuterium moderator at $T = 25K$. The peak in the neutron energy distribution corresponds to a wavelength of $\lambda \approx 5\mathring{A}$ and effectively enhances the flux at longer wavelengths of the incident spectrum. Consequently the IN12 spectrometer is especially suitable for making high resolution measurements at low frequency transfers. A neutron guide tube transmitted the neutron beam from the moderator to the spectrometer.

The setting of the turntable on which the monochromator, sample and analyser

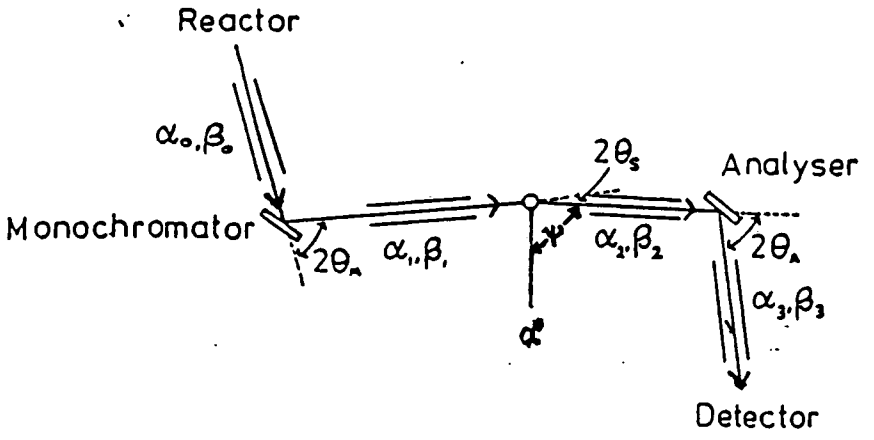

Figure 3.1: Plan view of the triple axis neutron spectrometer (schematic). α, β are the horizontal and vertical collimations respectively. $2\theta_m, \theta_s$ and $2\theta_A$ are the scattering angles at the monochromator, sample and analyser. (Neutron Research Facilities at the High Flux Reactor (1983))

are mounted and also the angles of the three spectrometer arms were under computer control, and enabled scans to be made automatically along predefined directions in reciprocal space. A monitor, which produced an electrical signal in proportion to the incident neutron flux (Bacon (1975)), was fitted between the mononchromator and sample. This allowed the counts obtained for a fixed time at each point in a scan to be properly normalised and the effect of fluctuations in the incident beam intensity to be disregarded. In these experiments the incident wavevector $|k_0|$ was held fixed and the measured double differential cross section was $\frac{d^2\sigma}{d\Omega d\theta_A}$. The number of counts in the detector is then proportional to $k_f^3 cot\theta_A S(Q,\omega)$ (appendix 1).

Unfortunately, the signal from the detector is a summation over the number of neutrons with the selected beam energy and integral multiples of this energy. To prevent these neutrons contributing to the signal a polycrystalline filter was fitted between the sample and monochromator. No coherent elastic scattering will occur if the neutron wavelength is twice the largest interplanar spacing in the mate-

rial. The lattice parameter of beryllium has a suitable value for transmitting a neutron beam having a wavelength of $5\mathring{A}$, and attenuating the higher harmonic wavelength components. Cooling the filter to 77 K increased the efficiency of the Bragg reflection process because of the dramatic decrease in the Debye-Waller factor with temperature. The possibility of transmission due to multiple scattering was eliminated by absorbing slits inserted in the beam direction. The detector was a high efficiency (80-90%) $^{10}BF_3$ gas detector.

3.3.3 Experimental method

The experimental measurements were performed at the ILL and were carried out in collaboration with Dr P W Mitchell, Dr H A Mook and Dr R Pynn. This section is divided into two subsections, the first of which describes europium oxide, chemical formula EuO, and the second the experimental conditions.

3.3.4 Properties of EuO

The crystallographic structure of EuO is of the rock salt type shown in Figure(3.2). The divalent magnetic europium ions form a spherically symmetric $^8S_{\frac{7}{2}}$ spin state (Mathias et al (1961)) surrounded by an octahedral cage of non magnetic oxygen ions. This crystal structure leads to a ferromagnetic exchange interaction between the Eu^{2+} ions. On cooling below $T_c \approx 69K$(Als-Nielson et el (1976)) from the high temperature paramagnetic phase EuO becomes ferromagnetic down to the lowest temperature. NMR measurements (Dillon and Olsen (1964)) suggest that the octahedral crystal field gives rise to a preferred spin orientation along the $< 111 >$ direction, referred to a set of cubic axes. In addition to the small magnetic anisotropy neutron inelastic scattering measurements for the spin wave dispersion relation (Passel et al (1976)) suggest that the spin interactions, the physical mechanism of which is discussed by Kasuya (1970), are

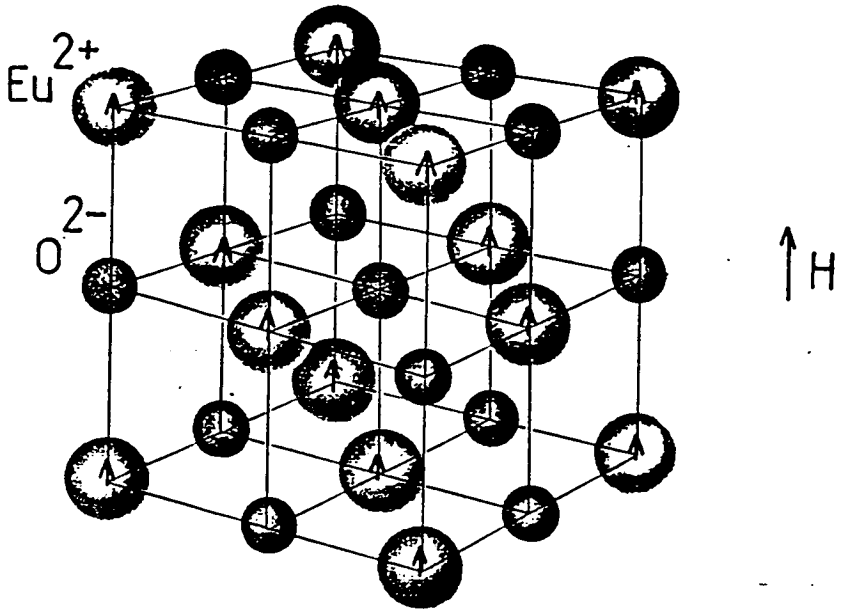

Figure 3.2: The nuclear and magnetic structure of EuO. At 73K the cell has lattice parameter a=b=c=5.12 $\AA$(Als-Nielson et al (1976)).

significant to next nearest neighbours. However, because the magnetic moment has no orbital component solid state effects are believed to be negligible, and the critical behaviour should be well described by the isotropic Heisenberg model.

3.3.5 Experimental conditions

In Figure(3.3) a schematic diagram of IN12 is shown. The incident beam was provided by a vertically focussed pyrolytic graphite (002) monochromator. Specular reflection from a supermirror bender placed on the first arm of the spectrometer produced a polarised beam. A Mezei-π-coil was mounted between the sample and the analysing crystal. When activated this caused the neutron spin polarisation to precess through exactly 180^0 on passing through the coil and allows spin flip and non spin flip cross sections to be determined. Energy and polarisation analysis of the scattered beam was performed with the (111) planes

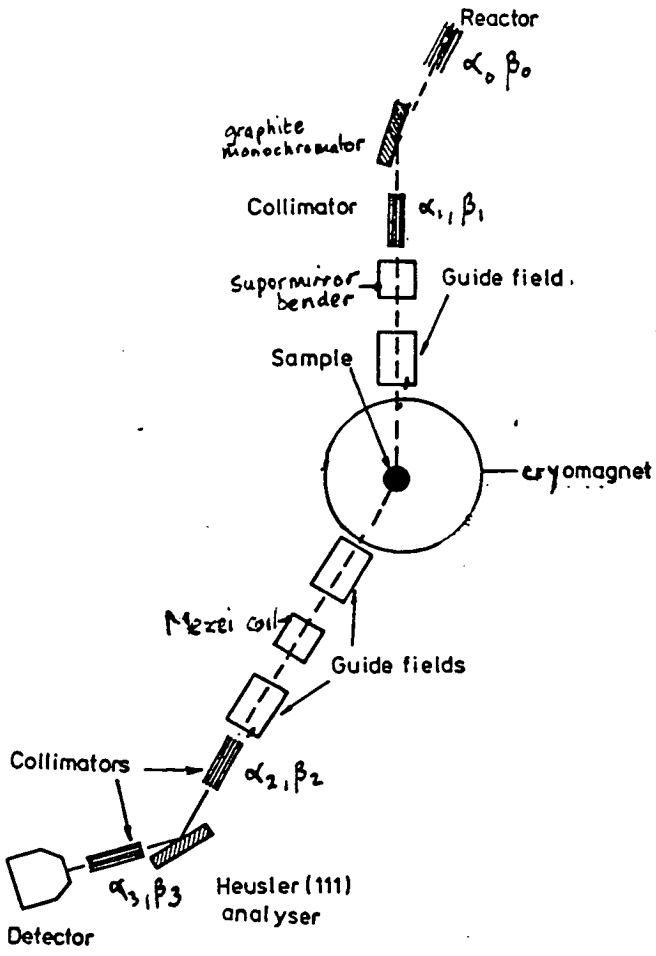

Figure(3.3) Triple axis spectrometer modified by the addition of a supermirror bender and Mezei coil for polarisation analysis. The instrumental parameters are, horizontal and vertical mosaic spread of mono, analyser and sample $(0.4^0, 1.5^0), (0.4^0, 1.5^0), (1.3^0, 1.4^0)$; horizontal and vertical collimation between mono and sample $(0.7^0, 2.0^0)$,sample and analyser $(0.5^0, 2.0^0)$; analyser and detector $(0.5^0, 9.0^0)$. The lattice spacing of the monochromator is 3.355 $\AA$, and the analyser, 3.437 $\AA$.

of a crystal of the Heusler alloy $CuMn_2Al$ in a vertical field of 0.2T. The polarising and analysing components of the spectrometer are more fully described elsewhere (Pynn (1984)). Ideally the devices reflect all neutrons of one spin polarisation and have zero reflectivity for the other component. In this case because the polarising action of the bender and the Heusler crystal are different, the spin flip cross section was measured without activating the coil. A fixed incident energy of 1.2 THz was used throughout the experiment and the collimation was 30′ before the sample, and before and after the analyser. The measured energy resolution from the diffuse scattering was 0.031 THz (FWHM).

The EuO crystal was in fact an assembly of four cleaved crystals, each of size 10mm x 10mm x 1mm. The crystals were prepared from EuO enriched to 99.9% in ^{153}Eu to reduce the neutron absorption from that of natural Eu of isotopic abundance 52% ^{153}Eu and 48% ^{151}Eu. Even so the scattering was always in reflection geometry as the penetration of the long wavelength neutrons used in the experiment, to obtain good energy and wavevector resolution, through the crystal was extremely small. Each crystal, a rectangular platelet with a (001) face normal, was mutually aligned to better than one degree and then clamped in the aluminium sample holder. The sample was placed in a cryomagnet with a $[0\bar{1}0]$ axis perpendicular to the scattering plane. The temperature stability was $\pm 0.02K$ and was accurate to better than $\pm 0.01K$ absolute. The cryomagnet could provide a magnetic field from 0 to 4T. Most of the data were collected with a magnetic field of strength $0.1T$ to align the ferromagnetic domains ,that occur below T_c, in the field direction. Clearly in a multidomain sample the terms transverse and longitudinal fluctuations become meaningless.

Constant Q scans were perfomed as a function of temperature ,magnetic field and wavevector around the (002) Bragg reflection. A major problem of working around this reflection arises from the contamination of the signal by the nuclear Bragg scattering which is relatively very intense. Unfortunately the scattering geometry was such that other more favourable reflections were not accessible.

3.4 Spectrometer resolution and analysis

The intensity of the scattered neutrons when the triple axis spectrometer is set to observe an event at (Q_0, ω_0) is related to $S(Q,\omega)$ by a convolution with the instrumental resolution function R(Q,ω):

$$I(Q_0,\omega_0) = \int R(Q-Q_0, \omega-\omega_0) S(Q,\omega) dQ d\omega \tag{3.4}$$

where

$$R(X) = R(X_o) e^{-(\frac{1}{2} X.\widetilde{M}.X)} \tag{3.5}$$

and $X = (dQ, d\omega)$. The result for the resolution function (Cooper and Nathans (1968)) was derived assuming that the transmission function of each spectrometer component could be represented by a Gaussian function. Full details of the normalisation factor R $(X_0 = Q_0, \omega_0)$ and the relation between the components of the matrix $\widetilde{\mathrm{M}}$ and spectrometer parameters, mosaic β, collimator α as shown in Figure (3.1), are given by Dorner (1972) and by Chesser and Axe (1973).

Unfortunately at present it is not possible to incorporate analytically the effects of the supermirror bender into the resolution formalism described previously. This is mainly a consequence of the restriction placed on the angular divergence of the incident beam from the monochromator mosaic reflected by the supermirror bender and the correlation of this restriction with the wavelength of the incident neutrons. However since $S(Q,\omega)$ for a Bragg peak is $\delta(Q-\tau)\delta(\omega)$ an empirical measurement of the resolution function was made by performing longitudinal and transverse scans through the (002) Bragg reflection as a function of wavevector and energy. A Fortran program called Rescal using the values given in Figure(3.3) for the spectrometer collimations and mosaics calculated the ellipsoid of revolution within the Cooper Nathans formalism. The input values of the geometric collimations α_1 and α_2 were adjusted until a best approximation to the experimentally determined resolution function was obtained. These values were held fixed in all the subsequent data fitting. The projection of the

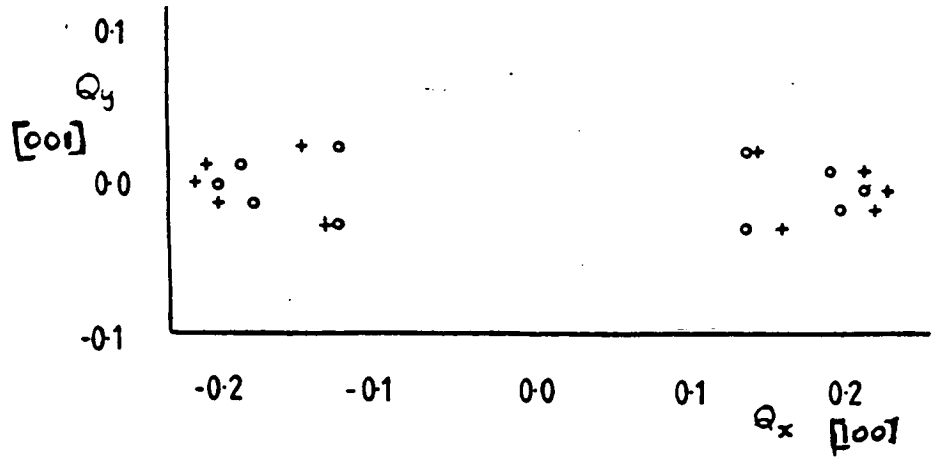

Figure 3.4: Projection of four dimensional resolution function at the (002) Bragg relection. The surface of the ellipsoid defines the locus of points for which the resolution function has the value $\frac{1}{2}R_0$. Both axes are in reciprocal lattice units, + experimental data, o calculated data

resolution ellipsoid along the Q_x and Q_y directions is shown in Figure (3.4). The agreement is shown to be satisfactory, similar fits were obtained for projections of Q_x or Q_y as a function of ϵ.

The analysis procedure involved a parameterised form for $S(Q,\omega)$ over the range of Q,ω concerned, and fitting the convolution with the resolution function , equation(3.4), evaluated at all the points on the scan , to the observed neutron distribution.

Even with a modern serial computer such a procedure requires considerable time. Such a task is ideally suited to the ICL distributed array processor (DAP) which is a single instruction multiple data stream machine. The parallel architecture of the DAP allows the parallelism of the analysis procedure viz the repeated calculation of the resolution function-dynamic structure factor convolution, equation (3.4), to achieve a very significant increase in the speed of program execution. The program used was called Shamgar (Mitchell and Dove (1985)) and it allows a simultaneous refinement to many sets of experimental data by a non-linear least squares fit (Bevington(1969)) A typical data set containing twelve scans, each scan having around twenty points, required 120 's of DAP[1] cpu time. This

[1] DAP cpu time is measured in seconds (s)

is at least an order of magnitude faster than a serial computer such as the ICL 2900. The errors quoted on the fitted parameters include those from the statistical uncertainities in the data and the values of the parameters which are fixed in the fitting procedure.

3.5 Results

All the wavevector scans presented in this section are in reciprocal lattice units unless otherwise stated. The Curie temperature,T_c, was measured as 73K from the peak of the non spin flip cross section as a function of temperature at a wavevector 0.05 $\AA^{-1}$ from the (002) Bragg reflection with an applied field of $0.1T$. Initial measurements characterised the form of the scattering above and below T_c for the spin and non spin flip scans. A constant wavevector scan for $q = 0.12\AA^{-1}$ above T_c in $0.1T$ applied field showed broad quasielastic lines of equal width and height in both spin flip, Figure (3.5), and non spin flip, Figure (3.6), cross sections. These peaks are superimposed on a flat background, with an additional resolution limited, elastic signal in the latter case. The transverse and longitudinal critical fluctuations are expected to be identical above T_c so that broad quasielastic signal in the spin flip channel is identified as the longitudinal susceptibility. Scans at similar wavevectors below T_c in the same applied field show the general form of the longitudinal fluctuations remain the same below T_c, with a broad quasielastic line centred at $\epsilon = 0$ superimposed on a sharp elastic component Figure (3.7). Figure (3.8) shows the transverse fluctuations are now radically different in character, with two well resolved peaks at non zero energies, which are identified as the two inelastic spin wave peaks.[1]

To determine the wavevector dependence of the longitudinal susceptibility a

[1] The dynamic structure factor for spin waves, equation (3.6), shows that at fixed wavevector, an energy scan should have two two peaks centred at $\pm\omega_o$, where ω_o is the spin wave frequency. It follows from the model spin wave dispersion relation $\omega_o = Dq^2$ that the seperation in peak position should increase with wavevector. This is consistent with the experimental results.

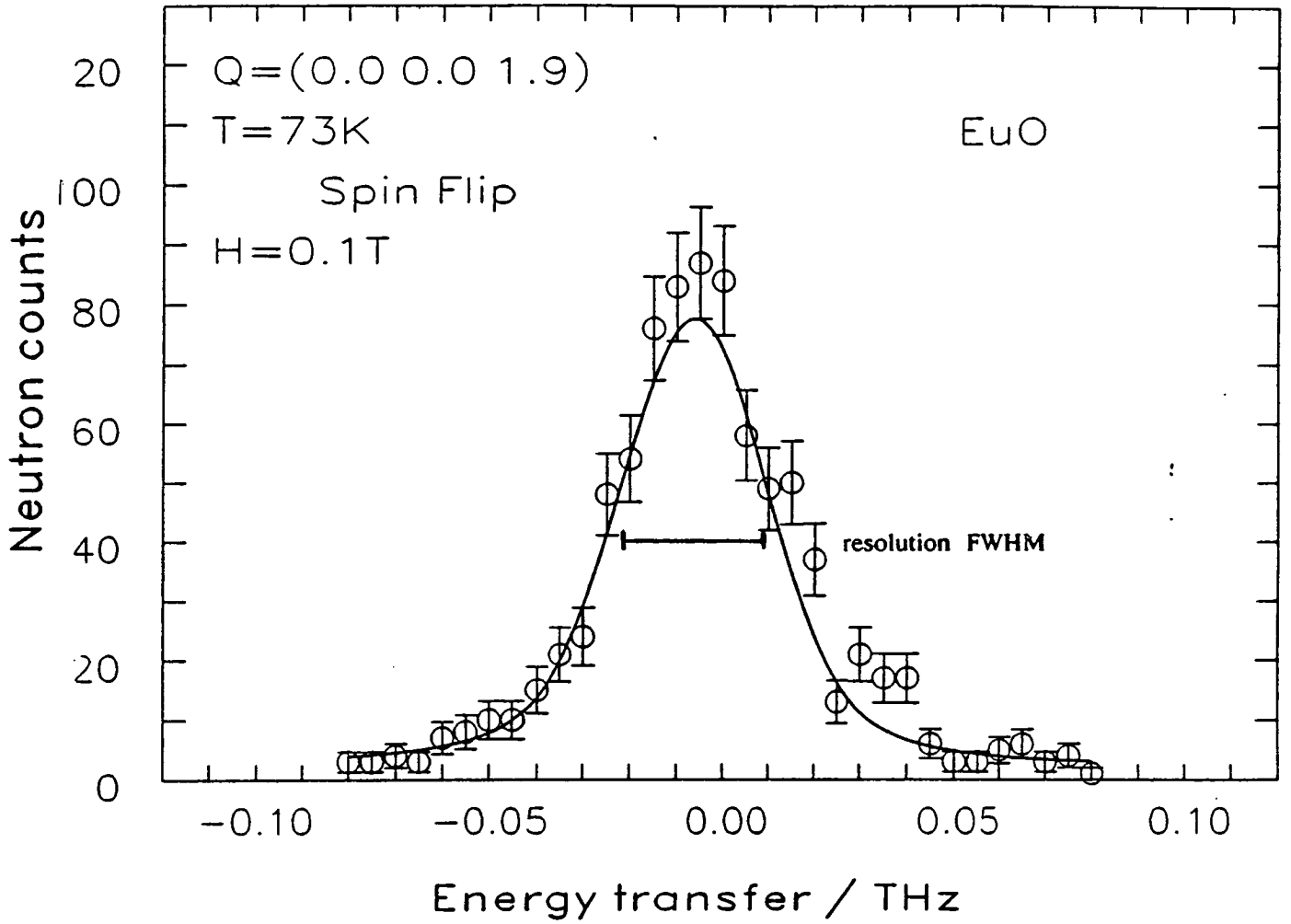

Figure(3.5) shows typical inelastic spectra obtained using polarisation analysis with a standard triple axis crystal spectrometer. The incoherent elastic component is around 15% of the total cross section. The experimental conditions used are noted by the insert. The solid line represents a smooth interpolation through the best fit to the points , shown with statistical errors, as discussed in Section (3.4).

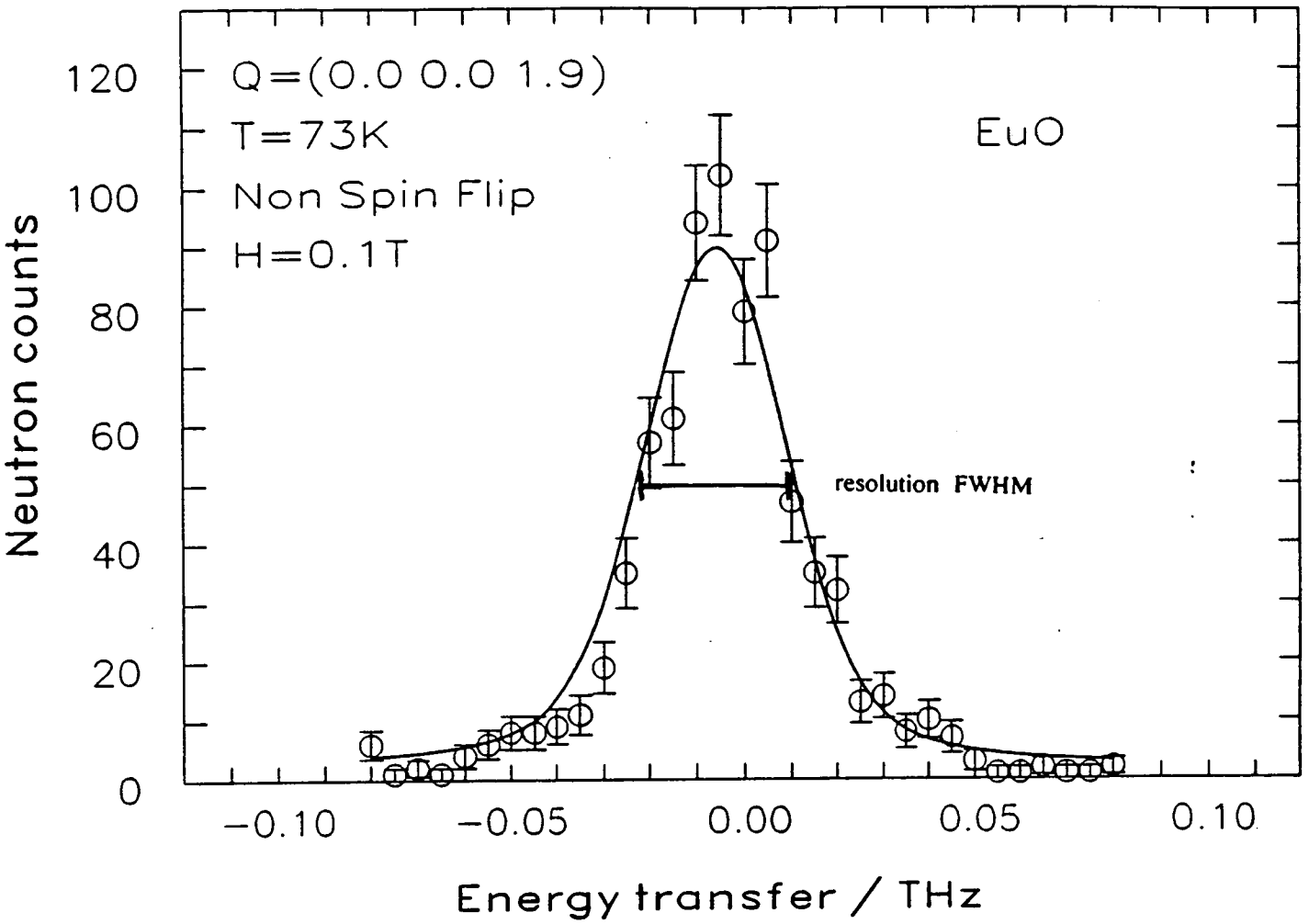

Figure(3.6) shows typical inelastic spectra obtained using polarisation analysis with a standard triple axis crystal spectrometer. The incoherent elastic component is around 15% of the total cross section. The experimental conditions used are noted by the insert. The solid line represents a smooth interpolation through the best fit to the points, shown with statistical errors , as discussed in Section (3.4).

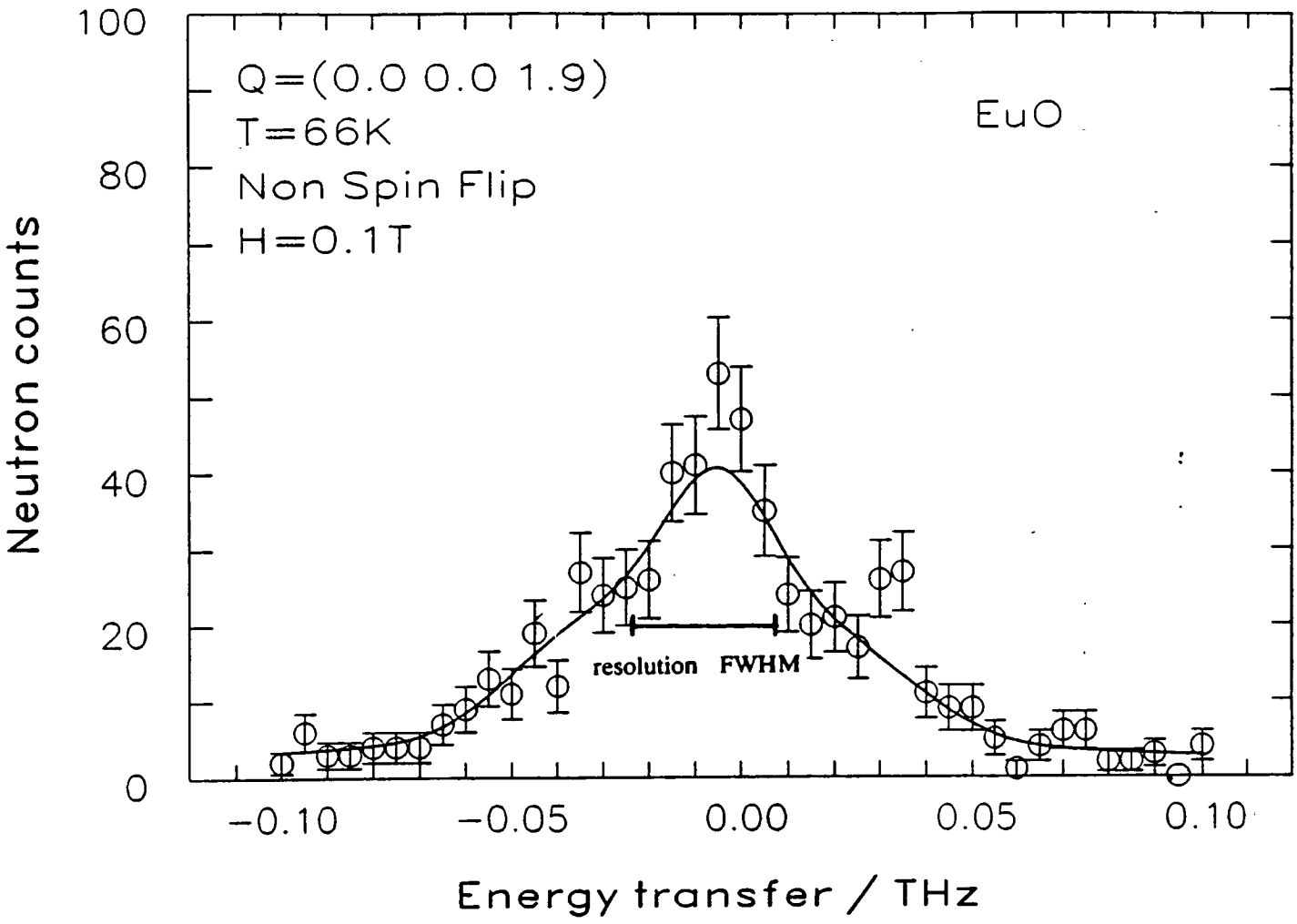

Figure(3.7) depicts representative inelastic spectra using polarisation analysis with a standard triple axis crystal spectrometer. The incoherent elastic scattering is clearly resolved as a discontinuity in the lineshape near $\epsilon = 0.02$ THz. The experimental conditions used are noted by the insert. The solid line represents a smooth interpolation through the best fit to the points, shown with statistical errors, as discussed in Section (3.4).

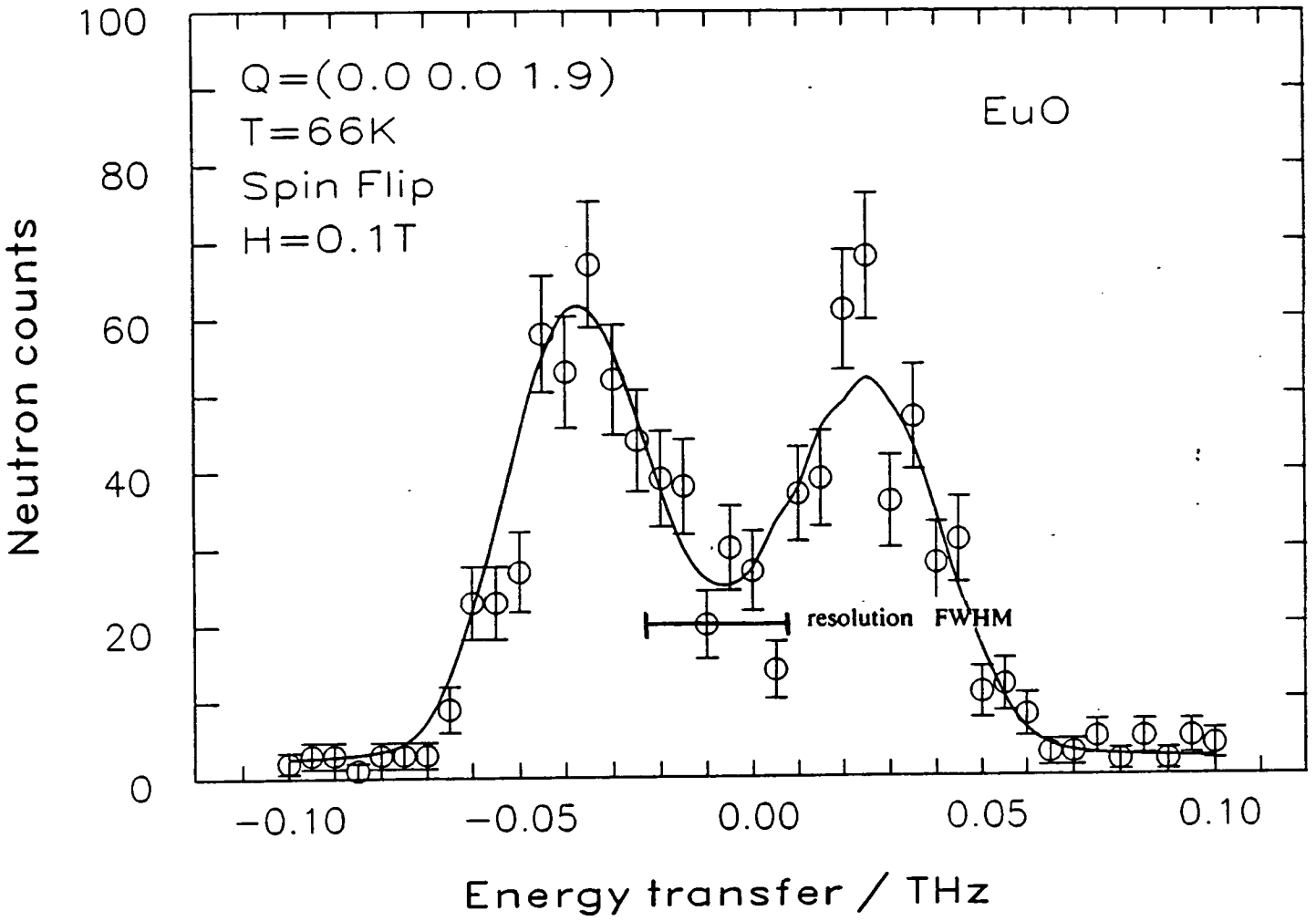

Figure(3.8) depicts representative inelastic magnon spectra obtained using polarisation analysis with a standard triple crystal spectrometer The experimental conditions used are noted by the insert. The solid line represents a smooth interpolation through the best fit to the points, shown with statistical errors, as discussed in Section(3.4).

series of spin flip and non spin flip energy scans were made at constant q = (0 0 2−η) where $0 < \eta < 0.2$. These data were fitted using the Fortran program called Shamgar, described in Section (3.4), to the form for $S(Q,\omega)$ given in equations (3.6) and (3.7), folded with the four dimensional resolution function of the spectrometer, equation (3.4). The functional form for the transverse dynamic structure factor is given by(Lloyd (1989)):

$$S_T(Q,\omega) = A_T[n(\omega)+1]\frac{1}{q^2}\omega_0\frac{\omega\Gamma_T(q)}{(\omega^2-\omega_0^2(q))^2+\Gamma_T^2(q)\omega^2} \qquad (3.6)$$

where $\Gamma_T(q)$ is an intrinsic energy width, A_T an overall scale factor and $\omega_0(q)$ is given by the model lower spin wave branch dispersion relation (Lovesey 1984):

$$\omega_0(q) = Dq^2$$

where q is the reduced wavevector, D is the spin wave stiffness constant for the spin wave branch, and all other symbols have been defined previously. The longitudinal dynamic structure factor is given by:

$$S_L(Q,\omega) = A_L[n(\omega)+1]\left(\frac{1}{q^2+\kappa'^2}+\frac{B}{q}\right)\frac{\omega\Gamma_L(q)}{\omega^2+\Gamma_L^2(q)} \qquad (3.7)$$

where the expression within parentheses represents the analytical form for the static longitudinal susceptibility at small q. The 1/q divergence predicted by Mazenko (1976) at small q is represented by the second term, and in the limit B=0.0 reduces to the mean field result. The parameter $\Gamma_L(q)$ is an intrinsic wavevector width ,$A_L(q)$ and B are overall scale factors, and k is the inverse correlation length of the critical fluctuations. The energy dependence of the longitudinal susceptibility is represented by a Lorentzian. This is the simplest analytical expression that adequately represents the data, and also has a physically reasonable interpretation. The polarising devices on the spectrometer are not perfect, therefore a correction was applied to account for the fraction of neutrons of the wrong spin orientation that reached the detector. The spin flip and non spin flip scans were fitted to the following functional expressions:

$$\left(\frac{R}{1+R}\right)S_L(Q,\omega)+\left(\frac{1}{1+R}\right)S_T(Q,\omega) \qquad (3.8)$$

$$\left(\frac{R}{1+R}\right)S_L(Q,\omega)-\left(\frac{1}{1+R}\right)S_T(Q,\omega) \qquad (3.9)$$

The parameters $\Gamma_T(q)$ and $\Gamma_L(q)$ are also called the transverse and longitudinal damping respectively.

where R is the flipping ratio. Included in the fits were a flat background and a Gaussian centered near $\epsilon = 0$ to account for the incoherent elastic scattering. The parameters describing the background were determined by performing similar scans as described above at $T = 2K$ and subsequent fitting. It was then assumed that this background was independent of temperature. The justification for this approximation is as follows. The initial slope of the phonon dispersion curve is never less than 16.8 meV $\AA^{-1}$. All our measurements were made with considerably smaller energy transfers than required at the given q to excite or absorb a phonon.

Figures (3.9)-(3.11) shows the results of fits to scans with reduced wavevector transfer q=(0 0 2-η) in the range $0 < \eta < 0.2$ at $T = 66K$ to equations (3.8) and (3.9). The solid line represents a smooth interpolation through the best fit to the data points. The fits are shown to be a good representation of the data. Similar scans were performed and analysed for T=63K,67.5K,69K,70K and 71.5K. The quality of the fits was judged by calculating the quantity χ^2 ,see Section (2.5). The value of χ^2 obtained was always close to 1.0 and the value obtained for B equal to zero within statistical error. Care was taken to look for any systematic deviations in the observed from the fitted lineshapes, particularily for energy scans at small q. Figures(3.9) and (3.11) both show evidence of a systematic deviation from the fitted lineshape for energy transfers less than zero. Clearly further measurements should be performed with higher statistical precision. The values for κ, Γ_L and $\frac{\Gamma_T}{D}$ determined by the least squares procedure outlined above are plotted in Figures(3.12) to (3.14) as a function of temperature. The temperature dependence of κ, Figure (3.12), is in qualitative agreement with the predictions of mean field theory and the neutron scattering results of Passel et al (1976). The finite value of κ at T_c is consistent with the presence of a magnetic field at the sample.

The theories of the damping of the longitudinal and transverse fluctuations are at present not well worked out in the $q - \omega$ regime of our experiments. Given

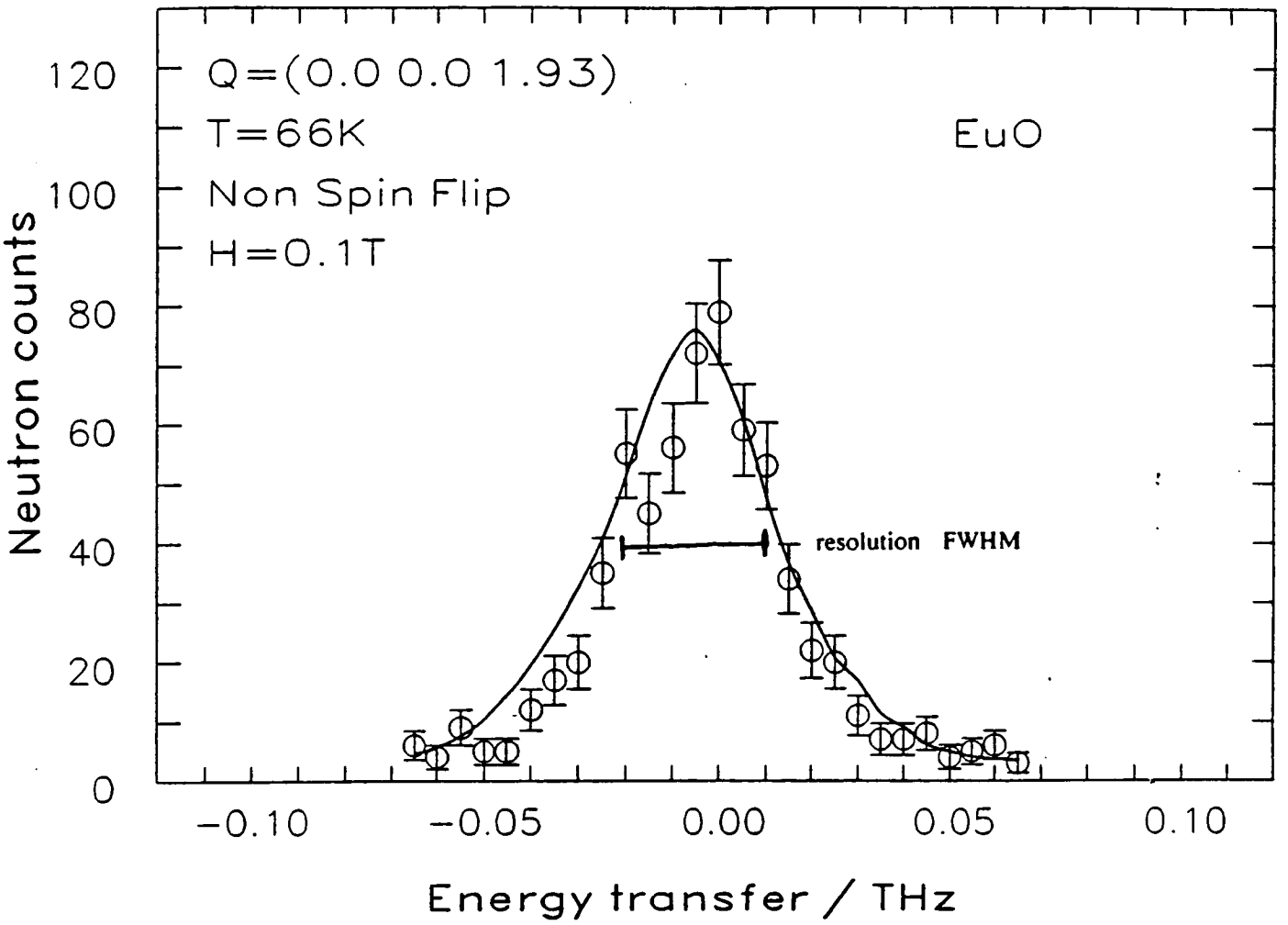

Figure(3.9) depicts representative inelastic spin flip spectra obtained using polarisation analysis with a standard triple crystal spectrometer. The resolution limited elastic incoherent component is clearly resolved at the centre of the energy scan. The solid line represents a smooth interpolation through the best fit to the points, shown with statistical errors, as discussed in Section(3.4).

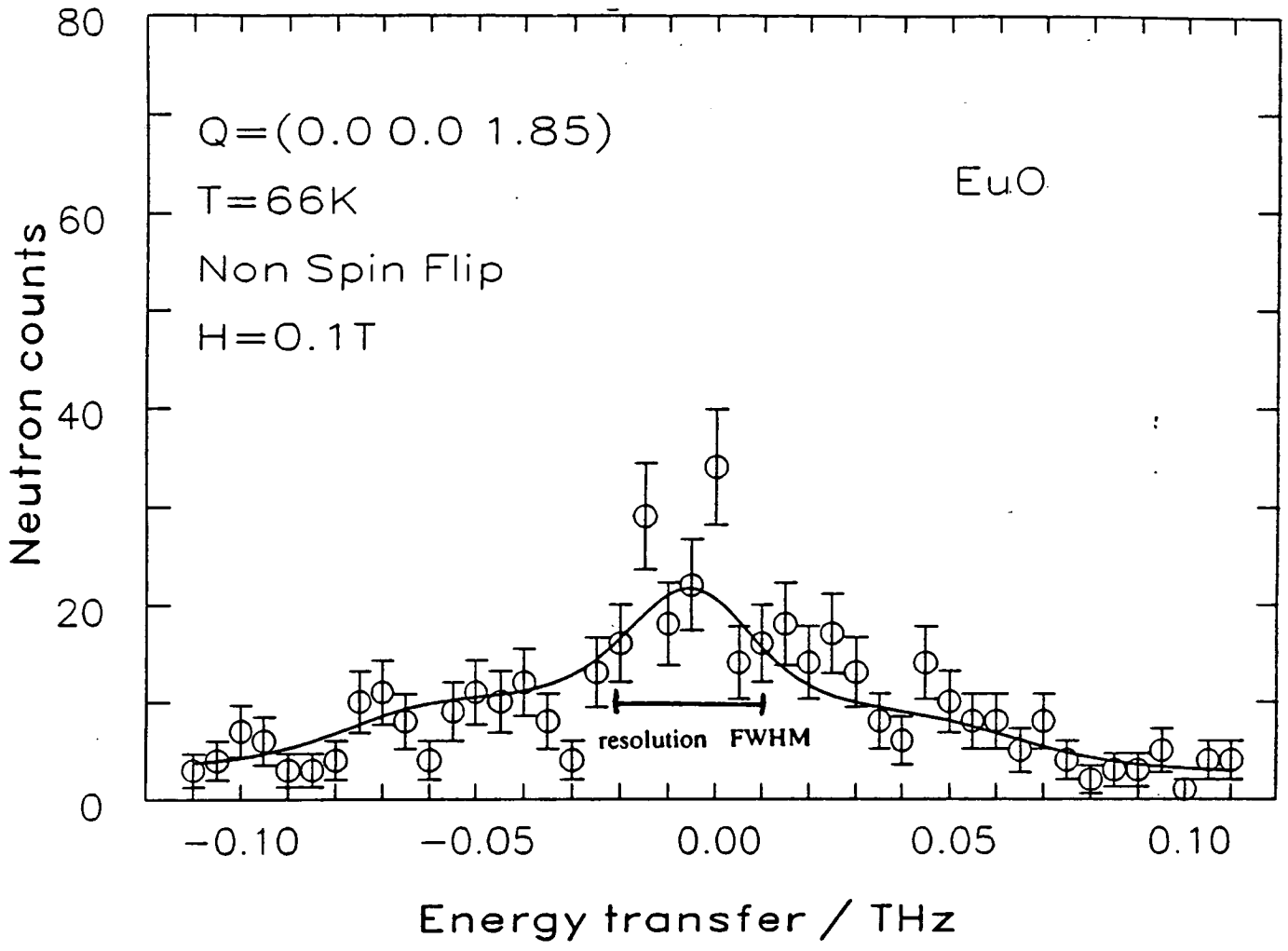

Figure(3.10) depicts representative inelastic spin flip spectra obtained using polarisation analysis with a standard triple axis crystal spectrometer. The resolution limited elastic incoherent component is clearly resolved at the centre of the energy scan. The solid line represents a smooth interpolation through the best fit to the points, shown with statistical errors, as discussed in Section(3.4).

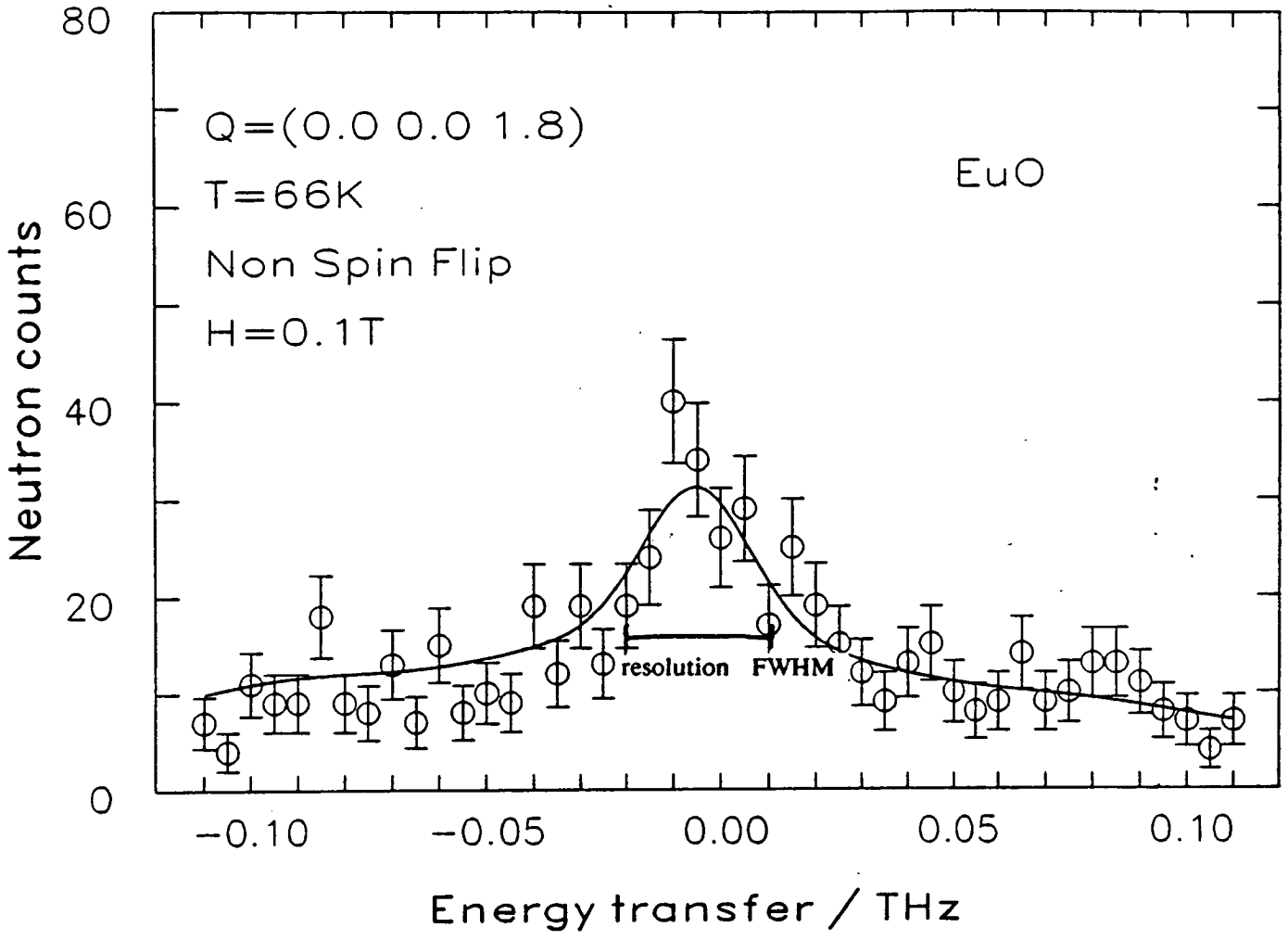

Figure(3.11) depicts representative inelastic spectra obtained using polarisation analysis with a standard triple axis crystal spectrometer. The resolution limited elastic incoherent component is clearly resolved at the centre of the energy scan. The experimental conditions used are noted by the insert. The solid line represents a smooth interpolation through the best fit to the points, shown with statistical errors, as discussed in Section(3.4).

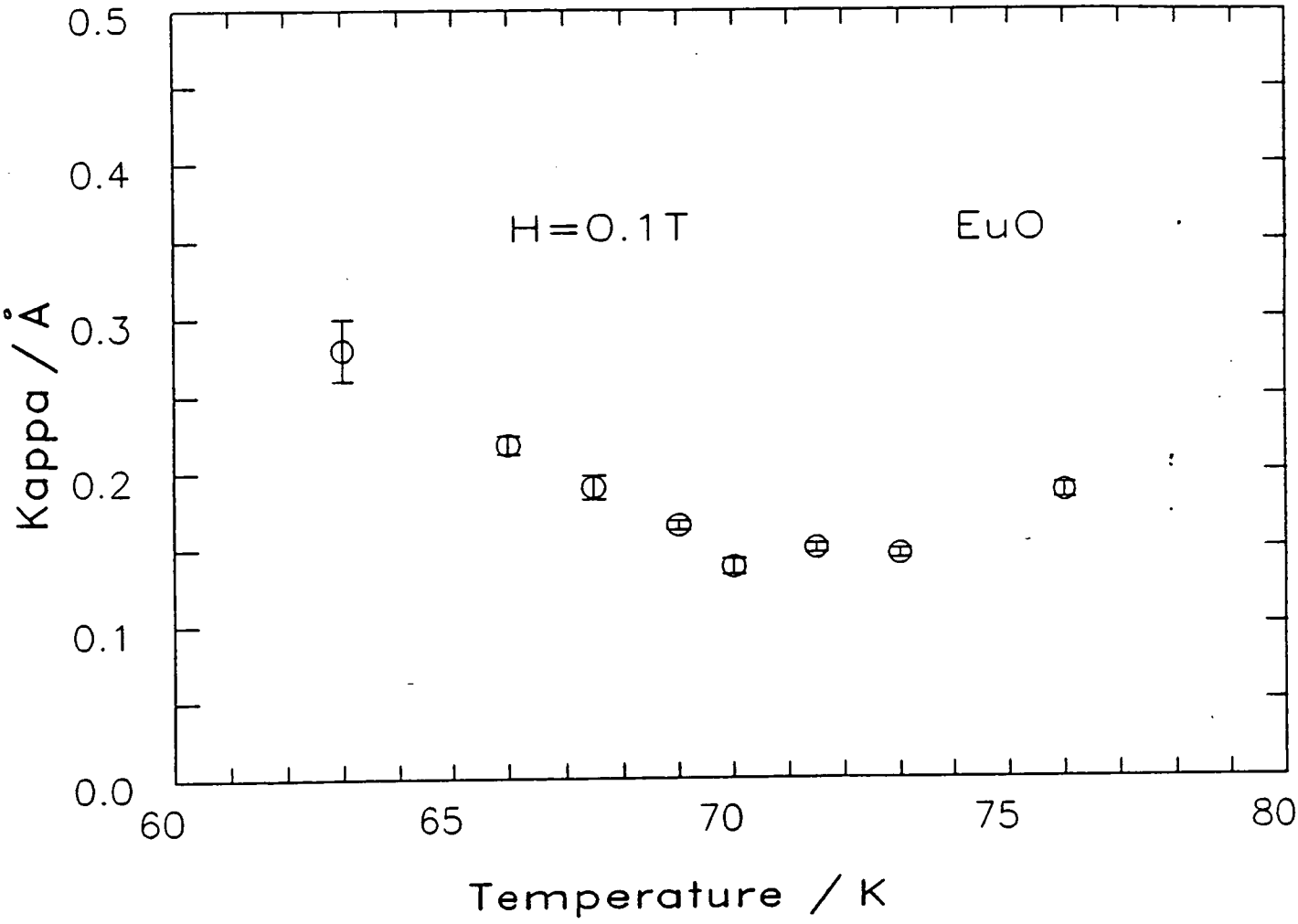

Figure(3.12) shows the values obtained for kappa with errors from the fitting procedure described in Section(3.4) plotted as a function of temperature

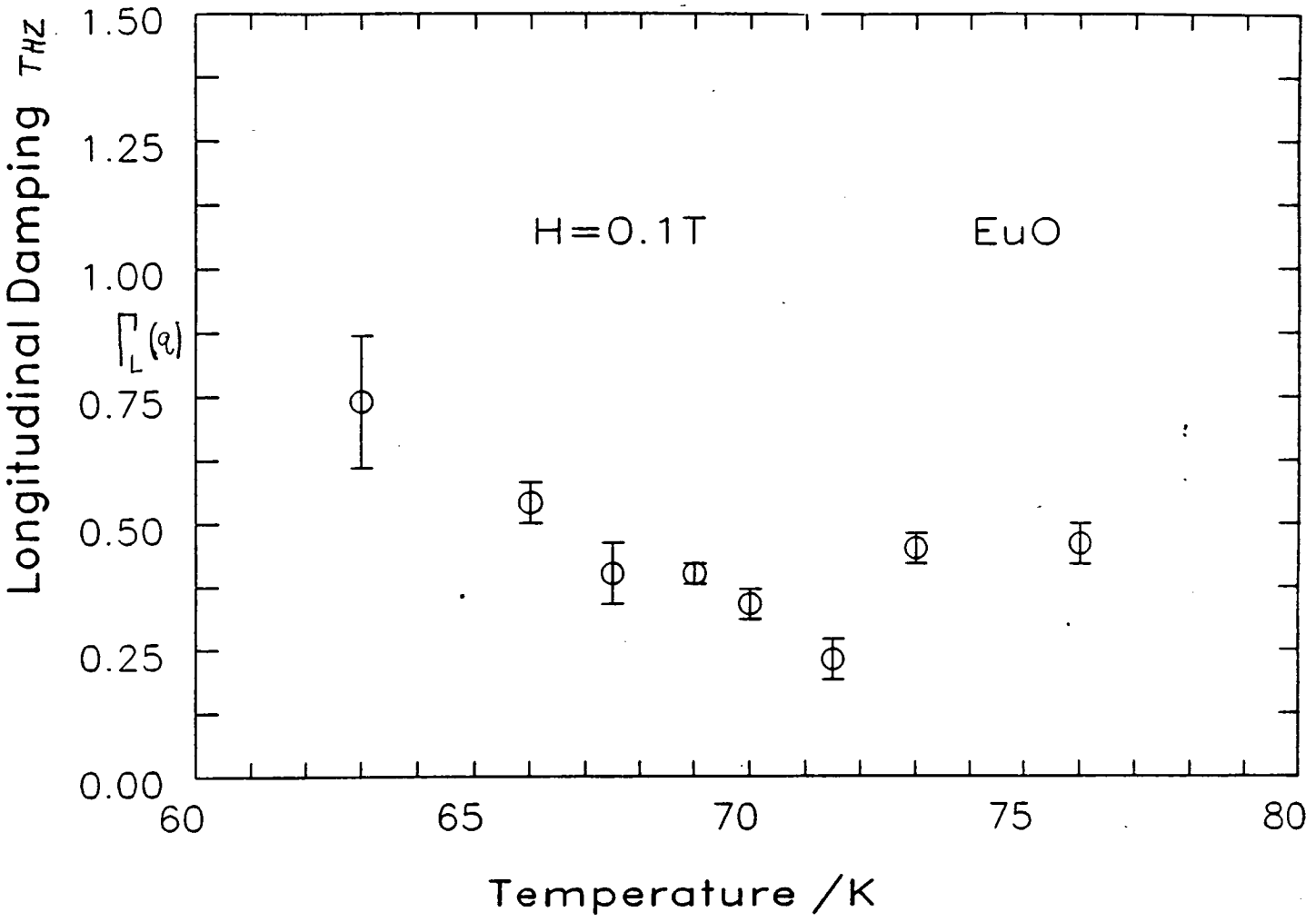

Figure(3.13) shows the values obtained for the longitudinal damping with errors from the fitting procedure described in Section (3.4) plotted as a function of temperature.

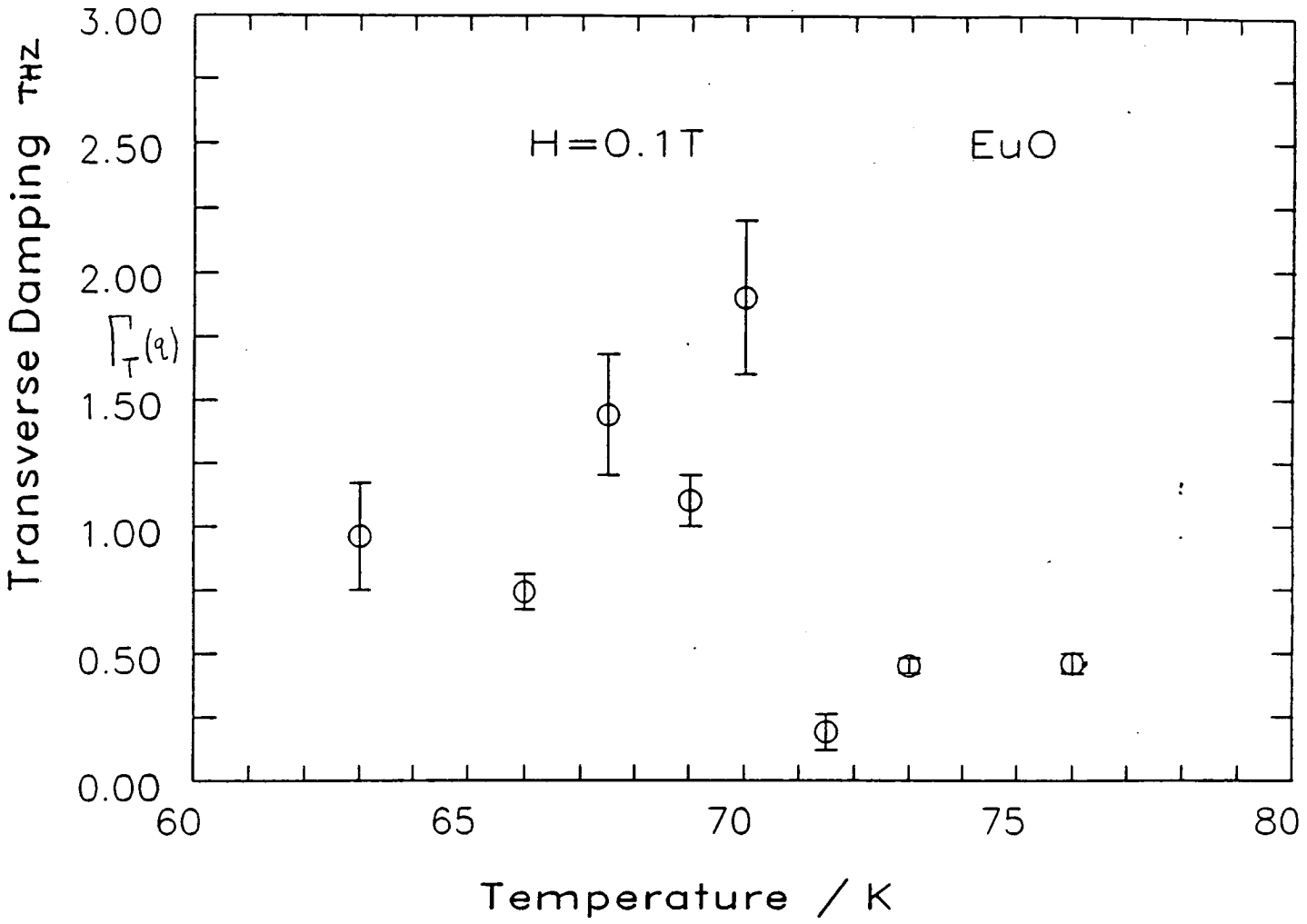

Figure(3.14) shows the values obtained for the transverse damping with errors from the fitting procedure described in Section (3.4) plotted as a function of temperature.

also the limited statistical precision of our data we can only say that the behaviour of the longitudinal damping, Figure (3.13), appears intuitively correct whereas the temperature dependence of the transverse damping, Figure (3.14), is anomalous. We believe however that the assumptions made in fitting the data and the statistical accuracy of the results are such that the trend shown may not be meaningful.

The magnetic field dependence of the longitudinal susceptibility was investigated for an applied magnetic field in the range 0.1T to 2T, with a sample temperature of 66K. When the applied field strength was greater than 1T the nonspin flip component of the scattered neutron distribution was negligible, equations (3.8) and (3.9), and precluded a model fit to the data. The statistical precision of the data collected for a magnetic field strength less than 1T was insufficient to allow the model to be validated quantitatively. However, for an applied magnetic field in the range 0.1T to 0.4T the parameters k and Γ_L remained constant with a value of $0.26+0.02$ $\AA^{-1}$ and $1.6+0.6$ THz respectively. The spin wave stiffness increased with the magnetic field strength: D = $0.758+0.005$, $1.31+0.07$ and $1.5+0.1$ THz, and the magnetic field values were 0.1,0.2 and 0.4T respectively.

3.5.1 Discussion and conclusions

Measurements for the energy dependence of the longitudinal susceptibility at small q show that the response is quasielastic, centered at $\epsilon = 0$, above and below T_c. This is in agreement with the results for $Pd(10\%)Fe$ (Mitchell et al (1984)) and Nickel (Mitchell (1987) unpublished). This form for the response function is consistent with that predicted by hydrodynamic theory (Forster (1975)). Measurements for the wavevector dependence of the longitudinal susceptibility could adequately be described by the mean field model. However this may be a consequence of the lower limit on the wavevector transfer accessible and/or the presence of a finite magnetic field at the sample: the magnetic field introduces a small energy gap at q=0 equal to $g\mu_B H \sum_i s_i^2$. The wavevector dependence of the longitudinal damping was found to be proportional to q^2 and q^4 for the

transverse damping as predicted by hydrodynamic theory. The poor statistical precision of the data for the field dependence of the longitudinal susceptibility precluded a detailed comparison with theory. Consequently the theoretically predicted divergence with decreasing field remains unobserved. A major technical difficulty in performing these measurements arose from the strong coherent nuclear component to the (002) Bragg reflection. It would be advantageous to perform similar measurements near the (111) Bragg reflection where the nuclear coherent contribution is considerably reduced because of destructive interference between the lattice of Eu^{2+} ions and the lattice of O^{2-} ions.

Chapter 4

Lead Magniobate: A system with competing interactions

4.1 Introduction

The discovery in 1945 that barium titanate exhibited a ferroelectric phase provided new impetus to the theoretical and experimental studies of the phenomenon because of its simple crystal structure. The transition to the ferroelectric state, where a spontaneous polarisation P exists, is accompanied by large anomalies in the permittivity which occur over a narrow temperature range,see Figure(4.1). Devonshire (1954) was successful in describing this anomaly and correlating other macroscopic effects using Landau theory, Section (1.2.1), with P as the order parameter. Progress in our understanding of the microscopic origin of the transition followed when Cochran (1960,1961) made the connection between lattice dynamics and ferroelectricity through the Lyddane-Sachs-Teller (1941) relation. This relates the anomaly in the permittivity to the decrease in the frequency of a Brillouin zone centre transverse optic vibrational mode towards zero as we approach the transition temperature. The associated "freezing in" of the atomic displacements determined by the mode eigenvector gives rise to the new low temperature structure. The microscopic origin of the temperature

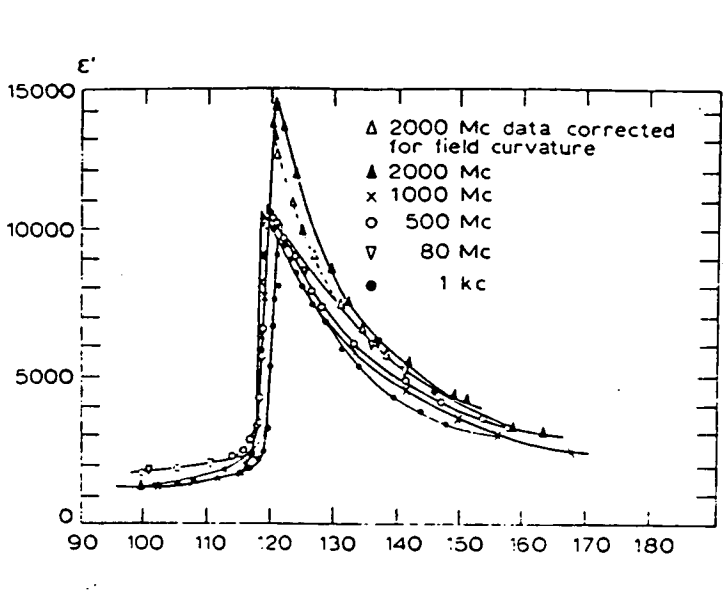

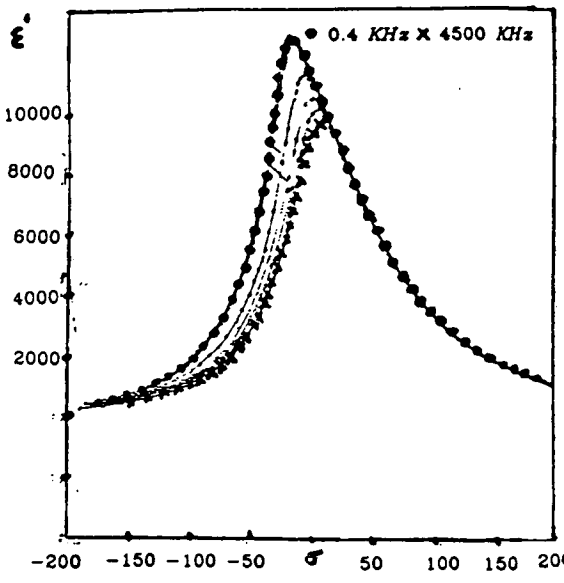

Figure(4.1) Real part of the permittivity ,ϵ, (a) for barium titanate , and (b) lead magniobate, plotted versus temperature for different values of the applied electric field frequency.

dependence of this "soft" mode has been attributed to anharmonic interactions between the normal modes of vibration (Cowley (1963)) and to the anisotropic oxygen ion polarisability by Migoni (1976). Until quite recently these models provided a satisfactory description of the phase transitions in perovskites (Scott (1974)), generic chemical formula ABX_3. However, disordered crystals having the formula $AB'_xB''_{1-x}X_3$ may have phase transitions where the permittivity anomaly is not described by the usual Curie-Weiss law and extends over tens or even hundreds of degrees. The temperature at which the permittivity maximum occurs decreases with the measuring field frequency, Figure(4.1 b), and can be quenched by application of a large electric field. In addition to the absence of a soft mode the anomaly is accompanied by metastability, thermal and permittivity hysteresis effects that are analogous to the behaviour found in magnetic spin systems with competing interactions, Section (1.2.2). Competing interactions in structural systems may arise from the presence of random fields and/or frustration effects.

Random electric dipole fields maybe created because the smaller cation sits in one of several crystallographically equivalent off centre symmetry positions due to the differing ionic radii of the B'' and B' ions and the change in the local interatomic force constants. Frustration to establishing long range order may also occur if the pure crystals $AB'X_3$ and $AB''X_3$ form ferroelectric and antiferroelectric structures respectively. Clearly the random field and spin glass models are limiting cases of what may occur in real systems. At present it is not well understood how closely real structural systems approximate to either the spin glass model (Klein et al(1976), Aharony (1978)) or the random field model (Vugmeister (1984),(1985)). Experimentally the situation is complicated by the difficulty of distinguishing between the low temperature phase of the random field model , ordered regions , and the spin glass model ,randomly oriented dipoles, by bulk permittivity measurements and other techniques that require the application of an electric field.

On cooling through the ferroelectric phase transition the order parameter may lie along any of the equivalent crystallographic directions in different regions of the crystal. The interfaces between these regions, because of the constraints imposed by lattice continuity and charge neutrality, are constrained to a small number of well defined crystallographic directions. Bruce (1981) has shown that these interfaces give rise to lines of diffuse x-ray scattering perpendicular to the interface and that the wavevector and temperature dependence provides detailed information about the interface width and the atomic displacements. In contrast the freezing in of randomly oriented dipoles is expected to give rise to a continuum of diffuse scattering that has only a weak wavevector dependence. Consequently the technique of x-ray diffraction may enable us to distinguish between the low temperature phases possible for systems with competing interactions. We chose to study lead magniobate, $PbMgNb_2O_9$, because it has been widely studied by other techniques and the charge difference between Nb and Mg is sufficiently large that macroscopic inhomogeneity in the mixture is

unlikely because of the large electrical charge imbalance it would lead to. Consequently deviations from the Curie-Weiss law for the permittivity are intrinsic to the physics rather than transition rounding because of concentration gradients.

The arrangement of the chapter is as follows. In Section (4.2) a review of previous experimental work is given. Section (4.3) contains a discussion of the theory for x-ray scattering by atomic fluctuations and domain walls in perovskite structures. In Section (4.4) the experimental details are outlined, and in Section (4.5) measurements of the diffuse x-ray scattering as a function of temperature and electric field in the (001) and $(0\bar{1}1)$ crystallographic plane are reported. Finally in Section (4.6) a discussion of our results and those obtained by other experimental techniques is given and suggestions made for further work.

4.2 Lead magniobate: a review

Lead magniobate has the perovskite structure, generic formula ABX_3, and is shown in Figure (4.2), with lattice parameter a = 4.04 $\mathring{A}$ (Krause et al 1971). A is a monovalent or divalent metal ion, B is a tetra or pentavalent ion and X may be oxygen or fluorine. The distribution of magnesium and niobium ions on the crystallographic B site can be ordered in principle (Glasso (1969)) according to two adjacent (111) planes being composed of Nb ions followed by one (111) plane containing Mg ions. The observation of strongly broadened first order Raman lines (Smolensky et al(1976), Burns and Scott (1973)), forbidden by symmetry for an ideal cubic perovskite structure, and three Restrahlung bands, corresponding to 3 degenerate infra-red active vibrational modes, (Karamyan and Krainik (1973), Burns and Dacol (1983)) suggest the material is disordered on a macroscopic scale.

Electron diffraction (Krause et al(1971), Krause et al (1979)) measurements

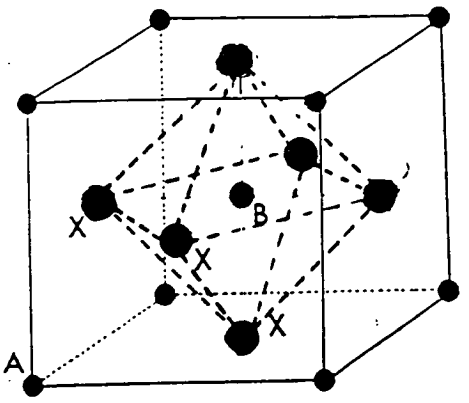

Figure 4.2 Ideal cubic perovskite structure showing the positions of atoms A.B and X. The number of off-symmetry positions for the impurity atom B" is determined by the displacement direction and the cubic point group symmetry.

at room temperature indicate the existence of microscopic regions of ordering, about 20 - 50 $\mathring{A}$ in extent, that may give rise to frustration effects because of the tendency of ordered and disordered lead perovskites to form antiferroelectric and ferroelectric structures respectively. The different ionic radii of magnesium and niobium, 0.72$\mathring{A}$and 0.64 $\mathring{A}$ respectively (Shannon (1976)), may also give rise to small electric dipoles which are randomly distributed throughout the crystal volume.

The transition to the low temperature phase is characterised by a cusp in the permittivity (Schmidt et al (1981), Smolensky (1984)), that extends over several hundred degrees ,a maxima at -8^0C, and is not described by a Curie-Wiess law. The electric field dependence of the permittivity suggests the transition is second order (Bonner et al (1967)). The permittivity magnitude depends on the amplitude and frequency of the applied electric field (Smolensky (1970)). A field of 26KV/cm suppresses the dielectric anomaly (Bonner et al (1967)) completely. Strong relaxation, hysteretic effects and anomalies in the specific heat at very low temperatures (Lawless (1976),(1977)) are also observed.

Raman scattering measurements (Karamyan and Krainik (1973)) have failed to detect a soft zone center transverse optic mode with a frequency greater than 5 cm^{-1}. The elastic moduli provide information about the transition because of the electrostrictive coupling in cubic materials between strain and the polarisation due to the soft mode phonon, (Thomas and Slowezewski (1970)). Broad minima (Wu and Sladek (1982)) in the shear and longitudinal elastic moduli between 210K and 298K, were determined from ultrasonic measurements using a ceramic sample. Similar minima in the shear moduli were observed for single cystal samples (Smolensky and Yuskin (1985)) along with a maximum in the attention of the acoustic wave near the transition region. Smolensky et al (1976) have observed a similar softening of the elastic moduli using the technique of Brillouin scattering. The hydrostatic pressure dependence (Matheswaranthan and Sladek (1987)) of the elastic moduli determined by ultrasound suggests that the observed elastic anomaly is not due to a softening transverse zone centre optic mode.

The integrated scattering of light (Smolensky et al(1976)) decreases with rising temperature until it vanishes at 360^0C. The light scattering is attributed by the authors to the existence of small polar regions, around 10^{-7}m in extent that are independent of temperature (Krainik and Trepakov (1982)). The scattering intensity is strongly suppressed by the application of an electric field of $6KV/cm$. Further evidence for the existence of polarised regions above T_c is provided by measurements of the refractive index. The change in the refractive index is related to P^2 for cubic crystals (Nye (1957)). Burns and Scott (1973) have shown that deviations from the high temperature paraelectric behaviour expected for the refractive index begin at a temperature, T_d , around 360^0C and similar measurements (Korshunov et al (1983)) made with higher resolution suggest that T_d is close to 600^0C.

The permittivity has been determined for single crystals (Nadolniskaya et al (1987)) in the frequency range $0.1 - 10^4Hz$ and temperatures from 83 to 650K.

The results suggested the presence of three relaxation mechanisms that were attributed to thermally activated domain wall motion and subsequently supported by measurements made with an electric field applied (Nadolnisaya et al (1988)).

Single crystal x-ray diffraction (Salnikov et al (1971)) measurements and Raman scattering (Karamyan and Krainik (1973)) investigations suggest the low temperature phase is tetragonal. The extinction positions observed after examination of the sample in an electric field by polarised light are also consistent with a tetragonal structure (Bokov and Mylnokova (1961)).

A peak in the permittivity anomaly is observed at a temperature of -8°C. The anomaly is not consistent with a ferroelectric phase transition and has several properties that are characteristic of systems with a spin glass transition. In the absence of an applied electric field lead magniobate is isotropic below the permittivity anomaly. At present this has been attributed to the existence of either a random dipolar glass (Burns (1986)) or many small ferroelectric domains. The objective of this study was to distinguish between these two possibilities by using the technique of x-ray diffraction.

4.3 X-ray scattering

In the following section the result for the dynamic structure factor in the one phonon approximation is given by (Bruce and Cowley (1981))

$$S^1(Q) = \frac{\hbar}{\pi} \sum_{qjj'} \delta(Q+q) F_1(Q,qj) F_1(-Q,-qj)(n(qj)+1)\chi''(qjj') \qquad (4.1)$$

where

$$F_1(Q,qj) = \sum_{\kappa} f_\kappa(Q) M_\kappa^{\frac{-1}{2}} (Q.\xi(Q,qj)_\kappa) e^{i(Q-q).R(\kappa)-W_\kappa(Q)} \qquad (4.2)$$

and $f_\kappa(Q)$ is the atomic form factor for atom κ in the unit cell. $Q = \tau + q$, where τ is a reciprocal lattice vector of the high temperature structure. $\chi''(qj)$ is the imaginary part of the dielectric susceptibility, and the conditions under which

this quantity is directly related to $S^1(Q)$ are discussed in detail by Cochran (1969). All other symbols are as defined in Section (2.2). It may be readily shown that if the behaviour of a mode is represented by a harmonic oscillator then $\chi''(qjj')$ is given by (Bruce and Cowley 1981):

$$\chi''(qjj') = \frac{\hbar}{\omega(qj)}(2n(qj)+1)\delta_{jj'} \tag{4.3}$$

From equation (4.3) it is expected that the phonon branches with the lowest frequencies contribute most strongly to the scattering intensity. To obtain the explicit wavevector dependence of the one phonon scattering intensity the acoustic phonon dispersion relations are approximated by a single isotropic branch given by the relation , $\omega = vq$, where v is the phonon propagation velocity and ω the phonon frequency. Apart from constant prefactors the results for the one phonon structure factor in the high temperature limit, $kT >> \hbar\omega$, is given by:

$$S^1(Q) = \frac{k_B T}{v^2 q^2} \mid F_1(Q,qj) \mid^2 \tag{4.4}$$

and similarily at low temperatures, $\hbar\omega >> k_B T$,

$$S^1(Q) = \frac{1}{vq} \mid F_1(Q,qj) \mid^2 \tag{4.5}$$

The structure factor, equations (4.4) or (4.5), is largest at Bragg reflection and ,at small q where the wavevector dependence of $|F_1(Q,qj)|^2$ may be neglected, has a simple power law dependence. In general v depends on the crystallographic direction, and as a result the scattered x-ray distribution may be an anisotropic function of the wavevector transfer. The elastic moduli are proportional to v^2 and may be determined by ultrasonic or Brillouin scattering experiments.

Near a structural transition temperature the decrease in the frequency of a soft optic phonon mode and adjacent modes will also give rise to intense diffuse

scattering around the Bragg peaks that may be a highly anisotropic function of the wavevector transfer (Gesi (1975)). Assuming that the amplitude of vibration of the soft phonon mode is the order parameter the temperature dependence of $\chi''(qjj')$ follows readily from equation (1.8).

4.3.1 Domain wall scattering

In this section a simple model of a static ferroelectric domain wall is introduced for materials having a tetragonal perovskite structure. The theory of x-ray scattering by ferroelectric domain walls (Bruce (1981)) has been discussed for domain walls separating regions where the polarisation directions are oriented at 180°, Figure (4.3 a) line B-B'. The results relevant to the work presented in Section (4.5) are presented, and the analysis extended to the case of a domain wall that separates regions where the interfacial polarisation angle is 90° to one another, line A-A' Figure (4.3 a). This model represents the domain configuration which is believed to occur in the low temperature phase of lead magniobate.

If a unit cell in domain j scatters the incident x-ray beam with an amplitude $D_j(Q)$ the structure factor, $A^0(Q)$, for the domain wall is given by:

$$A^0(Q) = \sum_j \sum_R D_j(Q) e^{i(Q.R)} \tag{4.6}$$

where the sum over j represents a sum over the two domains, and the sum over R runs over the unit cells in the j^{th} domain. Figure (4.3 a) shows schematically a domain wall in the crystallographic (100) plane, where the interfacial polarisation angle is 180°, and the crystal lattice is tetragonal. The domain wall is assumed to be flat and perpendicular to the [100] direction with a lattice cell dimension equal to a. The result for the intensity of the scattering by the domain wall in the (001) plane is then given (Bruce (1981)) by:

$$I(Q) = 4 \mid F_2(Q) \mid^2 \frac{1}{(q_x a)^2} \tag{4.7}$$

where q_x is the component of q parallel to the [100] crystallographic direction and a is the lattice cell dimension.

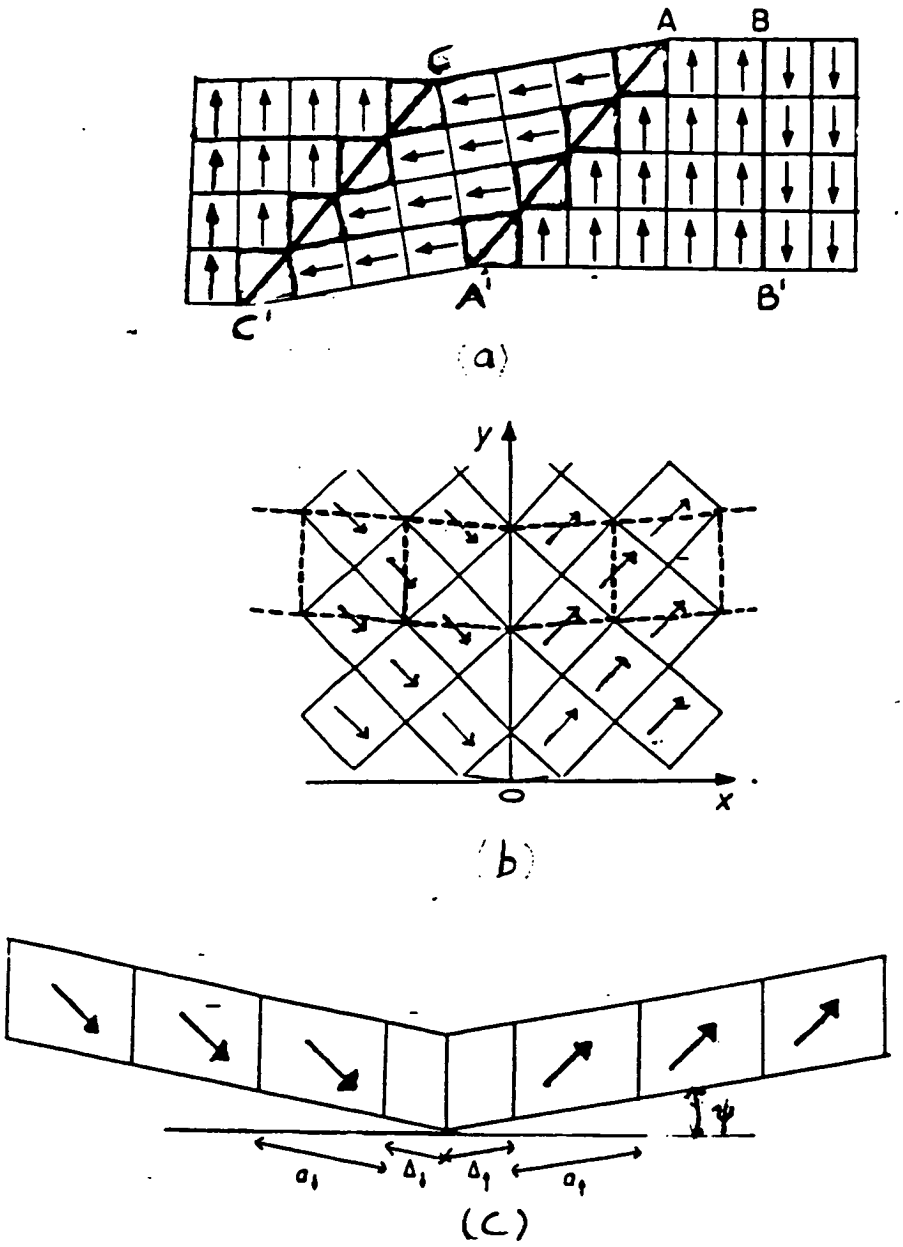

Figure(4.3). (a) Domain wall orientations possible for a tetragonal unit cell, solid line. The tetragonality is exaggerated. (b) The relationship between the mononclinic unit cell, dashed line, and the tetragonal unit cell. (c) The figure illustrates the relationship between the model for the domain wall and the symbols described in the text.

where

$$F_2(Q) = i\sum_{\kappa}(Q.u_{\kappa}^{j})f_{\kappa}(Q)e^{(QR_{\kappa}^{0})} \tag{4.8}$$

where R_{κ}^{0} is the equilibrium cubic phase atomic position and u_{κ}^{j} the atomic displacement from it. The other symbols have been defined in section (4.2). We expect then to observe lines of diffuse scattering along the [100] crystallographic direction denoted here q_x. Similarily it can be shown that a domain wall in the (010) plane gives rise to lines of scattering along the [010] direction .

The domain walls will not be perfectly flat but may fluctuate about an average position because of entropy effects and pinning due to defects. Assuming that the domain wall centre fluctuates about a mean position with a Gaussian probability distribution the result for the amplitude $A(Q)$ of the scattering by the domain wall (Bruce (1981)) is obtained:

$$< A(Q) >= e^{-\frac{1}{2}(aQ_x\lambda)^2}A_w^0(Q) \tag{4.9}$$

where λ determines the probability distribution and is a measure of the wall width and Q_x is the component of Q perpendicular to the wall. The effect of the wall roughness is to decrease the scattering intensity at higher order Bragg reflections and modify the wavevector dependence.

The analysis (Bruce 1981) is now extended to include the case where the polarisation is oriented at 45^0 to the domain wall. A schematic diagram of this situation is shown in Figure (4.3 b). The high temperature phase is referred to a set of axis that correspond to the [110] and [0$\bar{1}$0] direction of the cubic unit cell. The atomic positions in the low temperature phase may then be written as a small and continuous displacement from their high temperature equilibrium positions. The angle between the polarisation direction for domains adjacent to the domain wall is not exactly 90^0 but differs because of the tetragonality of the unit cell. The walls then contain kite shaped cells as shown in Figure(4.3b)that are strained. We have incorporated this effect by including a term Δ, for the lattice periodicity of the cells adjacent to the domain wall, Figure (4.3 c).

In order that we may write $D_j = D^o + iD^j$, (Bruce (1981), equation 8 : note the change of notation), the atomic displacements are resolved parallel and perpendicular to the domain wall and the latter component subsumed into the D^o term. In anticipation of the experimental results $\cos\Psi$ and $\sin\Psi$ are approximated by 1 and Ψ respectively. Following the analysis of Bruce (1981) the result for I(Q) in the (001) plane is obtained:

$$I(Q) = 4\frac{|F_3(Q)|^2}{a^2 q_x^2} \tag{4.10}$$

where

$$F_3(Q) = \left(\sum_\kappa f_\kappa(Q) e^{iQR_\kappa^0}\left(u_k\left(\tau + \frac{q}{\sqrt{2}}\right)cos(Q.\Delta) - sin(Q.\Delta)\right)\right)^2 \tag{4.11}$$

In order to understand qualitatively the distribution of x-ray scattering in reciprocal space it is assumed that $\Delta = 0.0$, and $u.(\tau+q)$ is approximately $(Q.u_k)$. In the (001) plane the wavevector transfer may be resolved as $Q_x = h+q$ and $Q_y = k+q$, where h and k are the cubic miller indices, and $Q = (Q_x, Q_y, 0)$ r.l.u. The structure factors $,(Q.u)$, for wavevector scans along the [110] and [1$\bar{1}$0] directions are $[h-k]^2$ and $[h-k+2q]^2$ respectively, for h and k positive. This gives rise to an asymmetry in the scattering intensity around each Bragg reflection; the sense of the asymmetry is reversed when k is negative.

4.3.2 Summary

Diffuse x-ray scattering is due to fluctuations in the electron density from the translationally invariant part. These fluctuations may be static, domain walls, or dynamic such as phonons. It is impossible to distinguish between static and dynamic effects with x-ray scattering, however the wavevector and temperature dependence of the scattering intensity may favour a particular interpretation.

Fluorescence and Compton scattering also give rise to a diffuse background of scattered radiation.

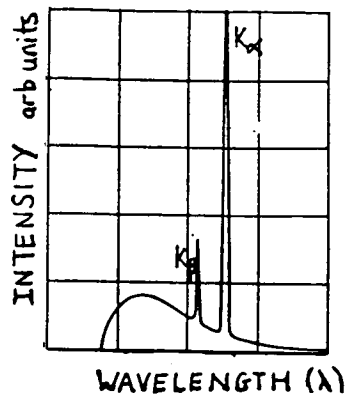

Figure(4.4) The ratio of $K_{\alpha_1}, K_{\alpha_2}, K_\beta$ and the continuum under normal operating conditions is $1 : \frac{1}{2} : \frac{1}{6} : \frac{1}{100}$. The intensity scale is distorted and the fine structure in K_α and K_β is not resolved.

4.4 Triple crystal x-ray spectrometer

The general layout and principles of the triple crystal x-ray diffractometer are the same as the triple crystal neutron spectrometer reviewed in Section (3.4). In the following section the modifications introduced because of the different spectral characteristics of an x-ray and neutron source are discussed.

The spectral output of a Cu target excited by 30KV electrons is shown in Figure (4.4). It is composed , to a first approximation, of a number of characteristic lines superimposed upon the Bremstrahlung continuum. The Bremstrahlung radiation results from the decceleration of the incident electrons through electromagnetic interaction with the target material. The cutoff of this continuum is determined by the incident energy of the electrons and is controlled by the accelerating potential across the x-ray tube. The characteristic x-ray lines are due to radiative transitions between atomic electron energy levels as a result of collisions with the impinging electrons. The lower electronic energy levels are denoted by the letters K, L and M. Transitions between the K-L, and K-M shells are known respectively as K_α and K_β radiation. Because the electrons in the L and M shell are not all degenerate in energy the K_α radiation is really a doublet and the K_β line has even more structure.

The choice of wavelength for a diffraction experiment is limited by the suitability of a material as a target and the technique. Consequently copper because of its good heat conduction properties and the matching of the K_α radiation wavelength to lattice parameters is preferred for general crystallographic purposes unless there is a particular reason to the contrary. One such reason is the existence of an x-ray absorption edge, for one of the constituent elements of the specimen under study, at a slightly larger wavelength than the incident radiation. The emitted fluorescence can give rise to an intense background and another radiation maybe preferred such as Ag, Mo, C or Fe.

The x-ray source for the Edinburgh triple crystal spectrometer is a rotating copper anode with line focal spot. The intrinsic limit to the intensity of the radiation emitted per unit area from the focal spot of an x-ray tube is set by the rate of heat conduction through the material. By rotating the anode and employing a line focal spot, viewed at a small angle α, Figure (4.5 a), a large increase in intensity is obtained when compared to that from a conventional x-ray tube.

The schematic outline of the spectrometer is shown in Figure (4.5 b). Unlike the neutron spectrometer case the monochromator setting angle θ_m and the analyser setting angle θ_a remain fixed throughout the measurements. The mosiac spread $\Delta\theta$ for the crystals used varied from a few thousands of a degree for Bragg reflection from (111) planes of silicon to tenths of a degree for Bragg reflection from the (002) planes of graphite. Consequently the wavelength composition of the reflected beam differs in each case. Graphite removes the K_β component of the incident radiation and, apart from the higher harmonics of the K_α line, the Bremstrahlung. However, even by inserting a narrow slit to control the incident beam divergence and give an effective mosaic spread smaller than the physical one it is not possible to remove the K_{α_2} component.

Silicon is a cubic crystal having the diamond structure and therefore has an

The reflected wavelength is determined by Bragg's law, $2d\sin\theta=n\lambda$, where d is the crystal interplanar spacing of the monochromator, and θ the angle in the scattering plane between this plane and the incident beam. At a fixed angle of incidence and interplanar spacing, the range of wavelengths that satisfy the Bragg condition is determined by the angular spread of the incident beam and mosaic spread of the monochromator. Under the present experimental conditions the beam is sufficiently well collimated, and the mosaic spread, $\Delta\theta$, of the monochromator small enough that the condition for a Bragg reflection is satisfied only for the K_{α_1} component, and integral multiples of this wavelength, of the incident beam.

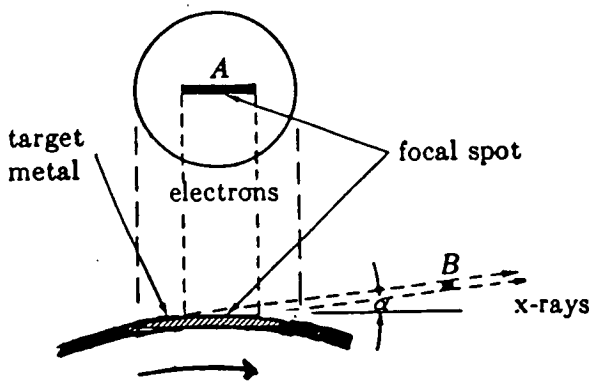

(a)

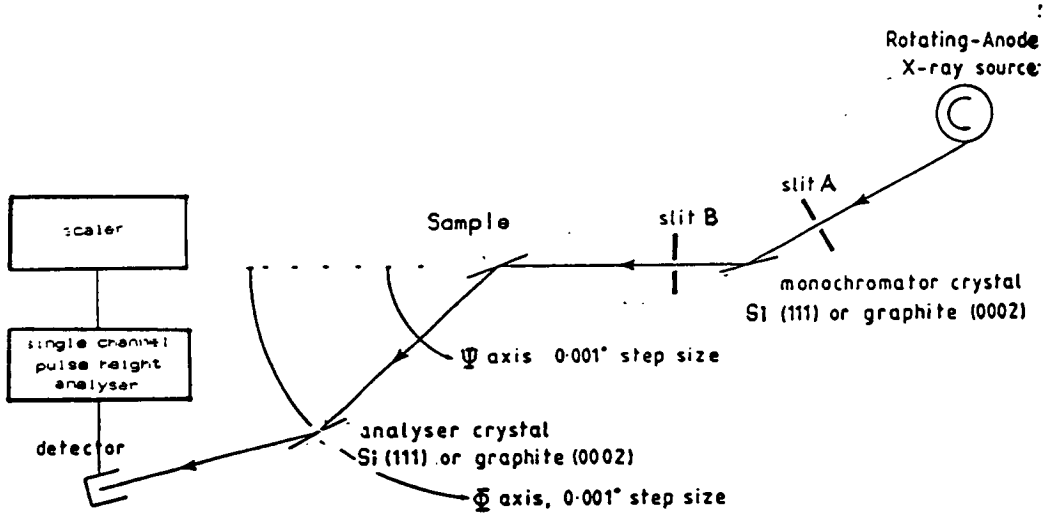

(b)

Figure(4.5). (a) Schematic diagram of the anode head. (b) Schematic diagram of an x-ray spectrometer reproduced from Lucas (1988).

accidental absence for the (222) Bragg reflection. Consequently the reflected beam is almost free from contamination by the first higher order harmonic. For perfect crystals the relationship between wavelength and direction in real space introduced by Bragg reflection may be taken advantage of to remove the K_{α_2} component by insertion of a narrow slit after the monochromator. The wavelength spread of the incident beam is then determined by the K_{α_1} linewidth and this configuration is used for very high resolution diffraction studies.

The rotation axes of the sample crystal, Ψ, and analyser/detector system , Φ, are coaxial, see Figure(4.5 b), and their positioning is controlled by a PDP/11 microcomputer. This allows intensity measurements to be made and recorded automatically along preselected directions in the diffraction plane with step sizes down to 0.001^0.

The detector was a $Xe(CH_4)$ proportional counter with an active area larger than the transmitted beam area. The proportional counter is a gas filled cylindrical chamber with a central wire (anode) held at a positive potential $\sim$600V. As the x-ray beam passes through the chamber electrical pulses, due to primary and secondary ionisation processes, are produced, the amplitude and number of which are proportional to the incident beam energy and intensity respectively. This signal is then fed, to an electrical circuit known as a pulse height discriminator which passes only pulses within a narrow preselected amplitude (voltage) range to an amplifier. After amplification the counts are recorded over a preset time interval by a meter. The bandwidth of the discriminator is a compromise between energy resolution and allowance for the variation in pulse height due to the statistical nature of the arrival times of the photons and the finite recovery time of the detector. The FWHM of the detector resolution is 1.3 KeV for x-rays having an energy of 8 KeV. This is more than adequate to discriminate against the higher harmonics of the incident radiation, having energies of 16KeV and 24KeV respectively, when using graphite for the monochromator and analyser crystals.

4.4.1 Resolution function of an x-ray spectrometer

The quantitative analysis of x-ray scattering data collected using a triple crystal x-ray spectrometer requires a detailed knowledge of the instrumental resolution and is analogous to the situation described in Section (3.4) for data collected with a neutron spectrometer. The x-ray scattering data presented later in this chapter are preliminary measurements and have been treated qualitatively. Consequently only the features of instrumental resolution salient to the experiments are reviewed here.

The inapplicability of the Gaussian approximation (Cowley 1986) for several resolution components of a triple crystal x-ray diffractometer may result in qualitative as well as quantitative differences in the shape of the resolution function in reciprocal space, when compared to the neutron spectrometer case. Specifically, the use of perfect crystals as monochromator and analyser, means that dynamical diffraction theory must be used to describe the diffraction of the incident radiation and the result of this theory is the existence of $\frac{1}{\theta^2}$ tails in the reflectivity or Darwin curve, where θ is the angular deviation from the nominal ray at the Bragg angle. Consequently the Darwin curve describing the monochromator and analyser crystals gives rise to deviations in the direction to the incident beam and consequently to a streak of intensity from each crystal around the observed Bragg reflections. The theoretical derivation for the location of the streaks in reciprocal space from each of the resolution elements, monochromator and analyser crystals and wavelength spread, $\Delta\lambda$, has been discussed lucidly previously (Lucas (1988)). Therefore only the relevant results are presented and these are shown schematically in Figure (4.6).

Cowley (1986) has approximated the Darwin width of the Bragg reflection by a Gaussian having the appropriate width. The resolution function calculated within the Cooper-Nathans formalism, assuming the sample contribution to be negligi-

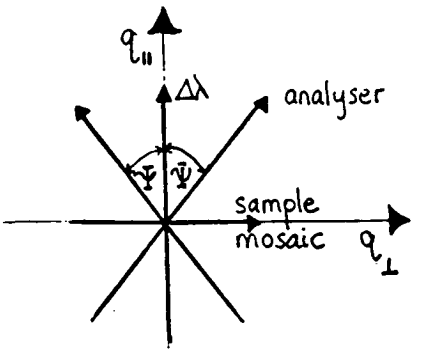

Figure (4.6) The resolution function obtained for silicon monochromator and analyser crystals. Streaks from each of the resolution components decided by arrows are shown. $q_{\parallel}$ and $q_{\perp}$ are components of q resolved parallel and perpendicular to Q.

ble, is in good agreement with the experimental iso-contours until the intensity is less than 5% of the maximum. The principle finding of the work is the complicated variation of the resolution function FWHM parallel and perpendicular to the wavevector transfer. Cowley has suggested that the quantitative measurement of x-ray scattering intensity in the form of rods should be measured by making wavevector scans perpendicular to the rods. Apart from polarisation and absorption factors the resolution function is then independent of Ψ and the integrated intensity is then proportional to the scattering power of the rod. This result is important for the correct interpretation of the diffuse scattering by domain walls.

Polarisation, R_p, and absorption, R_a, corrections to the data for the extended face geometry assuming the sample intersects all the beam are given below (Luger 1980)

$$R_p = \left(1 + \frac{1}{2} cos^2 2\theta_m cos^2 \Psi cos^2 2\theta_A\right) \qquad (4.12)$$

$$R_a = \frac{sin(\Phi - \Psi)}{sin\Psi + sin(\Phi - \Psi)} \tag{4.13}$$

All symbols are defined in Figure(4.5 b).

4.4.2 Experimental arrangement

The x-ray source was operated at 3KW with a copper target. CuK_α x-rays ($\alpha_1 = 1.54051\mathring{A}, \alpha_2 = 1.54451\mathring{A}$ (Bragg (1947)) were used and the focal spot of the rotating anode tube was a vertical line of height 3mm and width 0.3mm, viewed at a take-off angle of 6^0.

Measurements of the diffuse x-ray scattering were performed using pyrolytic graphite monochromator and analyser crystals, because the diffuse scattering was expected to be extremely weak. The instrumental FWHM parallel and perpendicular to the wavevector transfer was $0.008\mathring{A}^{-1}$ and $0.002\mathring{A}^{-1}$ respectively at the (300) Bragg reflection. A vertical slit placed between the monochromator and sample crystal limited the vertical divergence of the beam and produced a resolution perpendicular to the scattering plane of $0.1\mathring{A}^{-1}$.

The samples were single crystal (001) plates of size 3 x 4.7 x $2.2mm^3$ and 4 x 1.7 x $1mm^3$. They were cut from a boule supplied by G. Burns of IBM and are denoted in the results section as sample 1 and sample 2 respectively. The quality was assessed after mechanical polishing by examination in unpolarised light with an optical microscope and by measurement of the Bragg reflection rocking curve with the diffractometer in the high resolution configuration. The samples were found to be free of inclusions and sample 1 to have a rocking curve width of 0.018^0.

The sample was oriented in an extended face geometry on the diffractometer with either a [001] or [$0\bar{1}1$] axis vertical and perpendicular to the scattering plane. By alternately mounting the crystal in a variable temperature furnace or closed

cycle helium refrigerator the temperature could be varied from 620K to 12K. The absolute temperature was accurate to ± 2K at the maximum temperature attainable and to better than ±0.5K for $273K < T < 483K$, while the temperature stability was controlled to within $\pm 0.25K$. At the lowest temperature of 12K the stability was ±0.1K and better than ±0.5K for $12K < T < 273K$, while the absolute temperature was accurate to ±0.5K. An electric field could be applied via silver plate electrodes to the (100) face. For these measurements the sample was attached to a ceramic plate that was in turn mounted on the cold finger of the cryostat.

High resolution diffraction measurements using a silicon monochromator and analyser crystal were made with the sample oriented with a [001] axis vertical. The generator operated at 0.4KW and the CuK_{α_2} component in the incident radiation was cut off by the knife edge of the divergence slit B, Figure(4.5 b); set at a distance of 200mm from the monochromator. This arrangement gave a resolution parallel and perpendicular to the scattering vector of $0.002\AA^{-1}$ and $0.0016\AA^{-1}$ respectively at the (400) Bragg peak.

4.5 Results

4.5.1 Diffuse scattering in the (001) plane

Measurements of the x-ray diffuse scattering with no field applied to the sample were collected around all accessible Bragg reflections in the (001) scattering plane for sample 1. The x-ray scattering is shown in Figure (4.7a) to have ridges of intensity extending from the Bragg reflections along the [110] and crystallographically equivalent directions to the Brillouin zone centre. Similar streaks at low temperatures (77 K) were observed by Krause et al(1971) using the technique of electron diffraction. The wavevector dependence of the scattering is

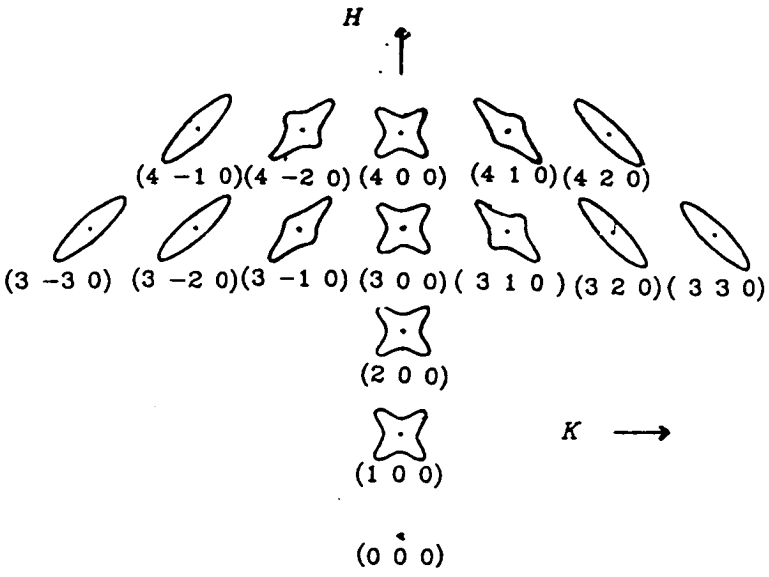

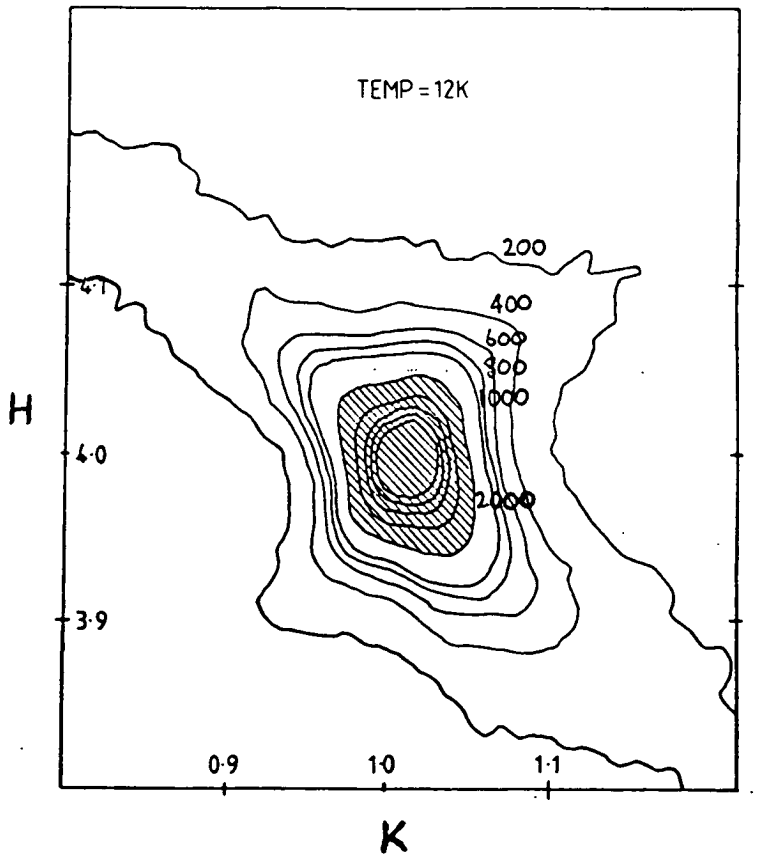

Figure (4.7). (a) A map showing the form of the iso-intensity contours obtained around all accessible Bragg reflections in the (001) plane for wavevector transfers $\mathbf{Q} = (Q_x, Q_y, 0)$ at low temperatures. H and K refer to the [100] and [010] cubic axes. (b) A grid wavevector scan over the (410) Bragg reflection showing the wavevector dependence of the scattering intensity in more detail.

The hatched area in the figure denotes the region where the contour levels are plotted in intervals of 2000 counts/30 s, elsewhere the contours are plotted in intervals of 200 counts/30 s.

shown in Figure (4.8) for scans along the [110] and [1$\bar{1}$0] direction around the (410) and (300) Bragg reflections. Cubic or tetragonal symmetry for centrosymmetric crystals constrains the scattering intensity in the (001) plane to have mirror symmetry about the [100] axis direction. The anisotropy in intensity for the (300) Bragg reflection about the [100] direction may be due to a systematic error or a non symmetric space group. Application of the absorption and polarisation corrections , equations (4.12) and (4.13), decreased the asymmetry to less than 3%. This residual discrepancy may reflect the simplicity of the assumptions made to derive the analytic form for the corrections applied.

The wavevector dependence of the diffuse scattering by acoustic phonons ,equations(4.4) and (4.5), or 180° and 90° domain walls, equations(4.7)and (4.10) respectively, should obey a power law around each Bragg reflection for q<< $\frac{2\pi}{a}$: Consequently the diffuse scattering intensity I(q) was fitted to the empirical form given by:

$$I(q) = A_1 q^{-A_2} + A_3 + A_4 q \qquad (4.14)$$

where $A_1..A_4$ were parameters determined by the least squares method. Parameters A_3 to A_4 were identified with a linear background due to the processes discussed in the summary of Section (4.3.2), and A_1 is a scale factor. The program called domfit was written in Fortran 77 and ran on the ICL 2900 computer. Values for χ^2 were close to 1.0 for all the data fitted and Figure (4.8) shows equation (4.14) provides a good representation of the data for $0.03 < q < 0.15$ r.l.u. The data were only fitted over this range because the results obtained were less sensitive to the estimate for the background contribution.

From Section (4.3) phonon scattering gives values for $A_2 \leqslant 2$, and for domain wall scattering $A_2 \geqslant 2$. The values for A_2 obtained from fitting equation(4.14) to the data around the favourable Bragg reflections, Table (4.1), for wavevector scans along the [1$\bar{1}$0] direction are close to two. The Debye temperature for lead magniobate taken from ultrasound (Wu and Sladek (1983), 382K) and

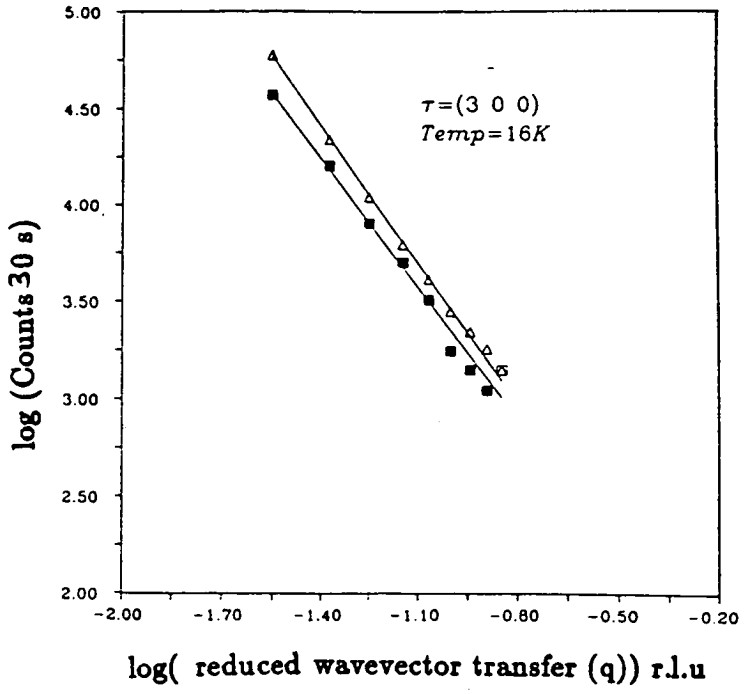

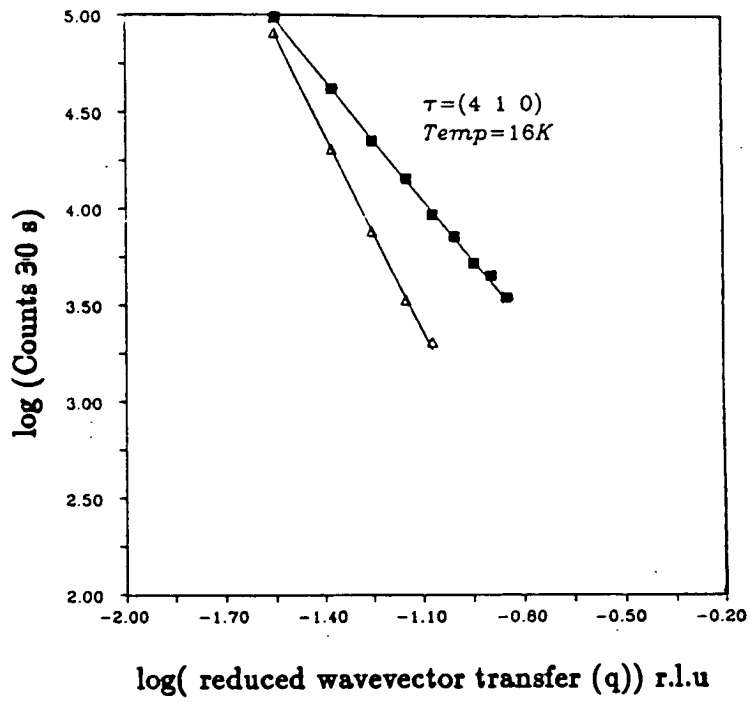

Figure(4.8). (a) and (b) show the x-ray scattering observed for wavevector transfers along the [110]Δand [1$\bar{1}$0]■directions. The solid line is a least squares fit to equation (4.14) in the text and the experimental conditions are noted by the insert. The errorbars are smaller than the symbols used to represent each data point.

HKL(Temp K)	300(16K)	310(16K)	320(16K)	330(16K)	400(16K)	410(16K)	420(16K)
$A_2(110)$	2.3 ± 0.05	2.9 ± 0.1	3.0 ± 0.2	2.7 ± 0.3	2.38 ± 0.1	2.6 ± 0.1	2.8 ± 0.15
$A_2(1\bar{1}0)$	2.3 ± 0.05	2.1 ± 0.06	1.83 ± 0.05	1.94 ± 0.09	2.4 ± 0.07	2.4 ± 0.1	1.9 ± 0.08
HKL(Temp K)	300(16K)	300(150K)	300(240K)	300(270K)	300(300K)	300(373K)	300(543K)
$A_2(110)$	2.3 ± 0.05	2.16 ± 0.04	1.8 ± 0.02	1.67 ± 0.07	1.7 ± 0.1	1.47 ± 0.1	1.48 ± 0.1

Table(4.1) shows the values for A_2 obtained by fitting equation (4.14) to the data. The errors quoted do not include an estimate of systematic ones.

calorimetric (Fouskova (1981)) measurements were used to estimate that equation (4.4) described the one phonon scattering for $q < 0.05$ rlu. This suggests that A_2 should be equal to one for $q > 0.05$ rlu. The values of A_2 obtained from the fitting procedure are systematically higher in the [110] direction than the [1$\bar{1}$0] direction. This may in part be due to the increased difficulty in accurately subtracting the background because of poorer statistics. Substituting the values for elastic moduli determined by Brilloiun scattering (Smolensky et al (1976)) in equation (4.4) the result is obtained that ,for temperatures less than 200 K, the phonon scattering is isotropic around the Bragg reflection.

The temperature dependence of the scattering intensity as a function of wavevector is shown in Figure (4.9). The scattering decreases markedly when the temperature is raised above T_c, and remains almost constant for temperatures below T_c. It is expected, equation (4.4), that the phonon scattering intensity increases linearily with temperature. Inclusion of two and higher order phonon scattering processes in equation (4.1) would change this simple temperature dependence but the intensity would still increase with temperature. Scattering by a soft transverse optic mode would give a divergence in the diffuse scattering intensity close to T_c, equation (4.1) and (1.8). This is not consistent with the data shown in Figure (4.9). The intensity of scattering by domain walls is proportional to the number of domin walls and the atomic displacements within the wall, equation (4.11). An increase in the number of domain walls concomitant with the expected decrease in the atomic displacement magnitude as T_c is approached would give a temperature dependent scattering intensity consistent with that shown in Figure (4.9).

It is therefore proposed that the scattering is by interfaces seperating small ferroelectric domains within which the polarisation is oriented along the [100] and crystallographically equivalent directions. The absence of oscillations in the wavevector dependence of the scattering intensity suggests

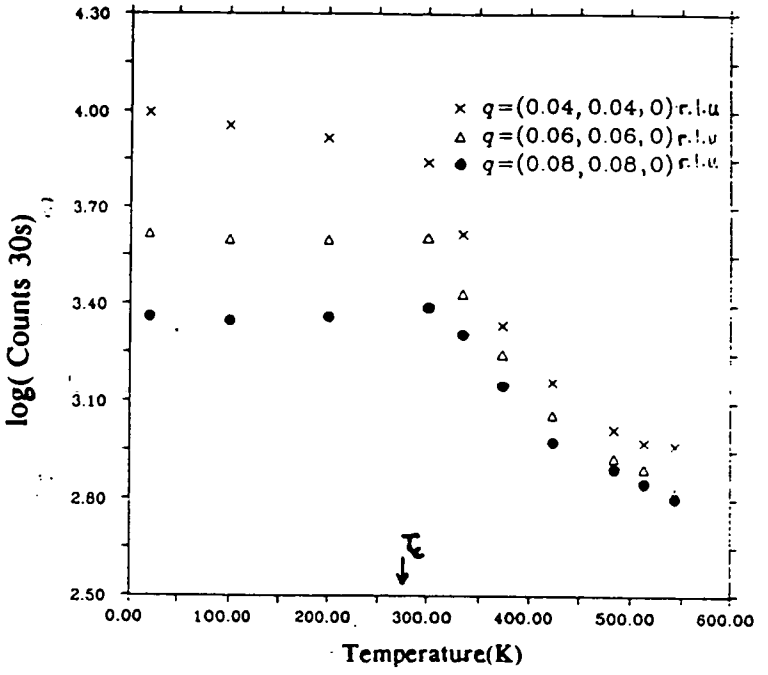

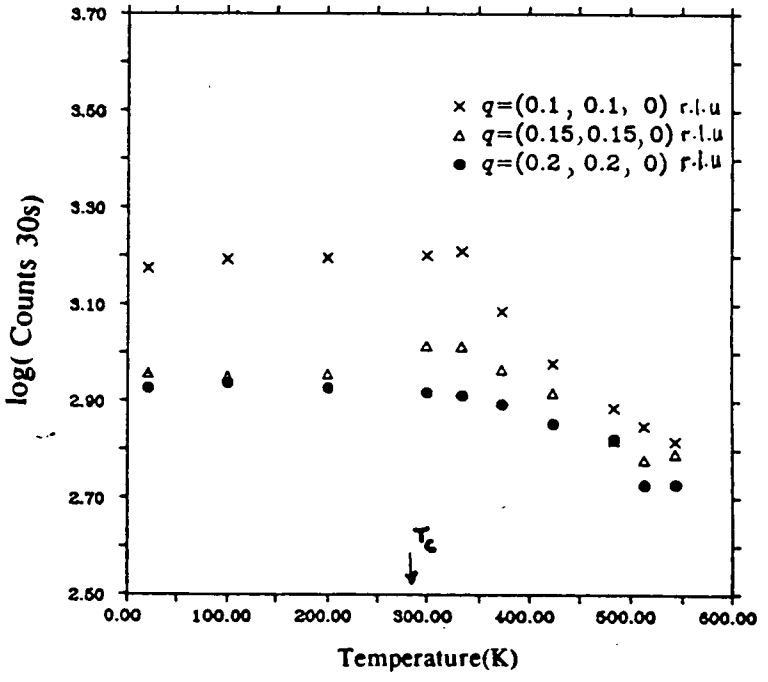

Figure(4.9).(a) and (b) show the temperature dependence of the intensity observed with the diffractometer set at the wavevector noted by the insert. The data recorded using the furnace were normalised at room temperature to the data taken in the cryostat. The errorbars at each point are smaller than the size of the symbol and $\tau = (300)$.

(Bruce 1981) that the maximum domain wall width is one lattice constant.

Figure (4.10) shows the intensity of scattering for scans transverse to the ridge of scattering along the $[1\bar{1}0]$ direction, close to the (300) Bragg reflection. The width of the streak decreases as we approach the Bragg peak until at q = (.05, .05, 0) r.l.u where it becomes comparable to the magnitude of the resolution limit. The shoulder on the peak centred at q = (.05, .05, 0) r.l.u was temperature independent and is believed to be due to the crystal mosaic.

The lineshape of the diffuse x-ray scattering measured for wavevector scans transverse to the streak direction was fitted to the empirical form:

$$I(q) = \frac{B_1}{q^2 + B_2^2} + B_3 + B_4 q \qquad (4.15)$$

where $B_1..B_4$ were parameters determined by the least squares method. B_3 and B_4 where identified with the background due to process described in Section (4.3.2) B_1 is an overall scale factor and B_2 an intrinsic wavevector width. Several typical wavevector scans and fits are shown in Figure (4.10) and equation (4.15) is shown to give a good representation of the data. Typical values for χ^2 obtained from the procedure above were about 1.0 for the data fitted. Other functional forms were tried, Gausssian and Lorentzian squared, but equation (4.15) consistently gave the best fit as judged by χ^2.

Figure(4.11) shows the values for B_2 obtained from the fitting procedure described above plotted as a function of temperature. The streak width depends on the wavevector, and at the lowest temperature is not resolution limited. This suggests that the domain is not of macroscopic extent parallel to the wall. The parameter B_2 is independent of temperature below T_c and suggests that the domain interface roughness is dominated by impurity defects. However, as the sample temperature is increased above T_c there is a marked increase in B_2. due to the

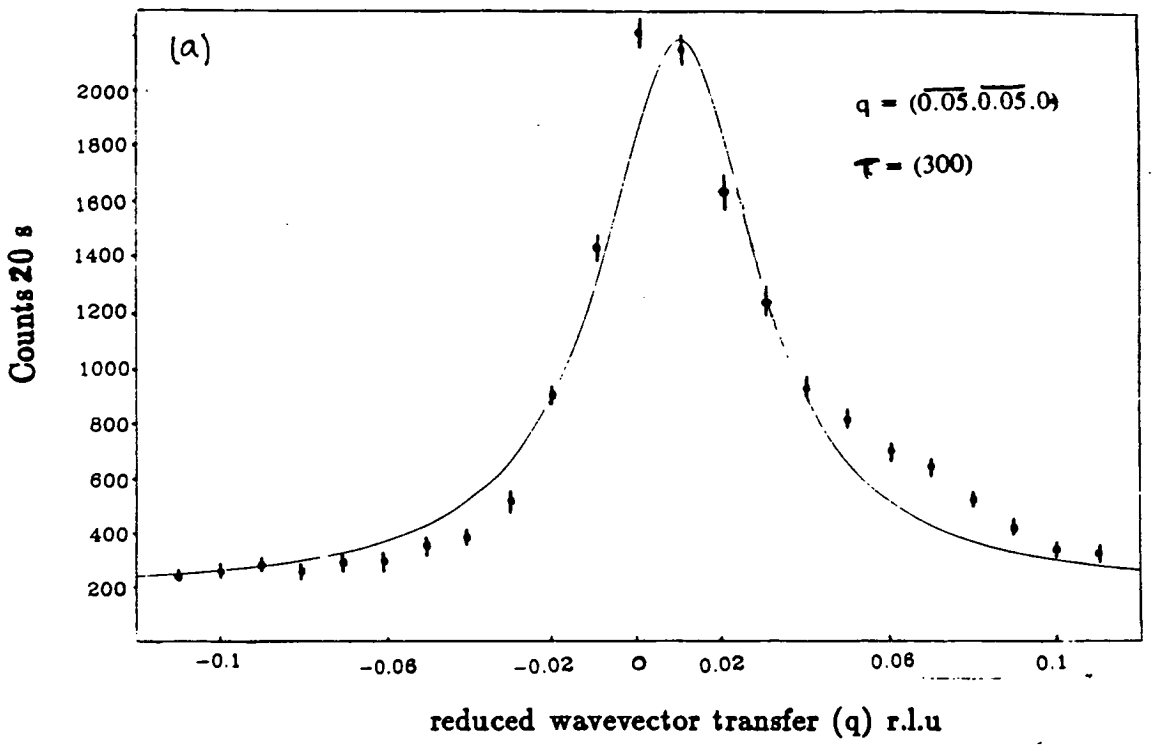

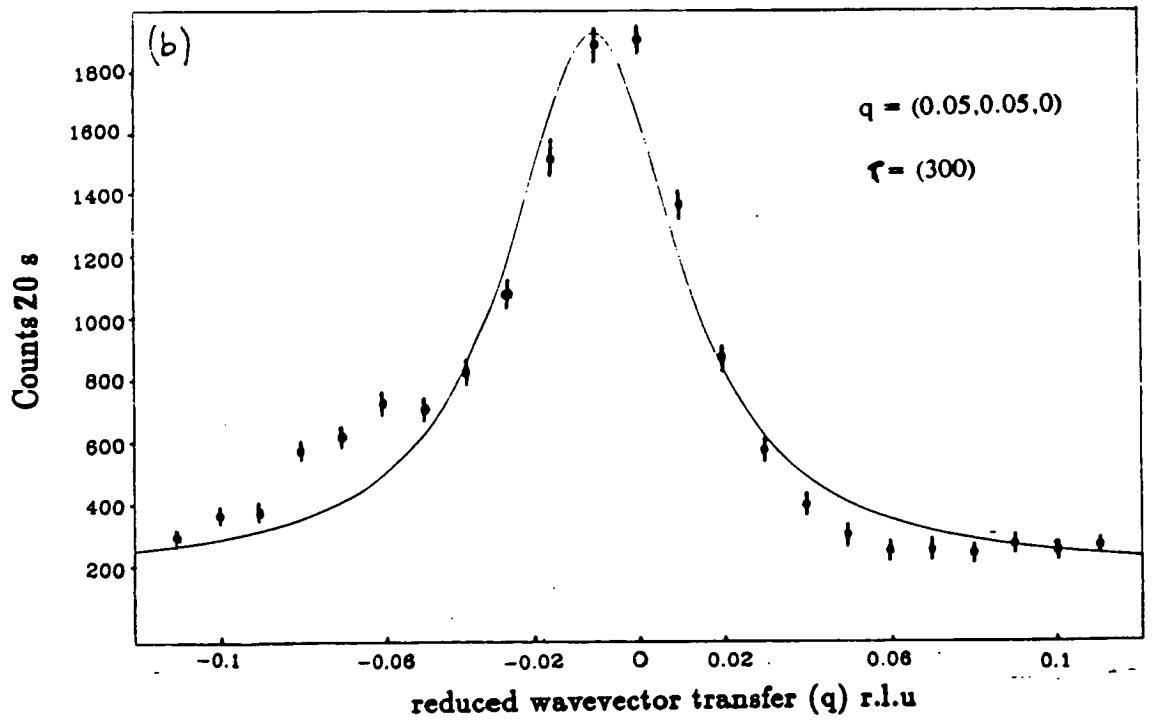

Figure(4.10) X-ray scattering intensity observed for wavevector scans transverse to the streak of diffuse scattering along the [110] directions. The solid line is a least squares fit to equation (4.15) in the text and the data points are shown with errorbars. The midpoint of the wavevector scan is determined by the insert and the sample temperature was 60K.

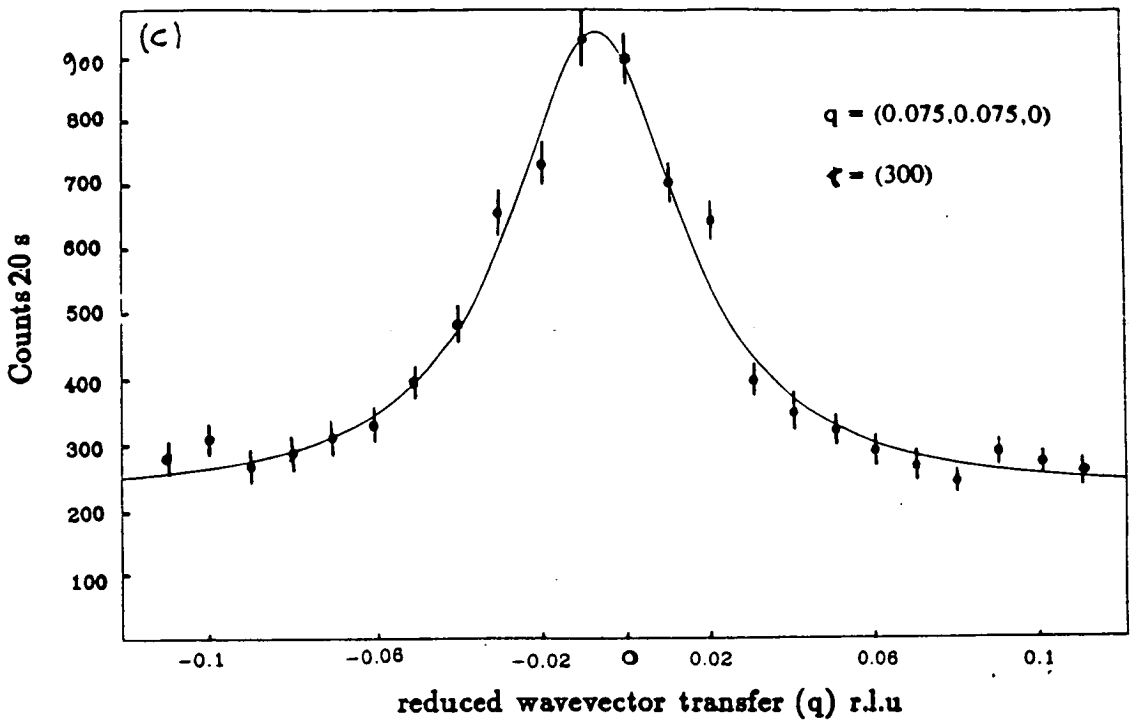

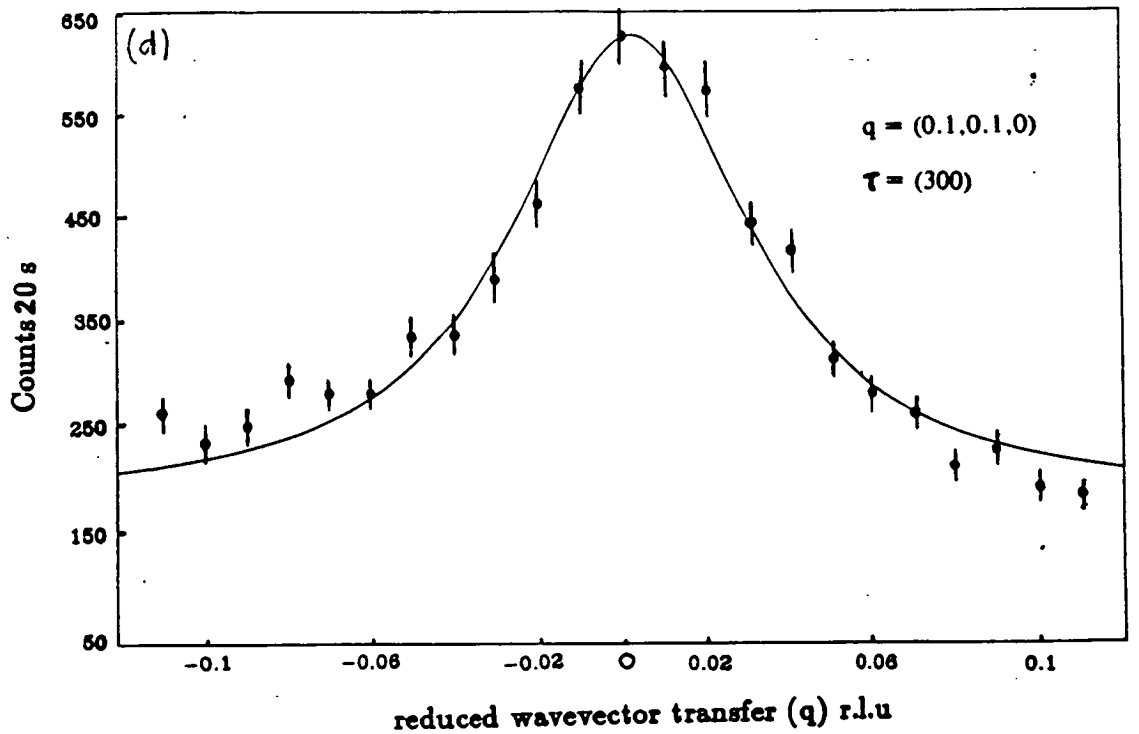

Figure(4.10) X-ray scattering intensity observed for wavevector scans transverse to the streak of diffuse scattering along the [110] direction. The solid line is a least squares fit to equation (4.15) in the text and the data points are shown with errorbars. The midpoint of the wavevector scan is determined by the insert and the sample temperature was 60K.

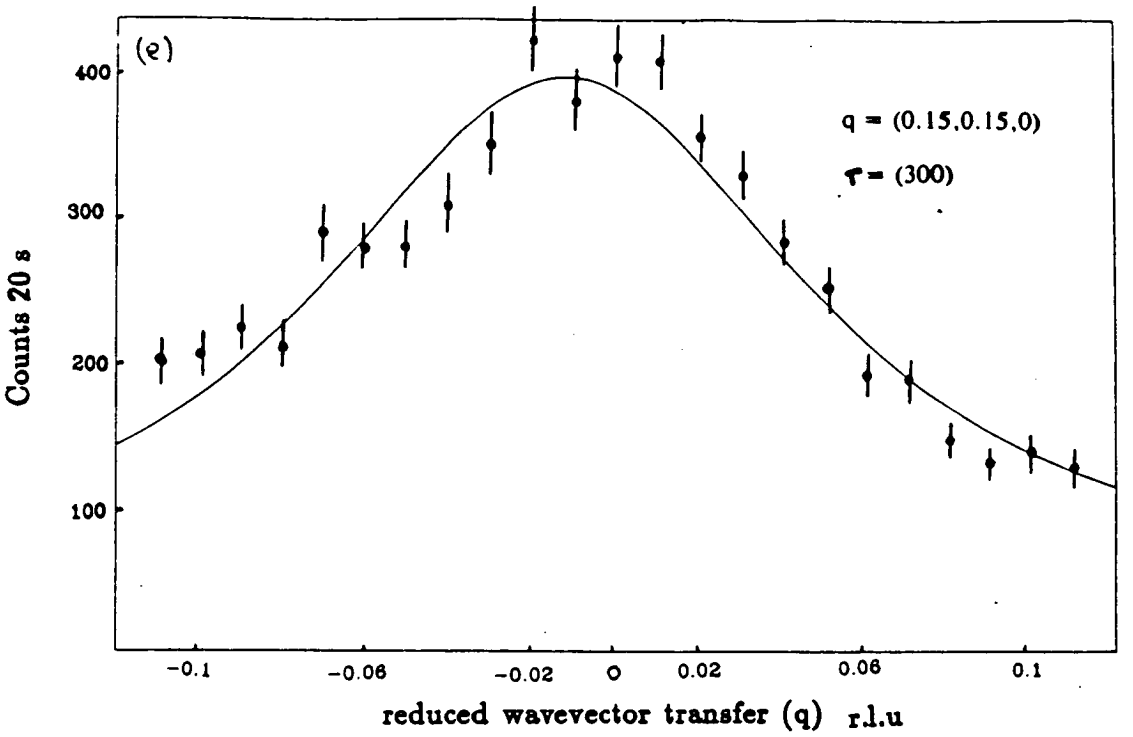

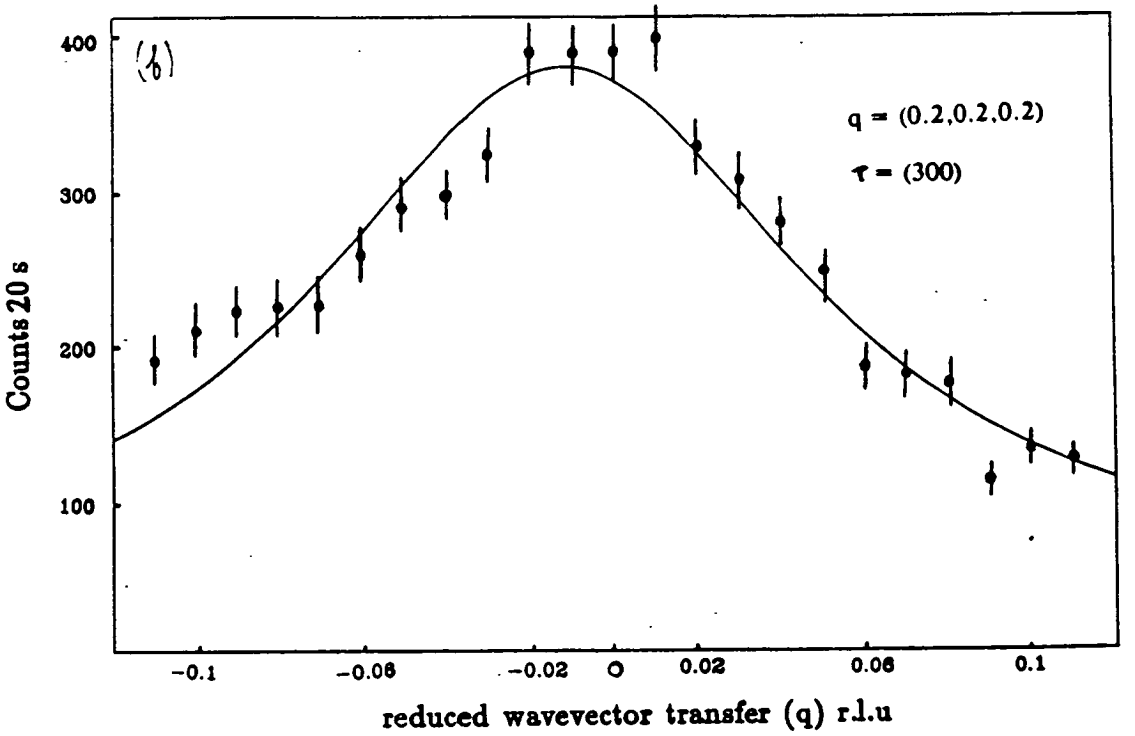

Figure(4.10) X-ray scattering intensity observed for wavevector scans transverse to the streak of diffuse scattering along the [110] direction. The solid line is a least squares fit to equation (4.15) in the text and the data points are shown with errorbars. The midpoint of the wavevector scan is determined by the insert and the sample temperature was 60K.

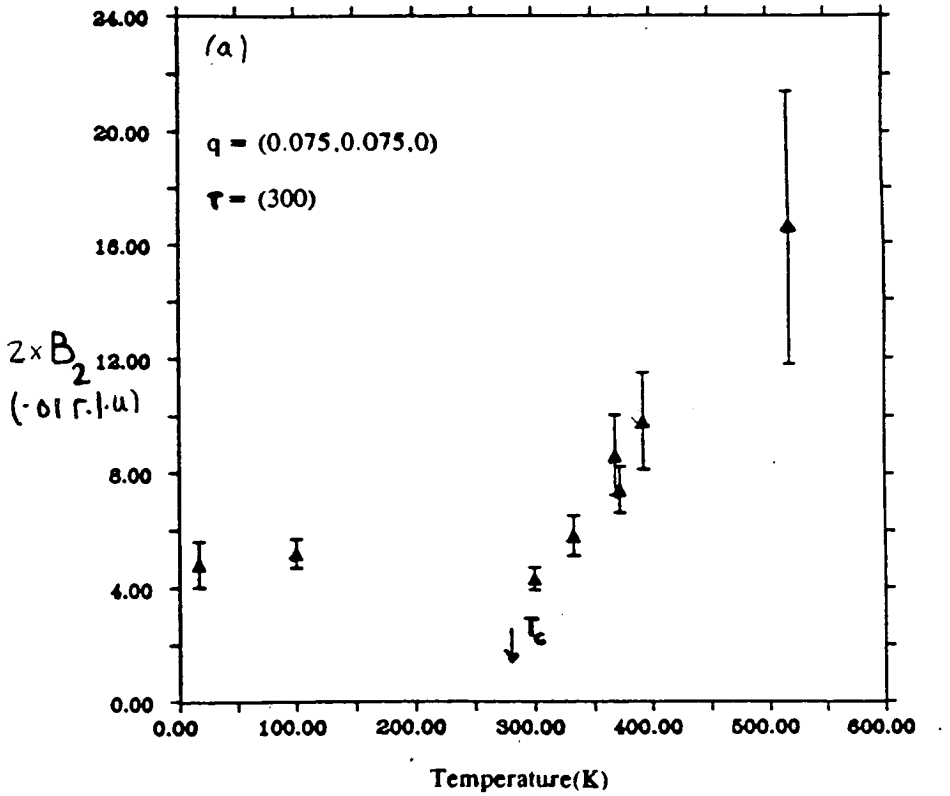

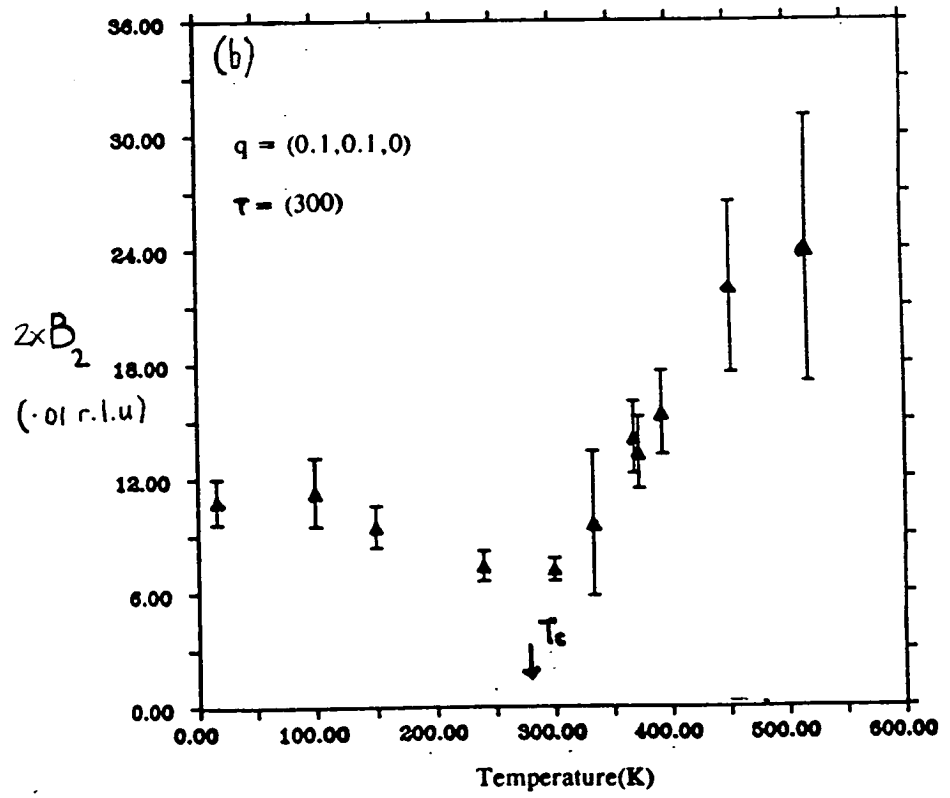

Figure(4.11) shows the parameter B_2 determined by the fitting procedure discussed in the text plotted as a function of temperature and shown with errorbars. The parameters τ and q at which the diffractometer was set are noted by the insert.

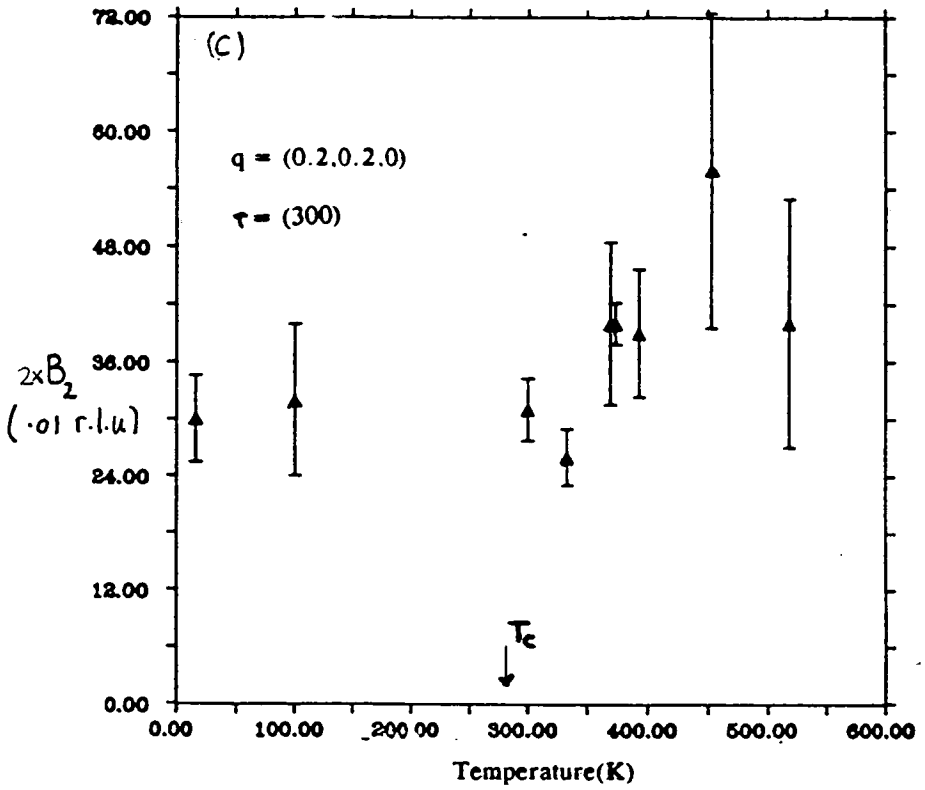

Figure(4.11) shows the parameter B_2 determined by the fitting procedure discussed in the text plotted as a function of temperature and shown with errorbars. The parameters τ and q at which the diffractometer was set are noted by the insert.

freezing out of small ferroelectric domains, distributed throughout the crystal volume, at a Curie temperature determined by the extent of local deviation from stoiciometry.

Domain growth may be equivalent to a change in the domain roughness. In Section (4.3) it was shown that as the domain wall roughens the scattering intensity is decreased by a Debye-Waller like factor. Wavevector scans were therefore made along the [110] and [1$\bar{1}$0] directions around all the accessible reflections for a fixed temperature in the range 16K to 540K. Figure (4.12) shows the wavevector dependence of the scattering intensity near the (300) Bragg reflection. The data were fitted to equation (4.14) by the method described in Section (4.3.1) and the values of A_2 obtained are presented in Table (4.1). The parameter A_2decreases slightly with temperature. This suggests that there is no roughening of the domain walls. However, in this temperature range the number of domain walls and atomic displacements decreases with a concomitant and significant decrease in scattering intensity. Therefore, the accurate subtraction of the background scattering is critical. This is a difficult task over a large temperature range, because the exact temperature dependence of the background is unknown.

In this section the wavevector and temperature dependences of the x-ray scattering measured around the (300) Bragg reflection have been reported in detail. Results obtained around other reflections were qualitatively similar. The results presented were obtained by heating the sample steadily after one particular cooling. When the sample was thermally cycled the x-ray scattering intensity changed, and was systematically higher or lower by around 10-20%. This lack of reproducibility is characteristic of systems with metastable states and competing interactions. However the values for A_2 and B_2^2 obtained by fitting equations(4.14) and (4.15) to the data remained constant to within statistical error.

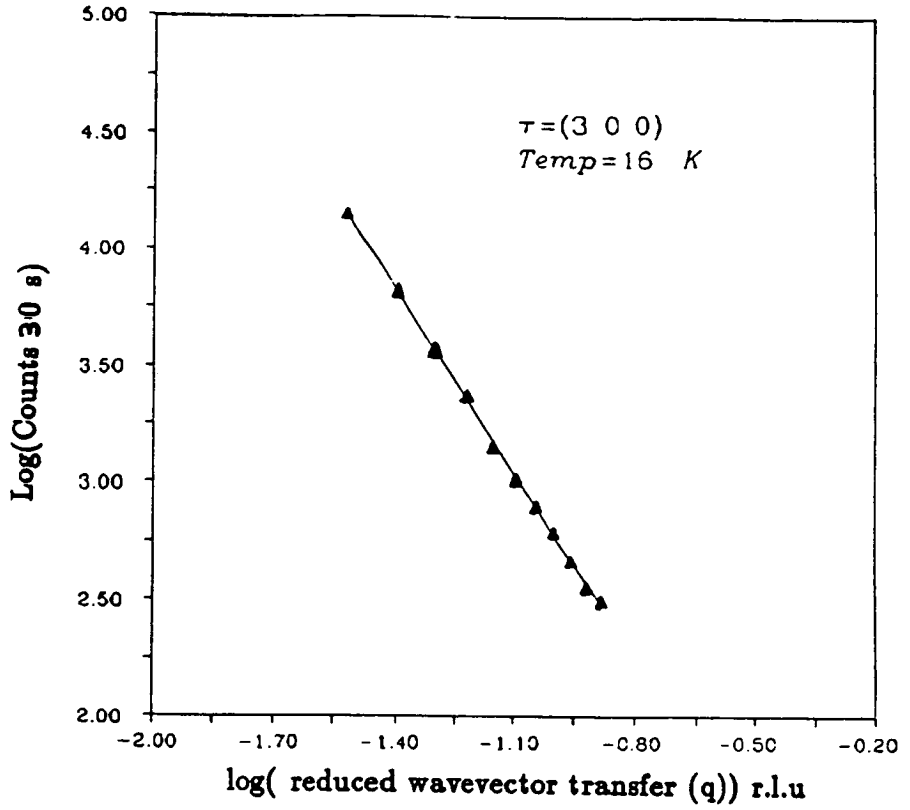

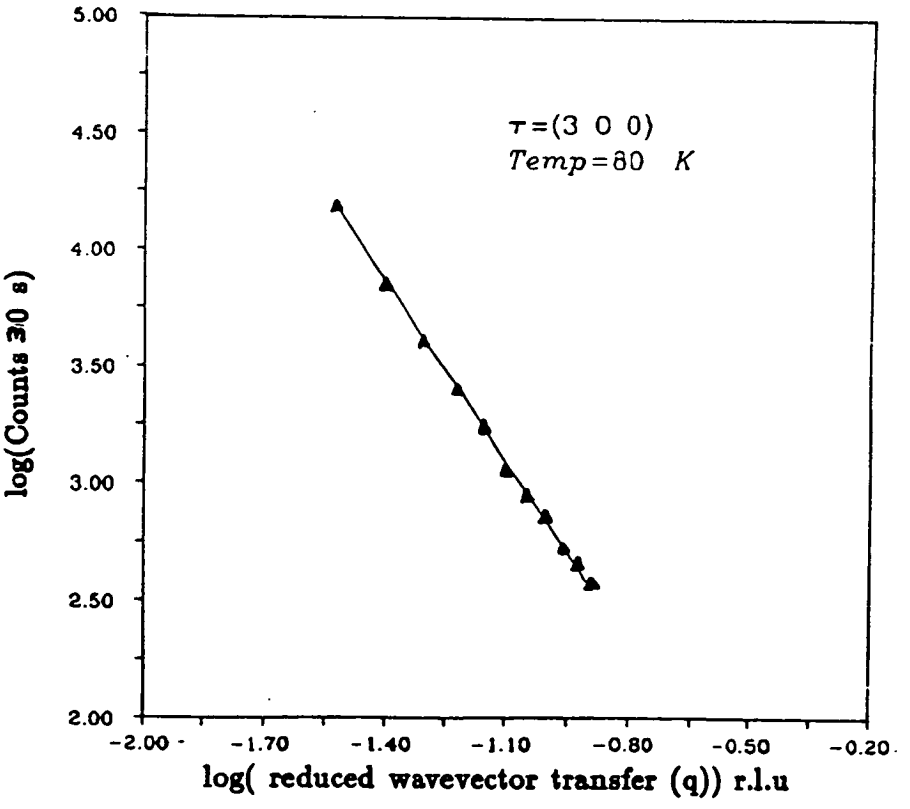

Figure(4.12) shows a typical wavevector scan along the [110] direction. The solid line is a result of a fit to equation (4.14); the errorbars are smaller than the physical symbols that represent each point.

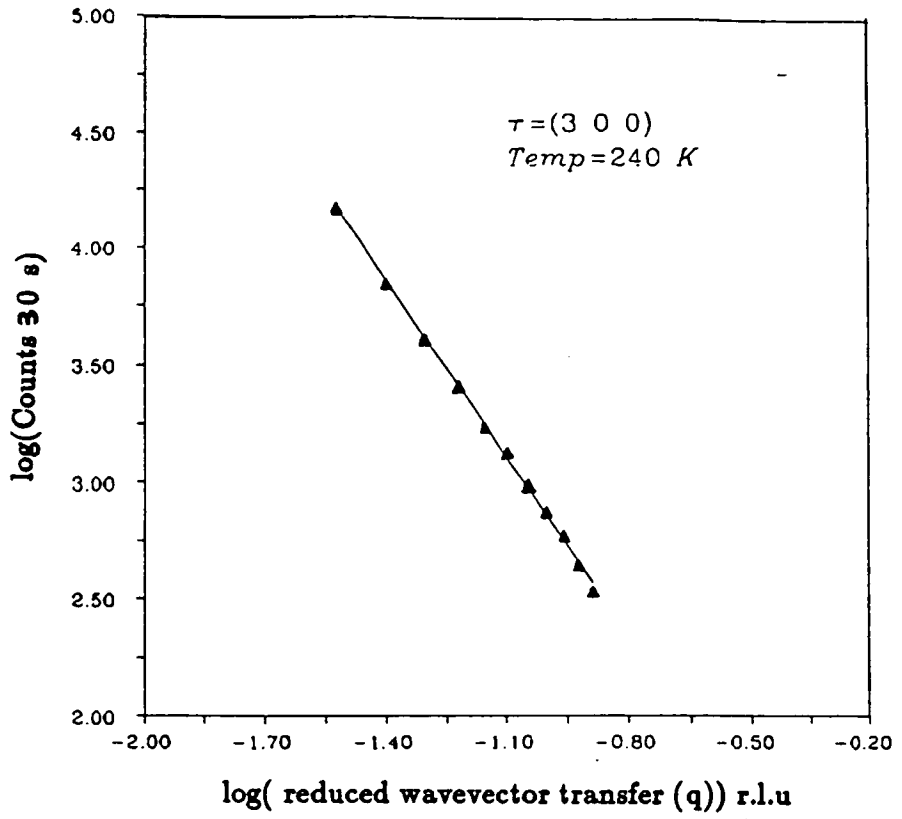

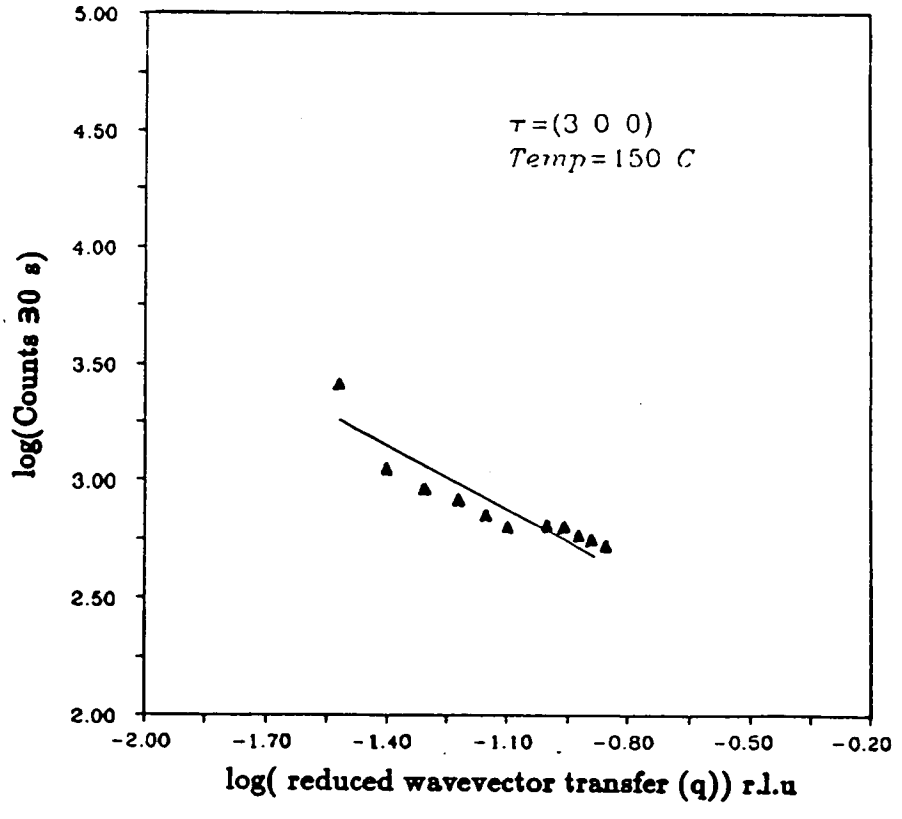

Figure(4.12) shows a typical wavevector scan along the [110] direction. The solid line is a result of a fit to equation (4.14); the errorbars are smaller than the physical symbols that represent each point.

Careful wavevector scans along the [100] direction at 12K through the (400) cubic phase Bragg reflection did not resolve any peak splitting because of the formation of tetragonal domains with a c axis parallel or perpendicular to the crystal face. Further measurements were made using higher resolution and are reported in the next section.

4.5.2 High resolution diffraction measurements

High resolution x-ray diffraction measurements were made between 12K and room temperature. Below T_c the absence of the cubic phase Bragg reflection splitting into two peaks along the [100] direction because of the formation of tetragonal domains suggests both the absence of a macroscopic symmetry change in the low temperature phase and long range order. Andrews(1985) has reported a similar result for the low temperature phase of $KTaO_3$:1.6%Li and $KTaO_3$: 1.7%Nb. Courtens et al (1983) have observed the absence of a macroscopic symmetry change for $R_xA_{1-x}DP$[1] crystals for x in the range $0.22 < x < 0.8$. More detailed measurements of the Bragg peak lineshape for wavevector scans along the [100] direction were made for temperatures between 12K and 300K. The Bragg peak lineshapes were fitted by the method of least squares to the sum of two Lorenztians and a linear background. This is the functional form which gave the best fit, as judged by χ^2. The combined FWHM of the fitted functions were temperature independent and an upper bound of $1.0017 \pm (5)$ was placed on the $\frac{c}{a}$ ratio. This is consistent with single crystal x-ray diffraction measurements (Sizykh et al(1987)) that reported a splitting along the [100] axis of $0.0004\mathring{A}^{-1}$ at low temperatures. Use of the empirical relationships between atomic displacement and T_c (Abrahams et al (1968)) give a value for c/a = 1.0029+(5). The value for T_c was obtained from the permittivity measurements of Bonner et al (1967).

[1] Solid solutions of ferroelectric RbH_2PO_4 and antiferroelectric $NH_4H_2PO_4$ are denoted Rb $_x$ $NH_{4-x}H_2PO_4$, where x refers to the fraction of each component. The deuterated compound, hydrogen replaced with deuterium, is known by the acronym RADP, where R, A, D, and P denote Rhubidium, Ammonia, Deuterium and Phosphorous respectively.

Barium titanate has a spontaneous polarisation value of $26\mu c/cm^2$ and is similar to that of lead magniobate, 20 $\mu c/cm^2$. However on cooling barium titanate from the cubic to the tetragonal phase the cubic Bragg reflection is clearly split into several peaks from which a $\frac{c}{a}$ ratio of around 1.01 may be estimated. This suggests that the magnitude of the polarisation may be extremely inhomogeneous in lead magniobate.

4.5.3 Diffuse scattering in the $(0\bar{1}1)$ plane

In order to validate the domain wall model discussed in Section (4.3.1), further diffuse scattering measurements were made in the $(0\bar{1}1)$ plane. Wavevector scans perpendicular to the [011] and $[0\bar{1}\bar{1}]$ directions around all accessible Bragg reflections were made and are shown in Figure (4.13) for the (300) Bragg reflection. The data shown in the figure suggest that the scattering intensity in this plane is negligible. This is consistent with the result for the structure factor for 90° walls, equation (4.11), calculated for this plane.[1] Along the high symmetry directions, such as the [110], the phonon modes are constrained by symmetry to be purely transverse or longitudinal. From equations (4.1) and (4.2) the phonon structure factor is non-zero for a longitudinal and transverse acoustic mode with $\underline{\xi}$ parallel and perpendicular respectively to the [110] direction. This is further support for the intrepretation of the results given in these sections.

Figure (4.14) shows a grid wavevector scan over the (300) Bragg reflection at room temperature. Streaks of diffuse scattering along the [211] and crystallographically equivalent directions are clearly visible. This scattering was found around all reflections accessible,(400), (300), (411), $(4\bar{1}\bar{1})$, (311) and $(3\bar{1}\bar{1})$ in the plane. Qualitatively the scattering was similar to that in the (001) plane. The scattering intensity along the [211] and $[2\bar{1}\bar{1}]$ directions became more anistropic with increasing wavevector transfer and decreased in intensity after heating from 12K to room temperature. Figure (4.15) shows the wavevector dependence of the scattering along the ridge of intensity compared to that found in the (001) plane. The values obtained for A_2 and B_2, by the fitting procedure described

[1] Under the experimental conditions the term $(u_k(r+q))$ is well approximated by $(Q.u_k)$. Scans close to (300) have Q close to the direction given by [100]. Substitution of the direction vectors Q=[100] and u_k=[011] into the term $(Q.u_k)$, with the exception of constants, gives the result for the structure factor equal to zero. The structure factor is therefore negligible in this plane.

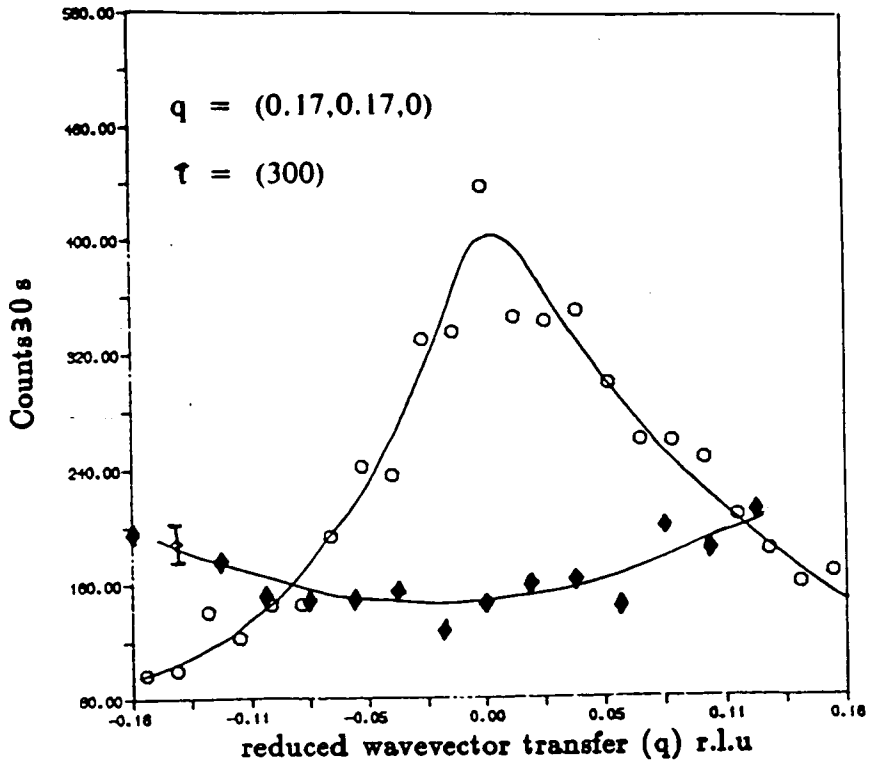

Figure(4.13) shows the x-ray scattering intensity observed when the wavevector transfer was varied along the [100] direction in the (0$\bar{1}$ 1) plane and when the wavevector transfer was varied along the [1$\bar{1}$0], , in the (001)plane. The mid point of the scan is noted by the inset and the solid line is a guide to eye.

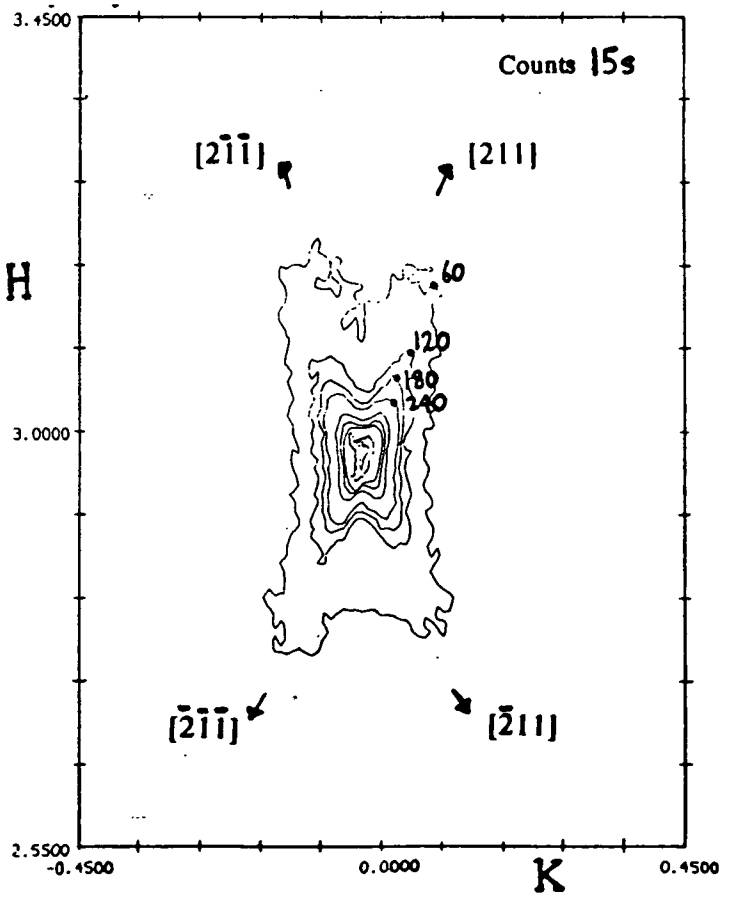

Figure(4.14). A contour map of the x-ray scattering intensity in the (0$\bar{1}$ 1) plane around the (300) Bragg reflection at room temperature. H and K denote the [100] and [011] cubic crystallographic direction.

in Section(4.5.1), are the same, within error, as those obtained for the data presented in Section (4.5.1) This suggests that the physical origin may be the same for the streaks along [011] and [211] type crystallographic directions.

Scans through all the accessible $q = \left(\frac{1}{2}\frac{1}{2}\frac{1}{2}\right)$ r.l.u positions in the plane showed the presence of very weak superlattice peaks as reported in the electron diffraction measurements of Krause et al(1971,1979). Great care was taken to eliminate the possibility of $\frac{\lambda}{2}$ contamination as the possible origin of the scattering. A wavevector scan along the [010] direction through the superlattice reflection position is shown in Figure (4.16). The wavevector dependence and intensity of the scattering was found to be independent of temperature between 12K and 545K The simplest empirical form that represented the superlattice peak, as judged by χ^2 was a Gaussian. The resolution contribution to the width of the Gaussian fitted to the peak by the method of least squares was assumed to be negligible. The value obtained by this procedure for the peak width suggests that the ordering is isotropic and extends over 10 to 20 unit cells. Krause et al(1979) attribute these superlattice reflections to the partial ordering of Mg and Nb ions on the B site over microscopic distances

The destruction of sample 1 required further measurements to be made with a second crystal, sample 2. However these measurements showed the presence of intense streaks, in the form of arcs, near the (300) Bragg reflection and Q = (3.5 0.5 0.5) r.l.u superlattice position, Figure(4.17), that were identified as powder lines from the (211) and (222) cubic phase Bragg reflections. These reflections have low Bragg angles, around 30^0, and consequently are sensitive to the surface quality. The presence of intense powder lines around the favourable reflections for study prevented further more detailed measurements of the wavevector and temperature dependence of the scattering.

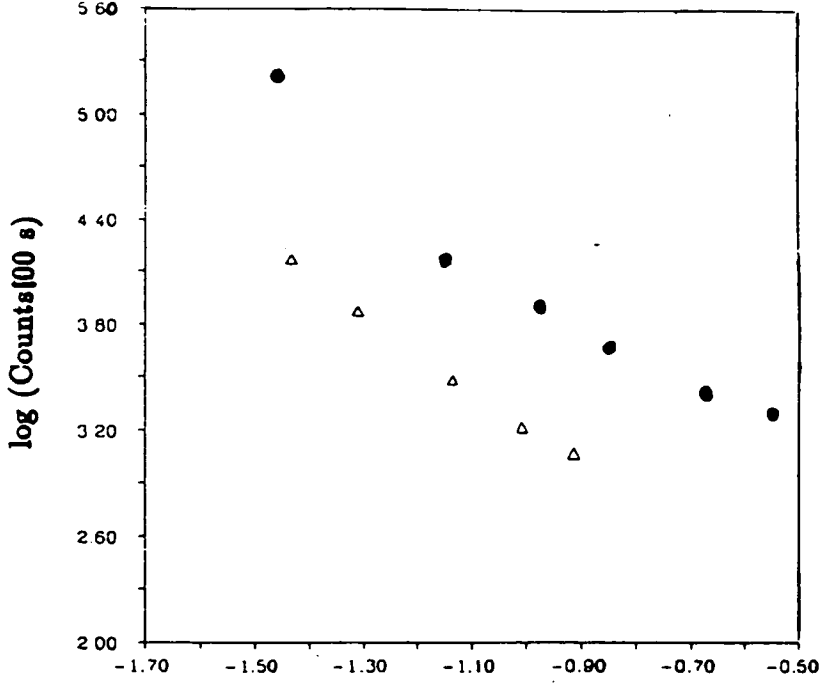

Figure(4.15). X-ray scattering observed for wavevector transfers near the (300) Bragg reflection when the wavevector transfer was varied along the [211] direction in the (0$\bar{1}$1) plane, Δ, and the [110], direction, ●, in the (001) plane. The errorbars are smaller than the symbols used to represent the data points and the temperature was 200K.

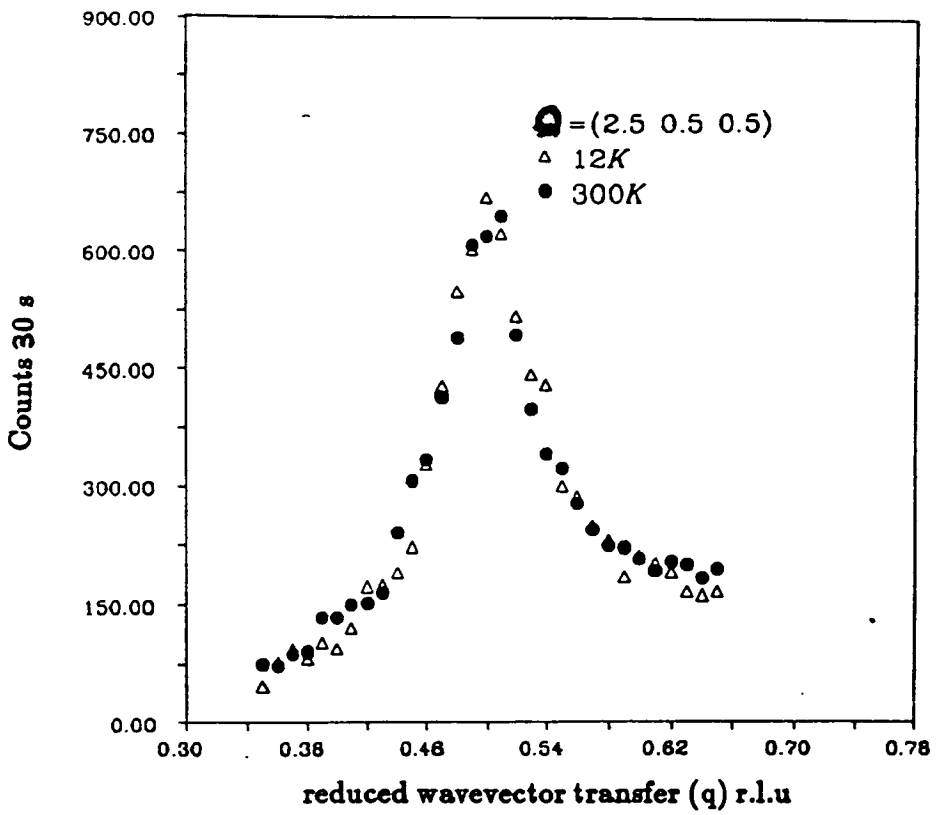

Figure(4.16). X-ray scattering observed for wavevector transfers along the [001] direction through the Q = (2.5 0.5 0.5) superlattice reflection. The experimental conditions are noted by the insert.

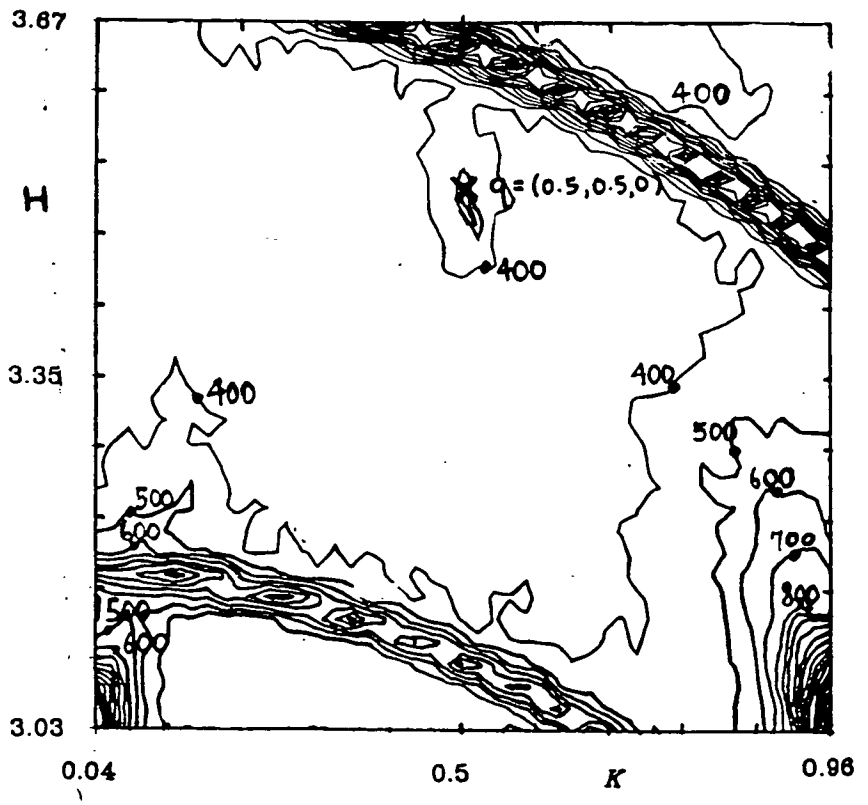

Figure(4.17) A grid wavevector scan in the $(0\bar{1}1)$ plane centred near the Q = (3.35,0.35,0.35)r.l.u position showing the wavevector dependence of the diffuse scattering observed along the <211> type crystallographic directions. The scattering intensity was recorded for 30 seconds at each point and the sample temperature was 30K. The superlattice reflection at Q = (3.5,0.5,0.5)r.l.u is shown clearly also at X.

4.5.4 Electric field dependence of the diffuse scattering

The results reported in this section were obtained using sample2 oriented with an [0 0 1] axis vertical. In this geometry the (3 0 0) Bragg reflection is much less sensitive to the quality of the crystal surface because of the higher Bragg angles of the neighbouring reflections: all measurements subsequently presented were performed here. After cooling through the transition in an electric field of 10KV/cm applied along the [010] direction wavevector scans were made along the [110] type directions as a function of temperature. The intensity is almost temperature independent below 280 K, Figure (4.18), and is in qualitative agreement with the results presented in Section(4.5.1). The scattering intensity is suppressed compared to that obtained with no field applied, Figure (4.19). It is energetically favourable for the dipole moment to align, subject to crystal constraints, along the field direction. It is believed that the scattering is suppressed because of the preferential domain growth along the electric field direction with a concomitant decrease in the number of domain walls.

The state prepared above is known as the field cooled state (FC) and is distinct from the zero field cooled state (ZFC) that is obtained by cooling below the transition temperature and then applying a field. For systems where random field effects may be important these states are different, and the ZFC state is expected to grow in time logarithmically slowly (Amin (1989)) towards the FC state. Memory effects are known to be important for such systems and therefore the sample was annealed at room temperature for 12 hours after performing the field cooled measurements. Measurements of the diffuse scattering along the [110] direction for the ZFC state are shown in Figure (4.20) and the relaxation phenomenon typical of systems with competing interactions is clearly observed.

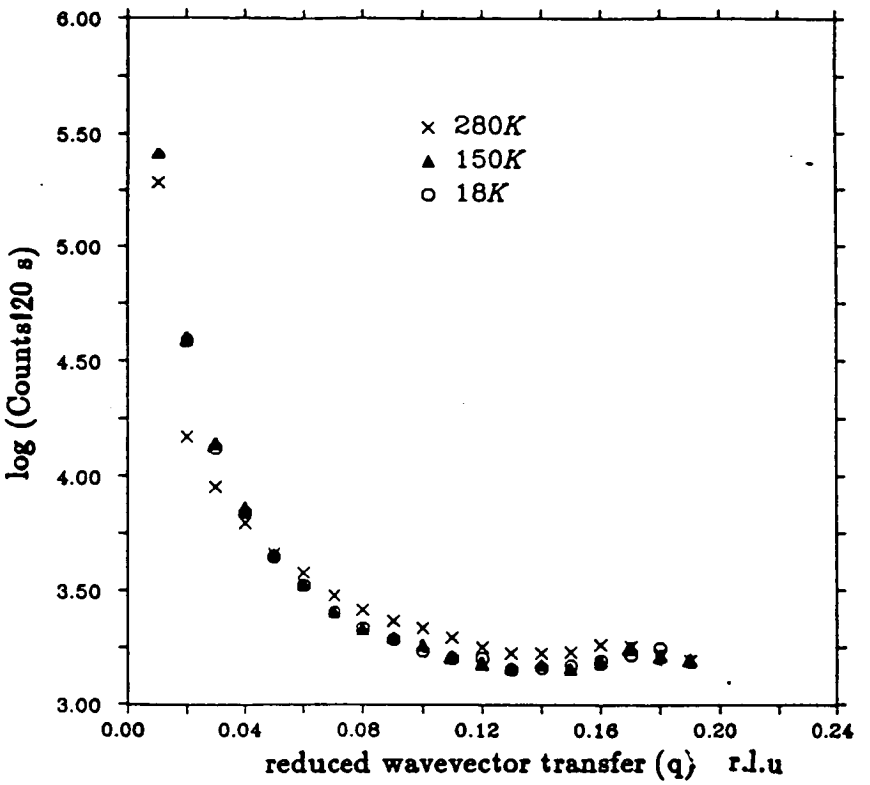

Figure(4.18). X-ray scattering observed for wavevector transfer scans along the [110] direction near the (300) Bragg reflection at a temperature noted by the insert and an applied electric field of 10 KV/cm.

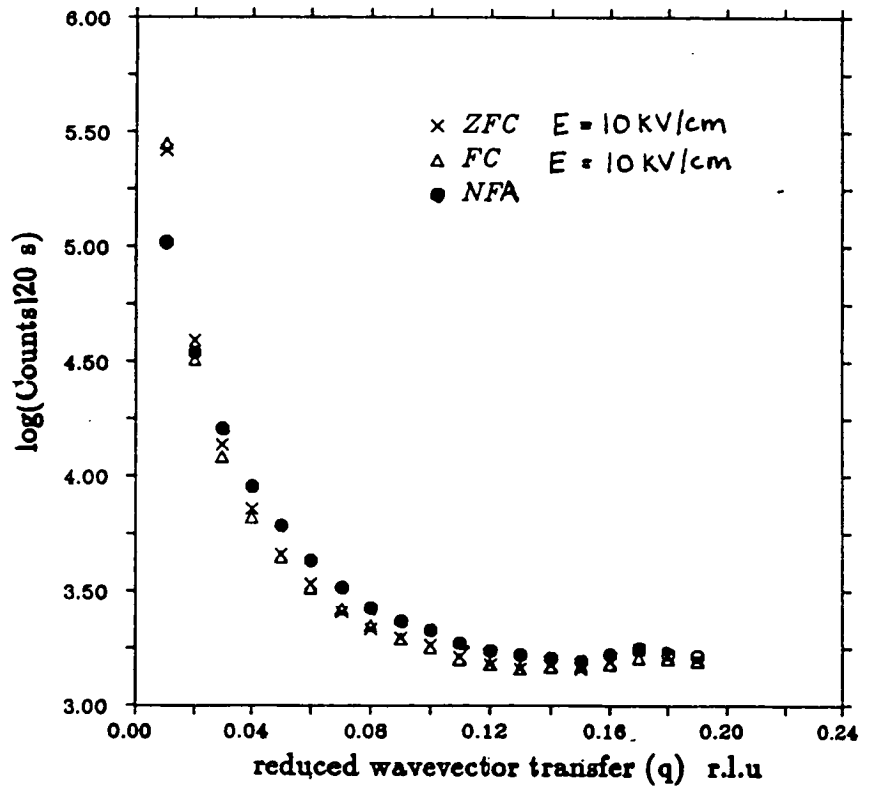

Figure(4.19). X-ray scattering observed for wavevector transfer scans along the [110] direction near the (300) Bragg reflection. The experimental conditions were noted by the insert and the temperature was 150K.

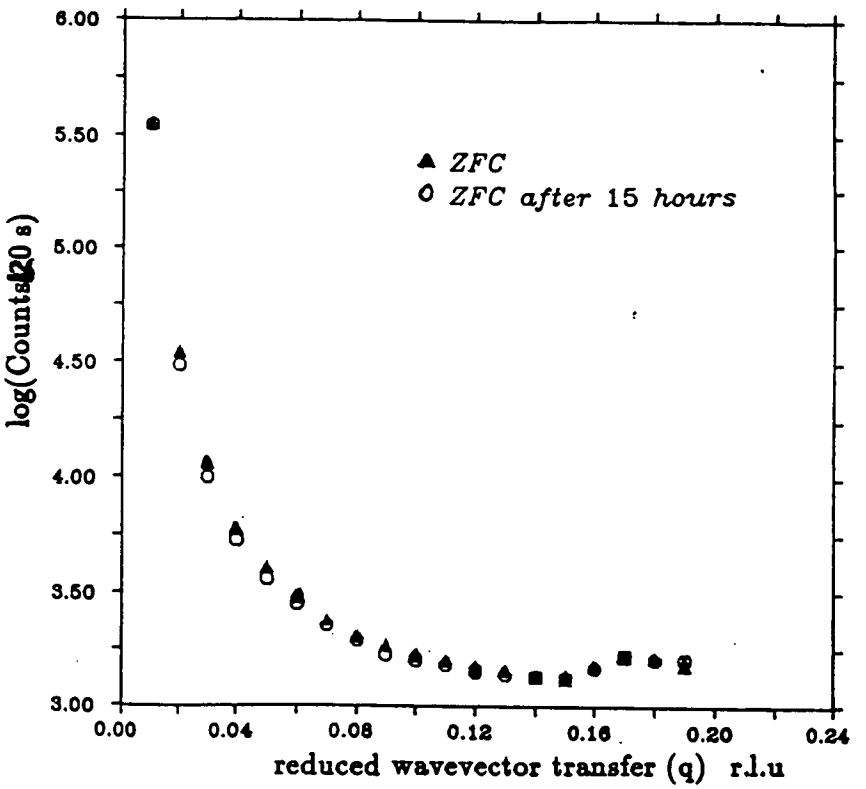

Figure(4.20). X-ray scattering observed for wavevector transfer scans along the [110] direction near the (300) Bragg reflection at a temperature of 150K. The experimental conditions are noted by the insert.

Wavevector scans perpendicular to the streak of diffuse were also performed for the FC and ZFC cases. The data were analysed as described in Section (4.5.1) and the results given in Table (4.2). Surprisingly the values for B_2 for the ZFC and FC states are ,within statistical error, the same as for the NFA state. If the domain model is correct the growth of the domains under the action of the applied field should result in an increase in the lateral dimension of the wall and a subsequent decrease in the width of the diffuse scattering. The failure to observe this result may well be due to the poor statistical precision of the data and the long timescales (Amin (1989)) required for the domains to reorient themselves and reach equilibrium.

The cubic phase Bragg reflections did not split into several peaks even after cooling the sample to 12K. The presence of diffuse scattering ruled out the possibility of a single domain sample. The resolution for these measurements was improved by 20% over those values given in Section (4.2.1) by reducing the size of the vertical and horizontal dimension of the pre-monochromator slit , Section(4.3). Sizykh et al (1987) report a lattice parameter change, c-a, of $0.002\mathring{A}^{-1}$, for a field of 7.5KV/cm applied along the [001] direction. This is consistent with the failure to observe any change in the lattice parameter within the experimental resolution of 0.002 $\mathring{A}^{-1}$.

Attempts to perform further measurements of the diffuse scattering and Bragg reflections at higher fields were unsuccessful because the electrical insulation in the cryostat failed at 15KV/cm.

q(r.l.u)	B_2	experimental conditions	B_1
0.05 0.05 0.0	13.3 ± 2.1	ZFC	3943 ± 223
0.1 0.1 0	11.1 ± 4.5	"	1251 ± 182
0.15 0.15 0	30 ± 9	"	1366 ± 79
0.05 0.05 0	14 ± 2.4	ZFC + 15 hours delay	2878 ± 168
0.1 0.1 0	14.3 ± 6.2	"	1009 ± 130
0.15 0.15 0	28.1 ± 8.5	"	1261 ± 103
0.05 0.05 0	11.8 ± 1.9	FC	3178 ± 173
0.1 0.1 0	9.9 ± 4.3	"	1109 ± 180
0.15 0.15 0	19.8 ± 4	"	1305 ± 99
0.05 0.05 0	9.5 ± 1.4	NFA	5465 ± 308
0.1 0.1 0	7.8 ± 2.8	"	1673 ± 186
0.15 0.15 0	21 ± 5.5	"	1312 ± 101

Table(4.2) shows the values for B_2 obtained from the fitting procedure described in Section(4.5.1). B_2 is in units of 0.0| r.l.u for q and the error bars do not include an estimate of the systematic errors present. FC denotes the field cooled state; ZFC zero field cooled state and NFA, no field applied.

4.5.5 Discussion and Conclusions

Diffuse scattering measurements were made for a single crystal of lead magniobate with a fixed temperature in the range 16K to 620K. Wavevector scans made along the [110] crystallographic directions in the (001) plane showed intense streaks of diffuse scattering that extended from the Bragg reflection to the Brillouin zone centre. Further measurements in the $(0\bar{1}1)$ plane showed that the x-ray scattering along the [110] type directions was negligible. The calculated 90° domain wall structure factors for the (001) and $(0\bar{1}1)$ planes were shown to be in qualitative agreement with the experimental data.

Application of an electric field of 10 KV/cm decreased the intensity of the scattered x-ray distribution, and this was attributed to the reorientation of domains that were unfavourably aligned with the applied electric field. A high resolution diffraction study did not resolve a splitting of the cubic phase Bragg reflections due to the formation of tetragonal domains at the lowest sample temperature. This suggested that an upper bound of 1.0017+(5) may be placed on the tetragonal c/a ratio. It is concluded that the experimental measurements and predictions obtained from the domain wall model are in qualitative agreement for the low temperature phase.

Detailed measurements were made of the temperature dependence of the scattered x-ray distribution for temperatures up to 620K. The intensity and wavevector dependences of the scattered x-ray distributions along the [110] crystallographic directions were, to within experimental error, temperature independent below the temperature were the permittivity maximum occurs. Above T_c the scattering intensity was found to decrease markedly with increasing temperature, but did not become negligible until the temperature reached was close to where a deviation from the normal Curie-Weiss law for the permittivity has been observed. This suggested that a fraction of the ferroelectric domains in the low temperature phase persisted above the permittivity anomaly. It is concluded that the results are consistent with the existence of a phase that consists of many small ferroelectric domains. Low temperature ferromagnetic phases with qualitatively similar structure are observed in systems where random field effects are important.

4.6 Further Work

Detailed measurements of the diffuse scattering should be made to determine the atomic displacements. The atomic displacements are related to the intensity of the sacttered x-ray distribution by the structure factor, equations (4.7) and (4.10). Cowley (1986) has suggested that to accurately determine quantitative information from x-ray scattering experiments the instrumental resolution should be convoluted with the model structure factor before the experimental data is fitted by the method of least squares. The resolution function can be calculated accurately only when silicon or germanium are used as a monochromator and analyser crytsal. Further measurements of the scattered x-ray distribution should be performed with either of these elements as monochromator and analyser.

It would be useful to extend measurements of the Bragg reflections and diffuse scattering to higher electric fields in order to obtain a mono-domain sample. The diffuse scattering should be completely suppressed, and it may be possible to measure the cubic phase Bragg peak splitting and accurately determine the c/a ratio. This should be feasible, because the failure to attain electric fields higher than 10 Kv/cm was due to a breakdown in the electrical insulation of the cryosat and not because of physical processes in the crystal.

It is of interest to investigate further the origin(s) of the superlattice reflections measured at the Brillouin zone centre in the $(0\bar{1}1)$ plane and the streaks of diffuse scattering along the [211] crystallographic directions. At present their origin is not understood, however the existence of an experimental systematic error cannot be completely ruled out.

Appendix 1

The intensity recorded in a neutron scattering experiment, I(t), does not give $\frac{d^2\sigma}{d\Omega d\epsilon}$ directly. Several corrections and mathematical manipulations must be applied and each is discussed briefly below.

I(t) measured in a scattering experiment is given by the convolution of the sample cross section with an instrumental resolution function. To proceed one normally assumes a model for $S(Q,\omega)$ and the convolution of this with the known resolution function is fitted to the data using the method of least squares. The details of the method are specific to the experimental situation and are therefore given more fully in the relevant section of each chapter. Let us ignore the resolution correction for the moment. The results from an experiment are still in the form of counts against some variable angle,wavevector or frequency. We shall now consider the relationship between $\frac{d^2\sigma}{d\Omega d\epsilon}$ and I(t) for the experimental arrangements considered in this thesis.

The triple axis x-ray spectrometer considered in chapter 4 has fixed monochromator and analyser angles so that provided the crystals are large enough to accept all the beam the solid angle and energy decrement remain constant. Consequently $I(t)$ is proportional to $\frac{d^2\sigma}{d\Omega d\epsilon}$. Because of the high flux of the incident x-ray beam, fluctuations are negligible and it is not necessary to normalise each point against the incident beam monitor.

In the case of the triple crystal neutron spectrometer, considered in chapter 3, the monochromator angle is fixed and the analyser angle varies in order to select neutrons of a particular final wavelength. If the collimation of the spectrometer is unchanged then it follows from equations (1) and (2)

$$E_o = \frac{\hbar^2 k_o^2}{2m_n} \qquad (1)$$

$$2k_o sin\theta_A = \tau \qquad (2)$$

that the observed intensity $\frac{d^2\sigma}{d\Omega d\theta_A}$ is related to the measured $I(t)$ by equation (3).

$$I(t) = k_\circ^3 cot\theta_A \frac{d^2\sigma}{d\Omega d\epsilon} \qquad (3)$$

References

C.S., Abrahams, S.K., Kurtz and P.B., Jamieson, Phys. Rev., 172,(1968),551

C.J., Adkins, Equilibrium Thermodynamics (McGraw Hill:Maidenhead (1975))

A., Aharony, Phys. Rev. B, 8,(1973),4270,3342

A., Aharony, and M.E., Fisher, Phys. Rev. B, 8,(1973),3323

A., Aharony, Solid Stat. Commun., 28,(1978),667

U., Ahlers, Phys. Rev. B, 3,(1971),165

J., Als-Nielsen and B., Birgeneau, Am. J. Phys., 45,(1977),554

J., Als-Nielsen, O.W., Dietrich, and L., Passel Phys. Rev. B, 14,(1976),4908

S.J., Amin, (private communication (1989))

S.R., Andrews, J. Phys. C., 18,(1985),1357

G.E., Bacon, Neutron Diffraction (Clarendon Press:Oxford (1975))

G., Bednarz and D.W., Field, Acta. Cryst., 38,(1982),163

M.M., Beg and M., Nielsen, Phys. Rev. B, 14,(1976),4266

P.R., Bevington, Data Reduction and Error Analysis for the Physical Sciences (McGraw-Hill: London (1969))

K., Binder and M., Young ,Rev. mod. Phys., 58,(1986),801

S., Bludman and A., Klein, Phys. Rev., 131,(1963),2364

V.A., Bokov and I.E., Mylnokova, Sov. Phys.: Solid State 3,(1961),613

W.A., Bonner, E.F., Dearborn, J.E., Geusic, H.M., Marcas and L.G., Van Utart, Appl. Phys. Lett., 10,(1967),163

W.L., Bragg, J. Sci. Instr., 24,(1947),27

E., Brezin and D.C., Wallace ,Phys. Rev. B, 7,(1973),232,1967

R., Brout, Phase Transitions (W.A. Benjamin:New York (1965))

A.D., Bruce and R.A., Cowley, Phase Transitions (Taylor Francis:London (1981))

D.A., Bruce, J. Phys. C, 14,(1981),5195

C.F., Buhrer, J. Chem. Phys., 36,(1962),798

G., Burns, Phase Transitions, 5,(1985),261

G., Burns and F.H., Dacol, Solid Stat. Commun., 48,(1983),853

G., Burns and B.A., Scott, Solid Stat. Commun., 13,(1973),423

N.J., Chesser and J.D., Axe, Acta. Cryst. A, 29,(1973),160

H., Clarke, Introduction to Quantum Mechanics (Van Nostrand Reinhold Company: Amsterdam (1984))

W., Cochran, Adv. Phys., 9,(1960),387; Ibid.,10,(1961),401; Ibid., 18,(1969),157

M.F., Collins, V.J., Minkiewicz, R., Nathans,L., Passel and G., Shirane, Phys. Rev., 179,(1969), 417

M.J., Cooper and R., Nathans, Acta. Cryst., 23,(1968),357

E., Courtens, T.F., Rosenbaum, S.E., Wagler and P.M., Horn, Phys. Rev. B, 29,(1983),515

E.R., Cowley and A.K., Pant, Acta. Cryst., 26,(1970),439

R.A., Cowley, Adv. Phys., 12,(1963),421

R.A., Cowley, Acta. Cryst. A, 43,(1986),825

A.F., Devonshire, Adv. Phys., 3,(1954),85

O.W., Dietrich, J., Als-Nielsen and L., Passel, Phys. Rev. B, 14,(1976),4923

J.F., Dillon and C.E., Olsen, Phys. Rev. A, 135,(1964),434

C., Domb, and M.S., Green, Phase Transitions and Critical phenomena Vol 1-6 (Academic Press:London (1974))

B., Dorner, Acta. Cryst. A, 28,(1972),319

B., Dorner, Coherent Inelastic Neutron Scattering (Springer-Verlag: Berlin (1982))

S.F., Edwards and P.W., Anderson, J. Phys. F, 8,(1975),965

P., Egelstaff , An Introduction to the Liquid State (Pergamon Press:Oxford (1967))

P., Ehrenfest, Proc. Amsterdam Acad., 36,(1933),153

C.P., Enz, Rev. mod. Phys., 46,(1974),705

E., Fermi, Ric. Sci., 7,(1933),13

H.J.,Fischbeck and K.H, Fischbeck Formulas Facts and Constants (Springer-

Verlag:Berlin 1982)

M.E., Fisher, Rev. mod. Phys., 46,(1974),587

M., Fishman and A., Aharony J. Phys. C 12, (1979), 235

A., Fouskova, V. Kohl, N.N., Krainik and I.T., Mylnikova, Ferroelectrics, 34,(1987),119

D., Forster, Hydrodynamic Fluctuations, Broken Symmetry and Correlation Functions (Addison Wesley: New York (1990))

P.G., de Gennes and J., Villain, J. Phys. Chem. Sol., 13,(1960),10

K., Gesi, Phys. Rev. B, (1975),1933

V.L., Ginzburg, Sov. Phys.: Solid State 2,(1960),1824

F.S., Glasso Structure, Properties and Preparation of Perovskite type Compounds (Pergamon Press:Oxford (1969))

J., Goldstone, Nuovo Cimento, 19,(1961),154

R.B., Griffiths, Phys. Rev. Lett., 24,(1970),1479

J.M.F., Gunn, G., Andreani and J., Mayers, J. Phys. C, 19,(1986),1835

I.L., Gurevich and L.V., Tasarov, Low Energy Neutron Physics (North Holland :Amsterdam (1968))

B.I., Halperin and P.C., Hohenberg, Phys. Rev., 177,(1969),952; Ibid.,10,(1974),139

B.I., Halperin and R., Varma Phys. Rev. B 19,(1977), 2395

A.B., Harris, J. Phys. C, 7,(1974),1671

C., Herring and C., Kittel, Phys. Rev., 81,(1951),869

J., Hog, In. J. Mag., 4,(1973),11

T., Holstein, and H., Primakoff, Phys. Rev., 58,(1940),1098

L.V., Hove,Phys. Rev.,93,(1954),268; .Ibid,95,(1954),249,1374;Ibid.,103,(1958),137

E., Ising, Z. .Phys., 31,(1925),253

H., Jackson, Phys.. Rev. A, 10,(1974),278

A.R., Jani, and V.B., Cohel, Solid Stat. Comm., 43,(1982),945

D.P., Kadanoff, W., Gotze, D., Hamblen, R., Hecht, E.A.S., Lewis, V.V., Palciauskas, M., Rayl, J., Swift, D., Aspnes and J., Kane Rev. mod. Phys., 39,(1967),395

A.A., Karamyan and N.N., Krainik, Sov. Phys.: Solid State 15,(1973),1687

K., Kasuya, IBM J. Res. Dev., 14,(1970),214

K., Kawasaki and H., Mori, Prog. theor. Phys., 25,(1961),1045;.Ibid, 28,(1962),690

;.Ibid.,38, (1967),1045

D., Keating, A., Nunues, B., Batterman, J., Hastings, Phys. Rev. Lett. 27,(1971),320

M.W., Klein, C., Held and E., Zuroff, Phys. Rev. B, 13,(1976),3576

O.Y., Korshunov, P.A., Markovin, and R.V., Pizarev, Sov. Phys.: Solid State 25,(1983),7

N.N., Krainik and V.A., Trepakov, Sov. Phys.: Solid State 24,(1982),1608

N.N., Krainik, S.A., Flerova and S.A., Popav, Sov. Phys.: Solid State 29,(1987),1636

H.B., Krause and D.L., Gibbon, Z. Kristallog., 134,(1971),43

H.B., Krause, J.M., Cowley and J., Wheatley, Acta. Cryst. A, 35,(1979),1015

K., Krebs, Phys. Rev., 138,(1965),143

L.P., Landau, Zh. Eksp. Teor. Fiz., 16,(1937),627

L.P., Landau, Statistical Physics (Pergamon Press:London (1958))

W.N., Lawless, Phys. Rev. B, 14,(1976),134;.Ibid,17,(1976),1458

W.N., Lawless, Ferroelectrics, 15,(1977),61,159

R. Lloyd, P., Mitchell, Physica B, 156,(1989),235

S.W., Lovesey, Theory of Neutron Scattering from Condensed Matter Vol. 2 (Clarendon Press: Oxford (1984))

T.C., Lubensky, Phys. Rev. B, 11,(1975),3573

C.A., Lucas (private communication (1988))

P., Luger, Modern X-Ray Analysis in Single Crystals (Springer-Verlag: Berlin (1980))

R.H., Lyddane, R.G., Sachs and E., Teller, Phys. Rev., 59,(1941),673

S.K., Ma, Modern Theory of Critical Phenomena (W.A. Benjamin:London (1976))

P., Maheswaranthan and R.J., Sladek, Phys. Rev. B, 35,(1987),3369

D.L., Martin, Physica 25,(1959),1193

B.T., Mathias, B.M., Bozarth and J.H., Vleck, Phys. Rev. Lett., 7,(1961),160

G.F., Mazenko, Phys. Rev. B, 14,(1976),3933

C.M.,McCarthy, C.W., Thompson and S.A., Werner Phys. Rev., 22,(1980),574

R., Migoni, H., Bitz and D., Banerle, Phys. Rev. Lett., 37,(1976),1155

V.J., Minkiewicz, M.F., Collins, R., Nathans and G., Shirane Phys. Rev., 182,(1969),624

P.W., Mitchell, R.A., Cowley and R., Pynn, J. Phys. C, 17,(1984),L875

P.W., Mitchell and M.T., Dove, J. Appl. Cryst., 18,(1985),493

P.W., Mitchell (private communication (1987))

L. K., Moleko and H. R., Glyde, Phys. Rev. Lett., 59,(1985),901

D.J., Montgomery and E.J., Covington, J. Chem. Phys., 27,(1957),1030

R.M., Moon, T., Riste and W.C., Koehler, Phys. Rev., 181,(1966),920

E.G., Nadolniskaya,N.N., Krainik, A.V. Shil'nikov and G.A. Smolensky Sov. Phys.: Solid State 29,(1987),1932

E.G., Nadolniskaya, N.N., Kranik, A.V., Shil'nikov, G.A., Smolensky and L. Kh., Vologirova Sov. Phys.: Solid State 30,(1988),82

M.S., Nelkin and D.E, Parks, Phys. Rev., 119,(1960),1060

J.F., Nye, Physical Properties of Crystals (Oxford University Press:Oxford (1957))

L., Onsager, Phys. Rev., 65,(1944),117

L., Passel, O.W., Dietrich and J., Als Nielsen, Phys. Rev. B, 14,(1976),4897

P., Pfeuty, G., Toulouse, Introduction to the Renormalisation Group to Critical Phenomenon (Wiley Eastern Ltd:New Delhi (1977))

R., Pynn, Rev. Sci. Instrum. 55,(1984),837

V., Ramamurthy and M., Satishkumar, Phys. Rev. B, 322,(1985),5471

K.E., Riedel and F., Wegner, Phys. Rev. Lett., 24,(1970),730,930

V.D., Salnikov, Y.S., Kuzminov and Y.N., Vanevtsev, Izv. Akad. Nauk. SSSR, 7,(1971),1277

G., Schmidt H., Arndt, C., Borchhardt, J., Von Geminski, T., Petzscha, K., Borman, A., Stenberg, A., Zirnite and V.A. Isupov Phys. Stat. Sol., 63,(1981),501

P., Schofield, Phys. Rev. Lett., 4,(1960),239

J.F., Scott, Rev. mod. Phys., 46,(1974),83

V.F., Sears, Solid. Stat. Comm., 11,(1972),1307

V.F., Sears, Adv. Phys., 24,(1975),1

V.F., Sears, Can. J. Phys., 59,(1981),555

V.F., Sears, Phys. Rev. B, 30,(1984),44

L.D., Shannon, Acta. Cryst. A, 32,(1976),751

V.I., Sizykh, V.A.,Isupov and V.V., Krillov, Sov. Phys.: Solid State 29,(1987),446

H., Smith, Neutron Inelastic Scattering, I.A.E.A. 2,(1968),149

G.A., Smolensky, J. Phys. Soc. Jap., 28,(1970),26

G.A., Smolensky, Ferroelectrics, 53,(1984),129

G.A., Smolensky, I.G., Siny, R.V., Pisarev, E.G. and Kuziminov Ferroelectrics 12,(1976),135

G.A., Smolensky and N.K., Yuskin, Sov. Phys.: Solid State 27,(1985),492

H.E., Stanley, Phase Transitions and Critical Phenomena (Clarendon Press:Oxford (1971))

J.C., Toledano, The Landau Theory of Phase Transitions (McGraw-Hill:New York (1988))

H., Thomas and J.C., Slowezewski, Phys. Rev. B, 1,(1970),3599

V.F., Turchin, Slow Neutrons (Israel Program for Scientific Translations :Tel Aviv (1965))

V.G., Vaks, A.I., Larkin and S.A., Pilkin, JETP, 26,(1968),647

J., Villain, Critical Phenomenon in Alloys and Magnets and Superconductors (New York: McGraw Hill(1971))

B.E., Vugmeister, Sov. Phys.: Solid State 26,(1984),658; .Ibid,27 ,(1985),716

B., Widom, J. Chem. Phys., 43,(1965),3892,3898

B.T.M., Willis, Thermal Vibrations in Crystallography (Cambridge University Press:Cambridge (1975))

K.G., Wilson, Phys. Repts. 12C,(1974),77

K.G., Wilson and J., Kogut, Phys. Repts. 12C,(1974),75

C.W., Windsor Pulsed Neutron Scattering (Taylor Francis:London (1981))

A.Y., Wu and R.J., Sladek, Phys. Rev. B, 27,(1982),2089

I.S., Zheludev, Crystalline Dielectrics (Plenum Press:London (1971))